

UC Davis

UC Davis Electronic Theses and Dissertations

Title

Quantitative Adjustment of Sun-View Geometry in Areal Remote Sensing

Permalink

<https://escholarship.org/uc/item/8412s64r>

Author

Jafarbiglu, Hamid

Publication Date

2023

Peer reviewed|Thesis/dissertation

Quantitative Adjustment of Sun-View Geometry in Areal Remote Sensing

By  
HAMID JAFARBIGLU

DISSERTATION

Submitted in partial satisfaction of the requirements for the degree of

DOCTOR OF PHILOSOPHY

in

Biological Systems Engineering

in the

OFFICE OF GRADUATE STUDIES

of the

UNIVERSITY OF CALIFORNIA

DAVIS

Approved:

---

Alireza Pourreza, Chair

---

Ali Moghimi

---

Troy Magney

---

Yufang Jin

Committee in Charge

2023

## ABSTRACT

Remote sensing and digital agriculture have emerged as practical tools in modern farming, promising significant advancements in agricultural efficiency, sustainability, and productivity. These technologies could enable farmers and researchers to gather essential data, make informed decisions, and manage resources more effectively, ultimately contributing to the global challenge of feeding a growing population while minimizing environmental impact. Remote sensing data, especially high-resolution UAS-based imagery, could provide detailed and real-time information about crop health, soil moisture, nutrient levels, and pest infestations. This information play an important role in addressing key agricultural challenges including I) limited resources, II) newly emerging or common diseases, iii) climate change and extreme weather outbreaks, and IV) sustainability. The wealth of data enables farmers to implement precision agriculture techniques, tailoring interventions and resources to specific areas of the field. The timely detection and monitoring of crop diseases allows farmers to take proactive measures and prevent large-scale outbreaks. Early-stage detection of problems enable farmers to mitigate losses, improve crop quality, and reduce the need for excessive chemical treatments. Remote sensing data enables high-thruput phenotyping and selection of more resilient and climate-adept crop varieties. Finally, constant monitoring and precise resource management facilitate sustainable production. All advantages of remote sensing applications discussed above depends on the accuracy and reliability of the data collected and correct interpretation of the data.

Despite the extensive deployment of remote sensing tools in agricultural industry for several decades, the anticipated outcomes have often fallen short of initial expectations. This shortcoming can be attributed to several interrelated factors including challenges related to data accuracy, resolution, data interpretation issues, and inconsistency across different spatial and temporal scales. Additionally, the dynamic nature of environmental processes and the inherent complexity of ecosystems makes it challenges to establish cause-and-effect relationships between remote sensing and ground truth data. The aforementioned challenges and limitations motivated our first study, which aims to comprehensively review the current

platforms, applications, and methodologies employed in remote sensing (with a focus on nut crops) and identify the potential error sources that cause these shortcomings. In this study we realized that radiometric correction, which is an essential data preprocessing step, has not been taken seriously in most studies. Without correct radiometric calibration, the recorded values may not represent true surface reflectance, leading to inaccuracies in the quantitative analysis. Additionally, inaccurate calibration can hinder the ability to compare and integrate data from different sensors or acquired at different times, as the variations in sensor responses or environments may not be properly accounted for, hence preventing generalizability of the methods and results.

Further investigation into the radiometric calibration steps and associated issues highlighted a significant environmental factor that can impact the collected data and lead to questionable interpretations. Specifically, the relationship between sun-plant-sensor geometry and the acquired remote sensing data stood up as a crucial discrepancy source. Conventionally, researchers collect reflectance data around “solar noon” in an attempt to minimize the irradiance changes. However, solar noon could be very different in terms of sun angle depending on the location and season. This formed our main study which focuses on understanding the impact of sun-view geometry on spectral reflectance variability of crops. In this study we showed that even a small  $2^\circ$  change in view angle of the remote sensing camera can lead to substantial differences in canopy reflectance, especially close to hotspot area. These variations, often assumed negligible, can exceed  $\pm 50\%$  of the nadir view due to directional solar radiation within a drone image. We introduced a model based on the Laplacian distribution function that can be used to compensated for these variations with up to %88 accuracy. With this model data become more comparable and hence the results more generalizable. Additionally, several other factors that are critical for radiometric calibration were investigated and recommendations for more reliable data collection or processing were suggested. Finally we developed an application, which is publicly accessible through Digital Ag Lab’s website (<https://digitalag.ucdavis.edu/decision-support-tools/when2fly>), recommends

the best UAS flight time to collect more reliable agricultural remote sensing data based on the sites location, date, and camera's field of view.

## **ACKNOWLEDGMENTS**

I extend my sincere gratitude to my wife, Fatemeh Afshar, for her unlimited support, love, patience, and encouragement that enabled me to pursue my dreams. I also would like to thank Professor Alireza Pourreza for his compassionate mentorship, vision, inspiration, patience, and support throughout my graduate studies. I would also like to thank Professor Ali Moghimi, Professor Troy Magney, and Professor Yufang Jin for their careful review and thoughtful suggestions that greatly improved the quality of this work. I am appreciative of each member of the Digital Ag lab for their years of support and friendship. I especially acknowledge Momtanu Chakraborty, Yuto Kamiya, Sirapoom Peanusaha, Mohammadreza Narimani, and Kyle Cheung. I am extremely grateful to the Department of Biological and Agricultural Engineering and its chair professor Fadi Fathallah for his exemplary leadership. I also thank Victor Duraj for trying to keep us safe and successful. I acknowledge the financial support of the United States Department of Agriculture- National Institute of Food and Agriculture (USDA-NIFA) and The Agriculture and Food Research Initiative (USDA-AFRI). I especially thank my family and friends for their mentorship and support to pursue a doctorate degree abroad.

## TABLE OF CONTENTS

ABSTRACT .....	II
ACKNOWLEDGMENTS .....	V
TABLE OF CONTENTS .....	VI
LIST OF FIGURES .....	VIII
LIST OF TABLES .....	IX
ABBREVIATIONS AND ACRONYMS .....	X
1 A Comprehensive Review of Remote Sensing Platforms, Sensors, and Applications in Nut Crops....	1
1.1 Introduction.....	1
1.2 Platforms.....	3
1.2.1 Unmanned Aerial Systems .....	6
1.2.2 Manned Aircraft .....	8
1.2.3 Satellite .....	9
1.3 Sensors.....	10
1.3.1 RGB Camera.....	13
1.3.2 Multispectral .....	15
1.3.3 Hyperspectral .....	16
1.3.4 Thermal.....	17
1.3.5 Lidar.....	19
1.3.6 Radar.....	20
1.4 Applications.....	21
1.4.1 Water Status .....	21
1.4.2 Disease control.....	25
1.4.3 Yield mapping and prediction .....	27
1.4.4 Nutrient management.....	29
1.4.5 Salinity.....	32
1.4.6 Phenotyping .....	33
1.5 Data processing and analysis.....	33
1.5.1 Preprocessing .....	33
1.5.2 Processing .....	40
1.5.3 Analytics .....	43

1.6	Conclusions.....	48
2	Impact of Sun-View Geometry on Canopy Spectral Reflectance Variability .....	50
2.1	Introduction.....	50
2.2	Materials and methods .....	54
2.2.1	Formulation.....	54
2.2.2	Experimental fields and data collection.....	56
2.2.3	Processing .....	58
2.2.4	Modeling.....	60
2.3	Results.....	62
2.3.1	Variation modeling.....	64
2.3.2	Physical-based Simulation .....	66
2.4	Discussion .....	69
2.5	Conclusion .....	73
3	Overall Conclusions and Future Work .....	75
3.1	Overall Discussion and Conclusions .....	75
3.2	Future research.....	77
4	REFERENCES .....	78
5	Appendix .....	96

Dfgjsk



## LIST OF FIGURES

Figure 1.1- Increasing acreage of nuts (Almond, Walnut, Pistachio) in California, USA (1990-2019) .....	2
Figure 1.2- Remote sensing platforms based on their altitude and flight time. ....	4
Figure 1.3- The Electromagnetic spectrum, different wavelengths and regions, bands' energy level, .....	13
Figure 1.4- Leaf reflectance of a healthy walnut leaf and a healthy almond leaf .....	17
Figure 1.5- The Web of Science search results from 2011 to 2020 for hyperspectral and multispectral....	31
Figure 1.6- Types of noises affecting a remote sensing sensor; Environmental and Sensor-based noises.	36
Figure 1.7- Graphical representation of DSM, DTM, CHM, and zero line. ....	40
Figure 1.8 - Image segmentation of an aerial multispectral image from an almond orchard. ....	42
Figure 2.1- Diagram of solar light components, directional and diffuse, radiating on a surface .....	56
Figure 2.2- The citrus block of the experiments.....	57
Figure 2.3- Different view angles of the same tree due to the overlapping images. ....	59
Figure 2.4- Defining new coordinates based on the hotspot.....	61
Figure 2.5- The effect of directional solar radiation on the reflectance .....	64
Figure 2.6- 3D representation of data points and fitted model(a). ....	65
Figure 2.7- Variation of canopy reflectance in prime view (close to nadir) vs. other views (off-nadir)....	66
Figure 2.8- Reflectance values for UAS-based measurements (top) compared to 4Sail simulation .....	67
Figure 2.9- Reflectance variations due to the sun-view angle difference ( $\theta_r - \theta_i$ ).....	69
Figure 2.10- Recommended flight time in the central valley of California .....	71
Figure A. 1- Percentage of reflectance variation from the Nadir view .....	98
Figure A. 2- An example of the DLS sensor reading on a partly cloudy day.....	98
Figure A. 3- DLS readings of the MRE when the flight mission is parallel to the solar plane. ....	99
Figure A. 4- DLS readings of a P4M flight mission whose paths are parallel to the solar plane. ....	99

## LIST OF TABLES

Table 1-1-comparison of satellites, manned aircraft, and UAS for their strength and weakness .....	5
Table 1-2- Platform types, application and sensors used in Almond, Walnut, and Pistachio studies. ....	5
Table 1-3- Common vegetation indeces used for Greenees Idnetification using RGB cameras .....	14
Table 1-4- Examples of remote sensing application for disease detection.....	27
Table 1-5-Analysis parameters of the selected papers .....	47
Table 2-1- Specifications of the cameras used in this study. ....	57
Table 2-2- summary of data collection from the crop sites. ....	58
Table 2-3- Parameters used in 4SAIL models. ....	62
Table 2-4- The results of directional effects and modeling on the citrus dataset .....	62
Table A. 1- The full results of the experiments outlined in this study.....	96

## ABBREVIATIONS AND ACRONYMS

Name	Abbreviation
Above Ground Level	AGL
Advanced Spaceborne Thermal Emission and Reflection Radiometer	ASTER
Airborne Visible/Infrared Imaging Spectrometer	AVIRIS
American Society for Photogrammetry and Remote Sensing	ASPRS
Artificial Neural Networks	ANN
Average Root Mean Square Deviation	ARMSD
beyond visual line-of-sight	BVLOS
Bidirectional Reflectance Distribution Function	BRDF
Bidirectional Reflectance Factor	BRF
Canopy Height Model	CHM
Canopy Response Salinity Index	CRSI
Charged Couple Device	CCD
Chlorophyll Absorption Ratio Index	CARI
Colored Infrared	CIR
Crop Water Stress Index	CWSI
Digital Elevation Mode	DEM
Digital Number	DN
Digital Surface Model	DSM
Digital Terrain Model	DTM
downwelling light sensor	DLS
electrical conductivity	EC
evapotranspiration	ET
Excessive Green Index	EGI
Federal Aviation Administration	FAA
Geoscience Laser Altimeter System	GLAS
Global Ecosystem Dynamics Investigation	GEDI
Global Navigation Satellite System	GNSS
Global Positioning System	GPS
Ground Control Points	GCP
Ground Sampling Distance	GSD
Hemispherical Reflectance Distribution Function	HRDF
hemispherical-directional reflectance factor	HDRF
High-Altitude Long Endurance	HALE
Hyperspectral	HS

Inertial Measurement Unit	IMU
Leaf Angle Distribution	LAD
Leaf Area Index	LAI
Leaf Inclination Distribution Function	LIDF
Light Detection and Ranging	Lidar
Low Earth orbit	LEO
Low-Altitude Long Endurance	LALE
Low-Altitude Short Endurance	LASE
Medium-Altitude Long Endurance	MALE
Micasense RedEdge 3	MRE
Moderate Resolution Imaging Spectroradiometer	MODIS
MODIS/ASTER	MASTER
multiple linear regressions	MLR
Multispectral	MS
Near-Infrared	NIR
Normalized Cross-Correlation	NCC
Normalized Difference Infrared Index	NDII
Normalized difference red edge index	NDRE
Normalized Difference Vegetation Index	NDVI
Partial Least Squares Regression	PLSR
Phantom 4 multispectral	P4M
Photochemical Reflectance Index	PRI
photosynthetically active radiation	PAR
Physical-Based Models	PBM
Precision Agriculture	PA
Precision Agriculture	PA
Precision Pest Management	PPM
principal component analysis	PCA
Radiative Transfer Model	RTM
Real Time Kinematic	RTK
Red-Green-Blue	RGB
Regression Trees	RT
Root Mean Square	RMS
Root Mean Square Deviation	RMSD
Scale-Invariant Feature Transform	SIFT
self-organization mapping	SOM
Short Wave Infra-Red	SWIR
Spectral Mixture Analysis	SMA
Standard deviation	STD
State of California	CA
Stem Water Potential	SWP

Structure-From-Motion	SFM
Synthetic Aperture Radar	SAR
Synthetic Aperture Radar	SAR
The Crop Water Stress Index	CWSI
The Discrete Anisotropic Radiative Transfer Model	DART
The National Aeronautics and Space Administration	NASA
The Normalized Difference Water Index	NDWI
The Normalized Multi-band Drought Index	NMDI
The Water Band Index	WBI
The Water Index	WI
Thermal	TH
Thermal Infrared Multispectral Scanner	TIMS
Uncrewed Aerial Systems	UAS
Uninhabited Aerial Vehicle Synthetic Aperture Radar	UAVSAR
Vapor Pressure Deficit	VPD
Vegetation Index	VI
vertical take-off and landing	VTOL

# **1 A Comprehensive Review of Remote Sensing Platforms, Sensors, and Applications in Nut Crops**

## **1.1 Introduction**

The world's population is increasing rapidly, while providing enough food for this growing population has become a challenge. Food is usually categorized into different classes containing fruits, vegetables, grains, proteins, and dairy <sup>1</sup>. Due to high protein content, which is essential for the human body <sup>2</sup>, nuts are considered one of the main substitutes for meat and a popular element of American families' food basket. From 2000 to 2016, nut consumption has increased from 2.61 to 4.8 lb per capita <sup>3</sup>. Based on the California Department of Food and Agriculture, per capita consumption of fruits and tree nuts is the third-largest among the major food groups, after dairy products and vegetables <sup>4</sup>. The United States is among the top nuts producers globally, and the State of California (CA) produces about 100% of the United States' almonds, walnuts, and pistachios by estimated bearing acres of more than 1.53 million, 440,000, and 289,000, respectively. These orchards produced nuts with the total value of about \$9 billion in 2019 <sup>5</sup>. As shown in Figure 1.1, the growing trend of nut orchards is noticeable, especially for almond that has grown more than 300% during the past 25 years, with an estimated annual increase of 2-3.5% in the 2020s <sup>67</sup>. The nut industry continues to grow, engulfing more lands, raising demand for inputs, and causing an imbalance in available and needed resources <sup>8</sup>.

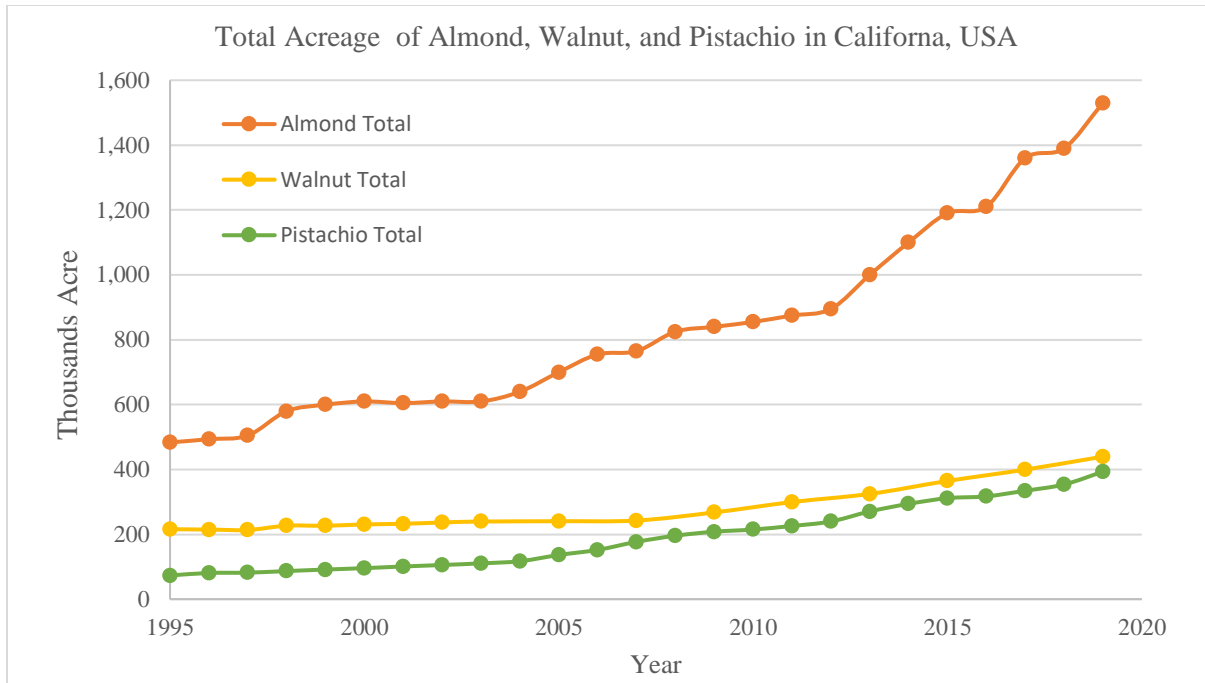


Figure 1.1- Increasing acreage of nuts (Almond, Walnut, Pistachio) in California, USA (1990-2019)<sup>6</sup>.

Limited natural resources restrict the expansion of new orchards; therefore, optimizing production practices becomes inevitable. As a result, many researchers worldwide are looking for sustainable solutions for food production systems compatible with depleting natural resources (water, arable land) <sup>9</sup>, increasingly extreme climate <sup>10</sup>, stricter environmental legislation, and the emergence of new and more resistant pests and diseases <sup>11</sup>. For this purpose, data-driven decision-making must substitute conventional orchard management techniques to address the inefficiency of agricultural operations such as irrigation, nutrient management, pest and disease management, pruning, and harvesting.

Precision Agriculture (PA) is a data-driven procedure to enhance agricultural efficiency by minimizing inputs and waste and maximizing yield quantity/quality while ensuring sustainability<sup>12</sup>. Models predicted that PA practices could increase the global yield by up to 67% by 2050 <sup>13</sup>. One crucial step of PA is large-scale data collection <sup>4</sup>, which is mostly conducted by remote sensing techniques, the cornerstone of the entire PA process. According to ASPRS (American Society for Photogrammetry and Remote Sensing), remote sensing is defined as “the measurement or acquisition of information of some property of an object or phenomena, by a recording device that is not in physical or intimate contact with the object or

phenomenon under study, e.g., the utilization at a distance”<sup>14</sup>. Remote sensing in agriculture employ electromagnetic radiation to record plants' physical and physiological characteristics non-destructively <sup>15</sup>. These data can be linked to various biotic and abiotic stresses or other quantities <sup>15</sup>.

In this manuscript, we conducted a comprehensive literature review on remote sensing and aerial imaging applications with a focus on nut production. However, most of the materials presented in this research is applicable to other specialty crops. This chapter is organized as follows: In section 1.2, several aerial data collection platforms are discussed. Section 1.3 explores the advantages and disadvantages of different types of sensors. In section 1.4, various applications of remote sensing data are discussed. Section 1.5 focuses on data processing and analysis steps, and finally, in section 1.6, conclusions are presented.

## 1.2 Platforms

Remote sensing platforms are defined as vehicles, such as aircraft or satellites, that can carry sensing devices to perform remote measurement operations. These platforms are continuously improving in terms of operational time, reliability, simplicity, and temporal resolution (the time interval between successive remote sensing measurements), which affects the spatial resolution. With diverse options available with specific characteristics, choosing a suitable platform depends on the nature of the problem. Satellites, for instance, can quickly map a vast area, but their spatial resolution is coarse for some PA proposes. Unmanned aerial systems (UAS), on the other hand, are well suited for small-scale and research applications, and they can provide very high spatial resolutions. However, the limited payload and short flight endurance remain the main drawbacks for large-scale UAS implementation. Manned aircraft fall in between, covering larger areas compared to UAS and delivering higher spatial resolution than satellites.

Three critical factors for selecting the best platform are spatial resolution, farm size, and operation cost. A cost analysis (in 2014) showed that the adoption of UAS platforms for aerial imagery is profitable in areas less than five hectares; above such threshold, manned aircraft and then satellites have lower operation costs <sup>16</sup>. This threshold extended to 20 ha in 2018 <sup>17</sup>. Figure 1.2 shows a coarse classification of different platforms based on altitude and flight endurance. In this classification, aircraft (manned or unmanned) can be divided into four categories: Low-Altitude Short Endurance (LASE), Low-Altitude Long Endurance



(LALE), Medium-Altitude Long Endurance (MALE), and High-Altitude Long Endurance (HALE) <sup>18</sup>. Despite their advantages in flight time and energy efficiency, HALE and MALE categories are expensive, complicated, and their operation-altitude conflicts with that of passenger aircraft, leaving LALE and LASE platforms the most common remote sensing platforms <sup>19</sup>. Most of the commonly used UAS fit in the LASE class with a limited flight altitude of lower than 1500 m above ground level (AGL). However, new legislation in some countries further limits UAS flight ceiling from 90 to 150 m AGL<sup>19</sup>. Remote sensing satellites, on the other hand, are in a specific range of Low Earth orbit (LEO), higher than the airspace of any aircraft and lower than other satellites such as Global Navigation Satellite System (GNSS).

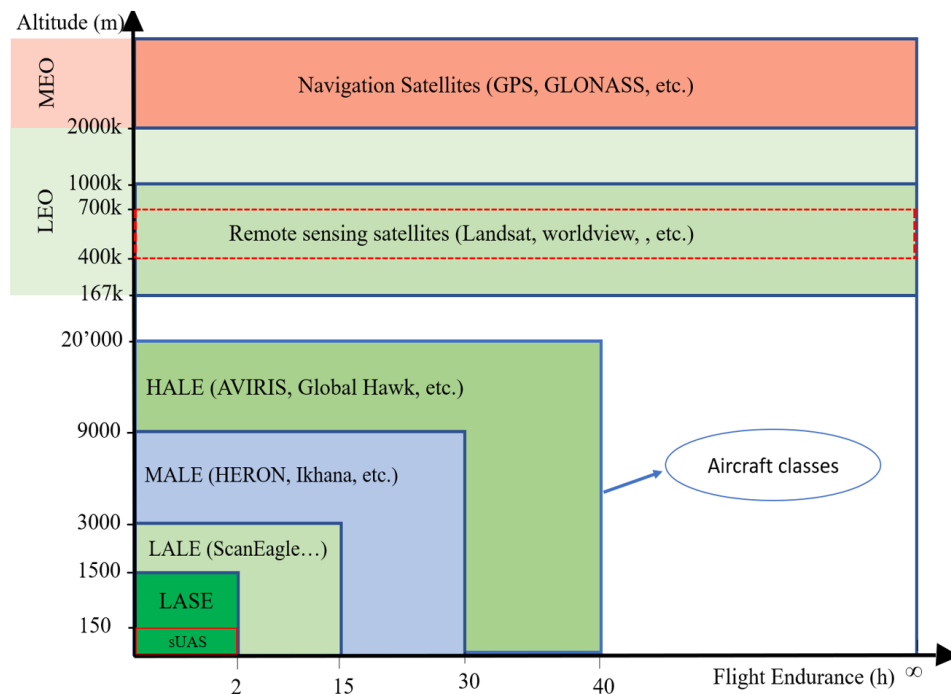


Figure 1.2- Remote sensing platforms based on their altitude and flight time. HALE (High-Altitude Long Endurance), MALE (Medium-Altitude Long Endurance), LALE (Low-Altitude Long Endurance), and LASE (Low-Altitude Short Endurance) are the main classification of aircraft platforms where sUAS are a sub-class of LASE with a maximum take-off weight of 25 kg (55lb). Satellites on the other hand, make measurements from as far as 400k meters away<sup>18 19</sup>.

In this section, three main remote sensing platforms, UAS, manned aircraft, and satellites, are reviewed. Table 1 compares the essential characteristics of satellites, manned aircraft, and UAS <sup>17</sup>. Two of the noticeable features in this table are expected advances in upcoming years and data processing complexity

that are higher for UAS compared to the other platforms. On the other hand, spatial coverage and flight endurance are the main advantages of satellites over UAS and manned aircraft.

Table 1-1-comparison of satellites, manned aircraft, and UAS for their strength and weakness<sup>17</sup>

	Satellites	Manned Aircraft	UAS
Spatial Resolution	Low	Med	High
Temporal Resolution	Low	Med	High
Expected Advances	Low	Med	High
Number of systems/sensors	Low	Med	High
Data Processing complexity	Low	Med	High
Spatial Coverage	High	Med	Low
Flight Altitude	High	Med	Low
Flight Endurance	High	Med	Low

For further comparison of the platforms, sensors, analysis methods, etc., 20 papers on remote sensing of almond, walnut, and pistachio orchards were selected, and results were compared. Table 2 includes the platforms used in these studies. Some studies used more than one platform. For example, in <sup>20</sup> sUAS, manned aircraft, and satellite platforms are used simultaneously, and in <sup>21</sup> manned aircraft and satellite data combined to extract as much data as possible. Besides the platforms, the type of the sensors - RGB, multispectral (MS), hyperspectral (HS), and Thermal (TH)- study area, intended application, whether the sensors were calibrated, and flight altitude are also specified in this table. Platforms, sensors and their calibration, and applications will be discussed in detail in the following sections.

Table 1-2- Platform types, application and sensors used in Almond, Walnut, and Pistachio studies.

	Crop	Platform name	Study Area (ha)	Application	Sensor/Spatial Resolution	Calibrat.	Altitude (m)	Total #
s U A S	Alm.	Quadkit, 3DRobotics <sup>7</sup>	< 1	Water Status	MS <sup>1</sup> /1.9 cm	✓	60	6
	Alm.	Mikrokopter <sup>22</sup>	< 1	Water Status	IR sensor-MS	×	20	
	Alm.	MD4-1000 <sup>23 / 24</sup>	1.45/ 2.5	Phenotyping	RGB <sup>2</sup> /15 mm	NA	50	
	Pista.	Phantom IV <sup>25</sup>	45	Height estimation	RGB/3.5 cm	NA	70	
	Alm.	Solo 3DR <sup>20</sup>	~60	Floral Phenology	MS/2.6–5.2 cm	✓	60-120	
	Alm.	Benzin Acrobatic <sup>26</sup>	4	Water Status	TH <sup>3</sup> / 12 cm	✓	150	
	Fixed-Wing	Alm.	mX-SIGHT <sup>27</sup>	42	Water Status	TH/50 cm	×	370
Pista.	mX-SIGHT <sup>28</sup>	260	Water Status	TH/35 cm	✓	250		
Manned	Alm.	Cessna <sup>29</sup>	5.5	Disease	HS <sup>4</sup> /30 cm, TH/40 cm	✓✓	550	11k
	Alm.	Cessna <sup>30</sup>	5.5	Water Status	HS <sup>4</sup> /20 cm, TH/25 cm	✓✓	200	
	A/P	CERES Imaging <sup>21</sup>	16	Water Status	TH/ 0.6-1.5 m	✓	500-1k	
	Alm.	MASTER <sup>** 31</sup>	1500	Water Status	TH/ 7.2 m	✓	11k	

Aircraft	A/P	AVIRIS <sup>32</sup>	700	Water Status	HS/ 7.1 m	✓	8.5k	9
	Alm.	CERES Imaging <sup>20</sup>	1700	Floral Phenology	MS/20 cm	✓	368	
	Alm.	NAIP* <sup>33</sup>	8000	Yield Prediction	MS/ 0.6 m	×	5k	
	Alm.	UAVSAR**** <sup>34</sup>	18000	Crop Separability	R <sup>5</sup> / 1.3 m	NA	12.5k	
	A/W/P	AVIRIS***/MASTER <sup>35</sup>	300,000	Water Status	HS/18 m, TH/36 m	✓✓	20k	
Satellites	A/P	Landsat-8 <sup>21</sup>	16	Water Status	MS/ 30m	✓	705k	5
	Pista.	Landsat-8 <sup>36</sup>	160	Salinity	MS/30 m, TH/100 m	✓✓	705k	
	Alm.	PlanetScope, Sentinel-2, Landsat <sup>20</sup>	1700	Floral Phenology	MS/3-30m	✓	LEO	
	Alm.	Landsat 5-7 <sup>37</sup>	2000	Water Status	MS/30 m, TH/120 m	✓✓	705k	
	Pista.	ALOS <sup>38</sup>	7000	Tree Distribution	MS/10 m	✓	692k	

\* National Agriculture Imagery Program of United States Department of Agriculture

\*\* MASTER (MODIS/ASTER)- Moderate Resolution Imaging Spectroradiometer (MODIS)/ Advanced Spaceborne Thermal Emission and Reflection Radiometer (ASTER)

\*\*\*Airborne Visible/Infrared Imaging Spectrometer (AVIRIS)

\*\*\*\* Uninhabited Aerial Vehicle Synthetic Aperture Radar (UAVSAR)- Even though it is designed to work on UASs, currently, UAVSAR is mounted on a NASA Gulfstream III aircraft (C-20A/G-III) <sup>39</sup>.

- |    |               |    |                                     |    |         |
|----|---------------|----|-------------------------------------|----|---------|
| 1- | Multispectral | 2- | Red-Green-Blue conventional cameras | 3- | Thermal |
| 4- | Hyperspectral | 5- | Radar                               |    |         |

### 1.2.1 Unmanned Aerial Systems

An Unmanned Aerial System (UAS) is an aircraft capable of flying autonomously or controlled by a remote pilot <sup>40</sup>. Payload and flight endurance were two main challenges of using early UASs for agricultural purposes. During the 1990s, UAS capable of carrying powerful and accurate sensors tended to be large and very expensive, while small platforms lacked adequate payload capacity to carry heavy sensors and deliver precise data. As a result, the science community in the late 1990s focused on sensor miniaturization to enable the use of small and affordable UAS platforms for survey-grade data delivery <sup>18</sup>. Using small Unmanned Aerial Systems (sUAS) or drones, which includes drones weighing less than 25 kg (55 pounds)<sup>41,42</sup>, in agricultural tasks started in the early 2000s <sup>43</sup> and then expanded swiftly to become one of the ten breakthrough technologies in 2014 <sup>44</sup> and continues increasing. According to Federal Aviation Administration (FAA) report in March 2018 <sup>45</sup>, the number of commercial drones is expected to be quadrupled, from 110,604 in 2017 to 451,800 by 2022, where drone technologies are estimated to provide service worth \$127 billion <sup>46</sup>.

Nowadays, an sUAS equipped with cameras and software that costs less than \$1000 can quickly survey over 100 acres in a short flight <sup>47</sup>. Additionally, growers can fly over and monitor fields on a monthly, weekly, daily, and even hourly basis <sup>48</sup>, depending on the desired temporal resolution. It is promising that drone-based remote sensing can provide inter- and intra- field variability of crops information and help

optimize irrigation schedule and increase water use efficiency<sup>47</sup>. Multirotor, single-rotor, and fixed-wing are the three types of drones commonly used in agriculture. The vertical take-off and landing (VTOL) and hovering capability of rotary drones make them very popular in agriculture, yet flight endurance and energy efficiency are serious cons. Because of this, some companies tried to combine fixed-wing and rotary drones to have both advantages of VTOL and flight endurance.

Usually, cameras and sensors account for a significant share of the cost in drone-based field mapping. Although the higher price of these sensors and cameras limits their practical implementation by farmers and technicians<sup>49</sup>, they are critical for unraveling complex problems and paving the road for designing simpler sensors. Apart from the high price restrictions, limited payload, and short flight endurance, some other challenges might also be considered when choosing a drone for an application. For example, in the U.S., flying beyond visual line-of-sight (BVLOS) needs special approval, and the maximum flying altitude is limited to 122 meters above the ground level. Additionally, specific locations in the proximity of controlled airspace and airports are limited<sup>50</sup>.

Despite all the drawbacks mentioned above and restrictions, a high-resolution camera mounted on a drone could provide very high spatial resolution imagery in 1 cm level<sup>51</sup>, or even less, which explains their widespread use. Moreover, a great deal of effort has been put into improving the UASs' drawbacks. To ameliorate limited flight times, for instance, implementing new battery technologies (fast charge with higher energy density) and deploying solar panels on UASs can extend flight time from 40–50 min up to 5 h<sup>17</sup>. Additionally, efficient mission planning can improve flight coverage by eliminating unnecessary energy consumption. All in all, UASs, specifically multirotor drones, have attracted rapidly growing attention in agricultural practices.

According to table 2, more than 66% (6 out of 8) of the sUAS used in nut studies are multi-rotor drones capable of collecting RGB and MS images. This percentage goes down to around 22% (2 out of 9) for fixed-wing drones, and it is even less (around 11 %, 1 out of 9) for single rotor drones. Another interesting point for comparing different drone types is that most studies with multirotor drones have been

conducted recently (2014, 2017, 2018, 3\*2019), while studies based on the single rotor (2012) and fixed wing (2014) are older. This clearly shows the growing popularity of multi-rotor drones in the remote sensing application of nut orchards. Moreover, as discussed earlier, fixed-wing drones have higher endurance and can cover larger areas from higher altitudes that are in accordance with Table 2. On average, studies that used fixed-wing drones cover more than 150 ha, while this number for multi-rotor drones is less than 20 ha.

### 1.2.2 Manned Aircraft

Manned aircraft's usage in agriculture first started with aerial application of chemicals on crops during the 1920s<sup>52</sup>. Then by advances in photographic devices, airplanes were used as a platform for taking analog aerial imagery and vegetation mapping by the 1950s<sup>53</sup>. The National Aeronautics and Space Administration (NASA) in the United States is one of the pioneers at using aircraft for remote sensing. During the 1970s, NASA used P-3A aircraft, equipped with multiple remote sensing sensors, operating at about 300m AGL for agricultural purposes such as mapping soil moisture<sup>54 55</sup>. However, using aircraft for the research community was very limited, mainly due to operation and sensor costs.

Nevertheless, some studies were carried out with the help of private and governmental sectors, and their results were promising enough to attract the attention of other researchers in these areas. With an increasing demand for remote sensing data, some companies, such as Galileo Group, started supplying aircraft and sensors for researchers. High cost, need for infrastructure and trained pilots, operational complexity of flights, and lower repeatability due to lack of precise autopilot systems such as terrain-following are their main disadvantages of aircraft remote sensing<sup>47</sup>. In the last few years, most aerial mapping by manned aircraft has been overtaken by UASs. However, some research demands specific data obtained by an airplane better than any other platform. AVIRIS (Airborne Visible InfraRed Imaging Spectrometer)<sup>56</sup> is one of the most famous examples of remote sensing instruments based on airplane platforms. AVIRIS can record 224 contiguous calibrated spectral bands (400 - 2500 nm) at different altitudes covering the United States, Canada, and Europe. It has a variety of applications, including ecology, geology, and agriculture. For instance, AVIRIS data were used to study 3470 km<sup>2</sup> orchards,

including almond and walnut, during an intense drought period in California's Central Valley (2013–2015). Such a vast area is beyond drones' capability, yet the resolution is not comparable with that of drones. AVIRIS has datasets from 4 km to 20 km with a spatial resolution of 3.3 m to 18 m<sup>35</sup>. Other airplanes have recorded as high as 50 cm-resolution multispectral images<sup>57</sup>.

According to table 2, around 39% (9 out of 23) of nut studies have used data collected from manned aircraft platforms. However, less than half of them (<sup>20</sup>, <sup>21</sup>, <sup>29</sup>, and <sup>30</sup>15 % total) used the platform merely for their particular study purpose. The rest of the studies are based on the governmental provided data at a national or international level prepared for multi-purpose applications due to the excessive costs of deploying manned aircraft.

### 1.2.3 Satellite

The launch of Landsat 1 in 1972 was the response to the growing interest in remote sensing data for research during the 1960s. Rapid advances in digital image processing accelerated the progress of remote sensing to the point that Landsat 4 with a new generation of sensors was launched in 1982<sup>58</sup> with regular updates afterward. Today, satellite imagery's spatial resolution has reached submeter range (e.g., 0.31 m for panchromatic nadir images and 1.24 m multispectral nadir- WorldView-4) and can cover a vast area in every pass. Still, the use of satellite-based remote sensing in PA could be limited because of their low spatial resolution for some purposes and/or fixed acquisition times<sup>59</sup>. Additionally, satellite imagery has some intrinsic weaknesses due to its high altitude. In general, electromagnetic signals must pass through a considerable depth of the Earth's atmosphere to reach the sensor on the satellite, and based on the atmospheric condition, some degree of signal attenuation will happen, and some noise will be blended with signals. As a result, measurement time and period highly depend on the weather and atmosphere condition because of the limited satellite revisit time<sup>53</sup>.

Unlike sUAS platforms that are a suitable solution when a “micro” view of the land is of interest, satellites provide a relatively low-cost “macro” view of the terrains<sup>47</sup> that makes them an efficient method for large-scale mappings such as desertification, land cover classification, climate change, and inter-field comparisons. For instance, Jin et al. used the Landsat-8 observations to differentiate

evapotranspiration (ET) levels in 160 ha pistachio orchards with different salinity levels <sup>36</sup>. As shown in Table 2, the average study area based on satellite images exceeds 2000 ha with the spatial resolution ranging from 3 to 30 meters in MS data and over 100 meters for TH data.

As the literature suggests, vast areas can be mapped by satellite remote sensing, mainly for large-scale studies and monitoring. Nevertheless, even satellites with the highest image resolution lack the spatial, spectral, and temporal resolution required for precise measurements needed for most PA practices. In such cases, other platforms may provide better results.

### 1.3 Sensors

Early in the 1960s, a researcher named Evelyn Pruitt coined the term “remote sensing” when she recognized that aerial photography or aerial imagery no longer accurately described the many forms of imagery collected using radiation outside the visible region <sup>58</sup>. In the current literature, remote sensing is the science of acquiring and interpreting information about objects without physical contact. It includes sensing and recording reflected or emitted energy (in any wavelength), processing, and analyzing data to convert them to knowledge<sup>60</sup>. All objects radiate electromagnetic energy when their absolute temperature is above absolute zero, called black body radiation. With an absolute temperature of 5778 k, the sun is the primary energy source and electromagnetic radiation on earth. As shown in figure 1.3, the sun's radiation is mainly in the form of visible light and infrared radiation with a peak wavelength around 500 nm. Additionally, the earth itself, with a 290 K temperature, has weak radiation in a wide range with a peak at around 10  $\mu\text{m}$ . As a result, passive sensors depend on either the sun's or earth's radiations and are designed to work in spectrum regions with the highest natural radiation energy. For example, thermal detectors are usually designed to be sensitive to radiation ranging from 7  $\mu\text{m}$  to 14  $\mu\text{m}$  <sup>53</sup>.

Each region in the electromagnetic spectrum carries helpful information for a specific purpose. For example, 0.4 to 0.7  $\mu\text{m}$ , the visible range, is used for vision-based sensings such as chlorophyll studies, green indices, morphological analysis of leaves and fruits, and vision-based measures to quantify all valuable data perceptible by a naked eye. On the other hand, the infrared region is used to extract data otherwise hidden from our eyes, such as water content and stress-related studies. Figure 1.3 shows the

electromagnetic spectrum with separated regions and example applications in agriculture for each region. There are no clear-cut boundaries dividing the electromagnetic regions; boundaries vary based on the application. The irradiance graph covering 250-2500 nm of the spectrum, the most commonly used region for agricultural remote sensing<sup>61</sup>, depicts the sun's black body radiation, radiations available in outer space, and sea-level radiations<sup>62</sup>. As mentioned before, atmospheric attenuation affects most of the spectrum with varying degrees and filters some bands entirely. The resistance of electromagnetic radiation against attenuation by the atmosphere and specific particles depends on its wavelength and interaction with the particles. For example, water vapor strongly absorbs radiation at around 1.1  $\mu\text{m}$  and 1.34  $\mu\text{m}$ , while in between, almost no energy is absorbed. A detailed list of atmospheric gases and their absorption bands can be found at<sup>63</sup>. The visible region of the sun's radiation undergoes minimal atmospheric attenuation making it a powerful region for remote sensing purposes. In this region, a large number of relatively high-energy photons (higher the frequency, higher the energy) create the highest watts per square meter per nanometer (Irradiance – see Figure 1.3), large enough to trigger a tiny detector (higher spatial resolution). The farther from the visible range, the smaller the irradiance in both directions. As a result, bigger (lower spatial resolution) or more sensitive detectors are required to measure the changes. When the amount of natural irradiance is too small, measuring the differences becomes challenging, inspiring the idea of using active sensors.

Active sensors include an energy source that emits electromagnetic energy in specific wavelengths and measures reflectance as opposed to passive sensors. Radar, Microwave, and Light Detection and Ranging (LiDAR) are examples of active sensors used in remote sensing. When a radiated signal reaches an object's surface, three major forms of interaction take place: absorption, transmission, and reflection. In most remote sensing sensors, the reflected portion of the radiation is measured<sup>48</sup>. The ratio of reflected radiation to incident radiation, defined as reflectance, plays a crucial role in revealing the surface's features.

As shown in Figure 1.3, specific wavelengths are suitable for each application. An effective wavelength can be selected based on the structure and components of materials being sensed, the distance between the



sensor and the object, and cloud, dust, or other particles between the object and the sensor. For instance, while clouds and water vapor block visible bands, radar signals can easily penetrate through them. Most of the sensors used for agricultural remote sensing take advantage of specific wavelengths. A comprehensive comparison of available sensors for UAS applications, including optical, multi/hyperspectral, thermal cameras, and LiDARs, is presented <sup>17</sup>.

Besides sensitive wavelengths, other essential parameters of any remote sensing sensors are spectral, radiometric, and spatial resolutions. The electromagnetic spectrum contains continuous wavelengths, while the digital sensors take discrete measurements. Their sensitive range and spectral resolution usually characterize sensors. Spectral resolution defines the number of measurements that a sensor can conduct at different wavelengths within a specific spectral range, i.e., the number of bands (or channels) in the instrument's sensitive range<sup>64</sup>. For example, the spectral resolution of a hyperspectral sensor that is sensitive to 400-1000 nm region and can measure 100 bands would be 6 nm. However, higher spectral resolution means less energy increasing the spatial resolution. However, the precision of each recording depends on the radiometric resolution defined as the sensor's ability to perceive and distinguish minimum change within its dynamic range, i.e., the precision at which the sensor records the data. Radiometric resolution often depends on the bit-depth of the sensor.

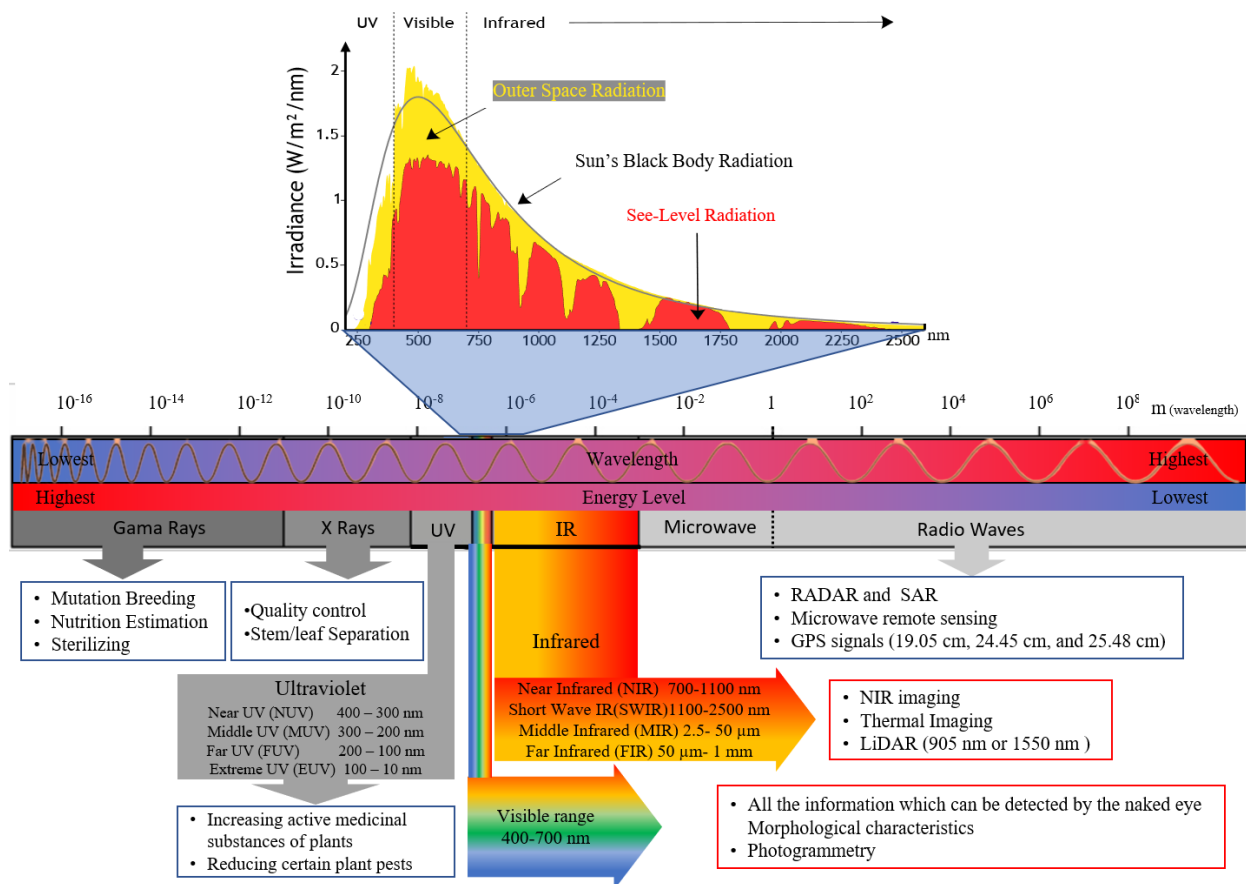


Figure 1.3- The Electromagnetic spectrum, different wavelengths and regions, bands' energy level, and some examples of their use in agricultural remote sensing applications. 300-2500 nm, the most commonly used region in agricultural remote sensing, is highlighted with solar radiation graphs outside and inside the earth's atmosphere (solar radiation graph modified from <sup>62</sup>).

Spatial resolution is defined as a measure of the smallest object that the sensor can resolve or the linear dimension on the ground represented by each pixel <sup>65</sup> referred to as Ground Sampling Distance (GSD). Besides the detector array size, Field of View (FOV) and the object's distance from the sensor are also important for determining the spatial resolution. For instance, a thermal camera that uses a 500\*500 array of detectors and has a 90-degree FOV installed on a drone flying at an altitude of 100 meters would yield 40 cm resolution i.e., one pixel contains an object of size 40 cm × 40 cm. However, spectral resolution and spatial resolution are inversely related hence, a tradeoff is involved in having higher resolutions. Some of the most common remote sensing sensors in agriculture will be discussed in the following sections. RGB Camera Analog photography was first started in approximately 1816 <sup>66</sup>, and despite some inherent advantages of analog film photography, such as higher spatial resolution, transition to digital

imaging was inevitable<sup>58</sup>. Digital photography records values from different wavelengths to form a color image. For example, a combination of Blue (~ 450-490nm), Green (~ 520-560nm), and Red (~ 635-700nm) would form an RGB image. Sensors based on this band combination are referred to as RGB cameras with the primary purpose of mimicking the human eye in the digital world. These cameras are readily available off the shelf and have been used in many agricultural studies. RGB cameras are extensively used for studying phenomena in which plants show visual symptoms such as diseases that affect the color composition of the leaves and visible pests or fungi on the leaves<sup>67</sup>. Sometimes, a camera is sensitive to all (or a large portion of the) wavelengths in the visible range that produce panchromatic images, which usually have higher spatial resolution than images created by separate bands. This is because detectors on panchromatic cameras receive cumulative energy from the whole spectral range, and, as a result, smaller detectors can be utilized and still sustain a high signal-noise ratio. Overall, images acquired in the visible region, whether panchromatic or RGB, are endowed with a high spatial resolution that makes these images a perfect choice for studies that need the most details<sup>7</sup>. Moreover, RGB cameras have been widely utilized for Greenness identification using various visible spectral indices as described in the following table:

*Table 1-3- Common vegetation indices used for Greenness Identification using RGB cameras*

Index name	Index Formula	Equation number	reference
The Excess Green index	$ExG = kG - (R+B)$ , $1.5 < k < 2.5$	Eq. 1	68
The Excess Green Minus Excess Red index	$ExGR = ExG + G - 1.4R$	Eq. 2	69
The vegetative index	$VEG = g/R^a B^{1-a}$ , $a \approx 0.66$	Eq. 3	70
The Color Index of Vegetation Extraction	$CIVE = 0.4R - 0.8G + 0.4B + 18.8$	Eq. 4	71
The combined index	$COM = aExG + bCIVE + cVEG$ , $a \approx 0.36$ , $b \approx 0.47$ , $c \approx 0.17$	Eq. 5	72

Various combinations of R, G, and B bands are intended to minimize the environmental and lighting effects to achieve the best segmentation of green vegetation from the rest of the image. However, their unstable thresholding limits the usage of these indices. Cameras that take advantage of at least one band in the Near-Infrared (NIR) region, such as Colored Infrared (CIR) or multispectral cameras, perform significantly better than RGB cameras that rely solely on visible region, in terms of vegetation segmentation<sup>73</sup> and canopy cover estimation throughout the season<sup>74</sup>.

### 1.3.2 Multispectral

A considerable amount of information lay beyond the visible range, where colors lose their meanings. Multispectral remote sensing takes advantage of the most informative bands within and outside the visible region. Multispectral sensors work similarly to RGB cameras, usually with 3-10 bands<sup>75</sup>. In fact, by some modifications, RGB cameras can be turned into a simple multispectral. For example, a filter can be added to block the red band and instead allow the NIR band<sup>76</sup>. However, most multispectral cameras include several sensors and lenses, and each sensor is sensitive to one spectral band. For example, the Micasense Red-Edge camera, that is a common multispectral camera in agricultural remote sensing, uses 5 separate sensors and lenses to capture NIR (842 nm center), red edge (717 nm center), red (668 nm center), green (560 nm center), and blue (475 nm center) bands with bandwidth from 12 to 57 nm<sup>77</sup>. Bands outside the visible region are not defined by color as they do in the visible region. As a result, colors are assigned artificially to represent the intensity in bands outside the visible range called “Band combinations”. For instance, an image in which the NIR band is displayed in red, red in green, and green in blue is called a standard false-color composite that can effectively map healthy vegetation<sup>78</sup>. Similar band combinations can estimate various plant parameters such as leaf area, leaf chlorophyll content, ground cover, and biomass<sup>79</sup>.

Vegetation Indices (VI), ratios or linear combinations of spectral reflectance in two or more bands, are among the most used tools in multispectral remote sensing. VIs exploit vegetation's unique reflectance properties to infer biophysical properties related to plants maximizing sensitivity to the vegetation characteristics while minimizing confounding factors such as soil background, directional, or atmospheric effects<sup>80</sup>. Numerous VIs have been defined for various purposes, including the Normalized difference vegetation index ( $NDVI=(NIR-Red)/(NIR+Red)$ ), which is the most distinguished index in remote sensing, derived from the combination of NIR and Red bands. A comprehensive review of the typical vegetation indices is presented at<sup>81</sup>. Although most VIs combine two or three bands, some use more bands. In this regard, unlike UAS-based multispectral sensors that use a small number of bands, some satellite-based spectral cameras are designed to measure more bands than regular multispectral cameras

(more than ten bands) that are referred to as superspectral sensors such as Moderate Resolution Imaging Spectroradiometer (MODIS) <sup>82</sup>. In this dissertation, superspectral and hyperspectral will be used interchangeably.

### 1.3.3 Hyperspectral

During the 1980s, scientists developed an instrument that was able to collect about 200 sharply defined spectral bands. This new invention was the emerging point of hyperspectral remote sensing <sup>58</sup>. Hyperspectral and multispectral imaging vary mainly in spectral resolution and bandwidth. Usually, multispectral sensors measure a limited number of bands (less than 15 bands) with bandwidths ~10-20 nm, while hyperspectral sensors measure hundreds or even thousands of bands in the visible-NIR region (usually from 200-2500 nm) with bandwidth ~0.1-10 nm.

Hyperspectral cameras are more expensive and complicated than multispectral and RGB cameras that limit their regular applications. However, they provide detailed information about each band's reflectance in a wide spectral range that can be used to pinpoint the most informative bands for a specific phenomenon<sup>83</sup>. For instance, the Chlorophyll Absorption Ratio Index (CARI), a strong chlorophyll indicator in plants, uses three relatively narrow bands in the green and red regions<sup>84</sup>, discoverable only with a hyperspectral scan. However, once discovered, an inexpensive camera can be devised to capture the required bands only. Moreover, most external or internal factors somehow affect plants' reflectance that is not entirely identified yet. As a result, many standard reflectance libraries for various materials, including plant leaves, are collected and used as a benchmark to answer the different phenomenon's effects on spectral response. Figure 1.4 shows the leaf reflectance of a healthy and a nematode stressed walnut leaves and a healthy almond leaf from UC Davis Digital Ag lab datasets. Since water forms a significant portion of leaves (more than 90% in most healthy leaves), the water absorption bands are noticeable in reflectance graphs. In the reflectance graph, both the shape and magnitude should be considered.

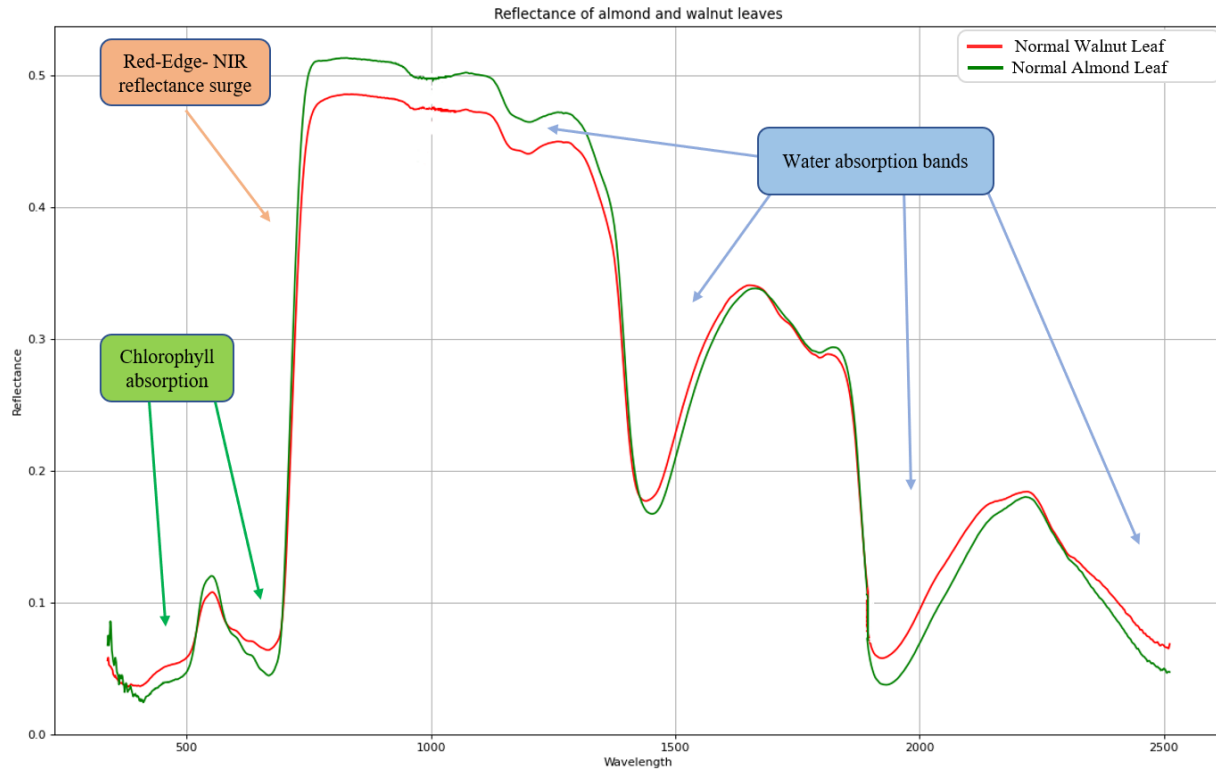


Figure 1.4- Leaf reflectance of a healthy walnut leaf and a healthy almond leaf marked with notable features. Under stress condition magnitude and shape of the spectral response will vary. Data from UC Davis Digital Ag lab datasets.

### 1.3.4 Thermal

The infrared spectral region is usually divided into several subdivisions based on their wavelength with approximate boundaries. However, another subdivision system is based on the radiation type: reflected infrared and emitted infrared<sup>64</sup>. In spectral regions with noticeable sun radiation (e.g., NIR-SWIR, see Figure 1.3) the reflected energy dwarfs the emitted energy marking this region as the reflected infrared<sup>85</sup>. On the other hand, emitted infrared, also known as thermal infrared, is based on black body radiation. Thermal infrared wavelength starts from 3  $\mu\text{m}$  and goes as high as 50  $\mu\text{m}$ . However, reflected sunlight can easily tamper the 3 - 5  $\mu\text{m}$  region during daytime imaging. Additionally, atmospheric absorptions block most other regions leaving 8 - 14  $\mu\text{m}$  the only favorable atmospheric windows for thermal imaging<sup>85</sup>. In fact, some cameras are designed to be sensitive to several regions, turning them into multispectral thermal cameras. NASA's Thermal Infrared Multispectral Scanner (TIMS), for example, measures 6 bands in the 8.2–12.2  $\mu\text{m}$  spectral region<sup>86</sup>.

Thermal cameras interpret the surface temperature based on the energy received in two ways: direct and indirect measurements. Direct measurement cameras, also known as cooled cameras, take advantage of quantum detectors cooled to cryogenic temperatures (close to 77 K). On the other hand, uncooled cameras operate within the ambient temperature and rely on thermal detectors to indirectly measure the temperature<sup>87</sup>. Uncooled cameras have a lower spatial resolution, sensitivity, and shutter speed than cooled cameras, but price, size, weight, and operation condition make uncooled cameras more convenient on sUAS and for remote sensing. Compared to reflective region cameras (RGB and multi/hyperspectral), thermal cameras are inferior in resolution, regardless of their significant advances in recent years. For instance, sensors used at <sup>88</sup> that were mounted on an sUAS flying at 70 m AGL yielded ground resolutions of 1 cm/pixel, 4 cm/pixel, and 9 cm/pixel in RGB, multispectral and thermal images, respectively, showing that thermal imaging was nine times coarser than RGB imaging. Thermal imaging becomes even more challenging in higher altitudes due to atmospheric disturbances. For example, environmental variability (e.g., light intensity, temperature, relative humidity, wind speed)<sup>9</sup> and undesired incident radiation <sup>89</sup> can alter the thermal data. As a result, the spatial resolution of satellite-based thermal imagery is usually tens of meters (100 meters at Landsat 8, for example). In general, thermal imagery still suffers from the coarse resolution, higher price, and complexity of the calibration process—however, its beneficial information outweighs its shortcoming.

Measurement of radiation within the thermal region offers unique advantages that make it an indispensable spectral region for agricultural remote sensing. For example, some crops' water and nutrient stress symptoms are detectable earlier in the thermal region than in the visible range<sup>90</sup>. As a result, canopy temperature can be used as a gauge of the overall plant health. In general, canopy temperature is a function of atmospheric evaporative demand and crops' water/nutrition status. This fact has established a foundation for numerous studies investigating the effects of drought, deficit irrigation, and heatwave on plants. Besides that, thermal imagery has demonstrated a good potential for calculating and validating other vegetation metrics such as Leaf Area Index (LAI = leaf area/ground surface area) and chlorophyll content <sup>91</sup>.

### 1.3.5 Lidar

Light Detection And Ranging (LiDAR), also known as laser altimetry, is an active remote sensing technology that determines ranges (i.e., distances) by measuring the roundtrip time of a laser pulse that travels between a sensor and a target object <sup>92</sup>. Lidars use a narrow bandwidth, around 1-2 nm, with high intensity and minimal divergence (less than 1 mm per meter). The high intensity of laser beam enables lidars to penetrate through leaves and even canopies to reach branches or soil and have multiple return signals. Each pulse illuminates a near-circular point (or area) on the ground, referred to as footprint. Depending on altitude, footprint ranges from below 10 mm for sUAS mounting lidars (example: Phoenix LiDAR Systems Ranger-HA) to tens of meters for satellite-based lidars (example: ~30 m - Global Ecosystem Dynamics Investigation (GEDI) and 70 m for Geoscience Laser Altimeter System (GLAS)). The returned signals will contain height information of all objects within the footprint in the order of their height. For instance, if a footprint contains a tree, the first returned signal will be from the top of the canopy, then the lower branches, and finally from the trunk or the ground, producing a vertical profile (discrete or continuous). Since most of the last returned signals would be from the soil, Digital Terrain Model (DTM, bare-earth model) is one of the lidars' useful outcomes.

Lidars rely on an accurate positioning system (usually RTK-GPS) to first calculate their own location and then that of the points in footprints. In terms of scanning, lidars work similarly to the line scanner and point scanner sensors. As a result, the distance of footprints on the ground in the x and y direction depends on the platform's forward speed and angular step between consecutive laser shots. In low altitude lidar applications, i.e., sUAS platforms, footprints might overlap, generating millions of accurately georeferenced points from the scanned area called point cloud or mass points. The point cloud can be used to extract accurate physical characteristics of the objects in the area, such as plants' volume and height. At higher altitudes, however, footprints neither overlap nor form a point cloud, but they form a grid of footprints with cross-track and along-track distances.

Although, in theory, lidars can work in any wavelength, depending on the application, one band will be selected to be used as a single spectral or several bands in newly emerging, multispectral lidars <sup>93</sup>.



Multispectral lidars take advantage of differences in penetration for different wavelengths to simultaneously extract spectral and vertical profile information. However, multispectral lidars are not fully operational yet, and single-band lidars are typical of most agricultural remote sensing applications. Two of the most common wavelengths used in lidars, especially low altitude lidars, are 905 and 1550 nm; each has pros and cons. The main advantages of 905 nm are lower sensor cost and less attenuation. However, 1550 nm is safer for human vision, allowing lasers with a considerable radiant energy per pulse<sup>94</sup>. As mentioned earlier, other wavelengths might be used as well. For instance, GLAS and GEDI use 1064 nm and 532 nm simultaneously.

Although UAS- based lidars offer data in astonishing spatial resolutions (millimeter scale), they suffer from several disadvantages: 1) Processing millions of data points is computationally expensive and needs substantial computational resources, 2) Most of the time, lidar data need accompanying images or videos for interpretation. 3) Prices for the software processing lidar data could go as high as the sensor itself or even higher. Nonetheless, with advances in computer hardware and software, more vendors are offering lidar-related products such as software, hardware, and consulting packages, and more affordable prices are anticipated.

### 1.3.6 Radar

Radar (Radio detection and ranging) works similar to LiDAR in transmitting electromagnetic signals and detecting the returns. However, radars use short wavelengths of radio region from 0.1 mm to 1 m, known as microwave region (see figure 1.3). Due to the long wavelength, radar signals can penetrate through clouds and other particles in the sky, forming an all-weather sensor. Moreover, each frequency (in radars, usually frequency is used rather than the wavelength) can penetrate through objects to a different extent; thus, it can reveal specific information. For example, frequency of 8-4 GHz, known as C-band, contains lots of information on vegetation dynamics and agricultural data, while higher frequencies 18-12.5 GHz, known as Ku Band, are suitable for crop separability<sup>95</sup>. In addition to frequency, polarization and incident angles are also important parameters in radar studies.

Diverging nature of radar signals requires large antennas to collect the back-scattered signals. This limitation is improved by Synthetic Aperture Radar (SAR), in which a longer antenna is electronically “synthesized”. This radar technology has been mounted on satellites and aircraft platforms such as UAVSAR, used for vegetation mapping, soil moisture, and crop separability on a large scale<sup>96</sup>. Although most of the reported remote sensing studies using radar are satellite-based or airborne, recently, some prototypes of lightweight radars mounted on sUAS were used for high-resolution (1600 points/m<sup>2</sup>) radar mapping<sup>97</sup>. However, radars have a long way to reach the popularity of optic sensors mainly because the world is less known in radio frequencies.

## 1.4 Applications

The sensors introduced in the previous section can be deployed for dealing with an extended range of problems such as water management, which is a global concern, or region-specific problems, such as salinity. In this section, the most common remote sensing applications are classified into seven groups: water status studies, disease detection and control, yield mapping and prediction, nutrient management, phenotyping, soil and salinity studies, and other managerial practices. Some of these applications have gained more attention than others in nut crops. For instance, as shown in table 2, more than half of the papers (11 out of 20) focused on water status representing the significance and severity of water management problems in agriculture. On the other hand, only one paper studied disease detection and control, and one aimed at yield mapping and prediction. The rest of the papers focused on other managerial practices. The numbers might show the relative importance of the applications in nut orchards. However, according to the general purpose applications, an increase in less common applications is anticipated<sup>98</sup>. In the following, each application is reviewed in depth.

### 1.4.1 Water Status

Water status is an essential factor in plant monitoring since it is an indicator of how well a plant is functioning. For example, it can be used for determining drought and disease resistance genotypes, irrigation planning, and it plays an important role in blossom timing. However, due to the dynamic nature of plants, measurement of water status is not very straightforward and can be considered as a function of

multiple environmental parameters including, but not limited to, ambient temperature, wind speed, solar radiation, especially photosynthetically active radiation (PAR), sun azimuth angle, humidity, and vapor pressure deficit<sup>99</sup>. As a result, water status might differ for individual plants in a field or even individual leaves of the same plant (usually leaves under sunlight are dryer than those in shadow).

Plant water status has a direct relationship with plant transpiration, mainly by stomatal conductance<sup>100</sup> [69], and evaporation, either from soil or other parts of the plants such as stems. The sum of evaporation and transpiration is called evapotranspiration (ET); an accurate estimation of ET with high spatial and temporal resolutions is the foundation of irrigation management systems<sup>101</sup>. ET can be estimated in a variety of ways; I) by using a lysimeter which works based on weighing the moisture change in the soil and its vegetative cover, II) by directly measuring the upward fluxes of moisture away from the surface with taking simultaneous measurements of vertical velocity and humidity by devices (atmometer or evaporimeter) that have a high-frequency response, and III) by indirectly deriving from energy balance equation of net radiation, soil heat flux, and sensible heat flux which will result in the energy available for the actual ET<sup>102</sup>. Although these methods can estimate ET with high accuracy, the equipment (e.g., ET tower) is usually expensive, their estimations are limited to the surrounding area, and they are not able to represent all heterogeneity within an agricultural field<sup>37</sup>. As a result, in practice, ET is estimated at a reference surface (usually alfalfa or grass) under well-watered condition, and then crop coefficients are applied to calculate a rough estimation of ET for a specific crop at a specific stage of growth. For example, the crop coefficients of almond are 0.40 at the initial stage, 0.90 at mid-season, and 0.65 at the end of the season<sup>103</sup>. Several research projects have tried to improve ET estimations by taking advantage of remote sensing data. For example, in a study to improve the spatial resolution of ET estimations over an almond orchard, Landsat images were combined with reference ET networks. With this method, they could estimate daily ET within the orchard (at 60\*90 m spatial resolution- 2x3 pixels) by R2 of 0.87 compared to ground measurements<sup>37</sup>. However, even though vital, high resolutions of the ET alone (that does not account for different infiltration rates due to soil type variability) are not sufficient for

monitoring water stress of individual trees and PA practices. So, other water stress indicators are also required.

Water stress, also known as water-deficit stress or drought stress (differs from the excess water stress), is a state in which the amount of water received by the plant is less than its need for an optimal ET<sup>104</sup>. Plants, as living organisms, respond in various ways to water stress, and those responses can be used as indicators to measure and quantify water stress. Indicators widely used include a decrease in leaf water potential<sup>105</sup> and an increase in canopy temperature<sup>9</sup>. Other indicators, that are used for research purpose, include stomatal conductance<sup>100</sup>, gas exchanges<sup>56</sup>, sap flow<sup>106</sup>, photosynthetic rate, net assimilation rate<sup>107</sup>, transpiration rate, Photochemical Reflectance Index (PRI)<sup>108</sup>, natural frequency in vibration of leaves<sup>109</sup> and intercellular CO<sub>2</sub> concentration<sup>110</sup>. Among these indicators, those with the potential to be used in automated platforms and on large scales are of great interest. Some studies have used MS imaging as an indicator of water stress and introduced indices such as:

$$\text{The Normalized Difference Water Index - NDWI} = (R_{860} - R_{1240}) / (R_{860} + R_{1240})^{111} \quad (\text{Eq.1})$$

$$\text{The Water Band Index - WBI} = R_{970} / R_{900}^{112}, \text{ and} \quad (\text{Eq.2})$$

$$\text{The Normalized Multi-band Drought Index - NMDI} = (R_{860} - R_{1640} + R_{2130}) / (R_{860} + R_{1640} - R_{2130})^{113} \quad (\text{Eq.3})$$

As it is clear from their constituent bands, all these indices take advantage of the infrared region and water absorption bands to estimate water status. However, estimation of water status and stress using thermal data is, by far, the most studied method. Thermal imaging works based on the assumption that transpiration is an energy-demanding process that linearly reduces the surface temperature of leaves and vegetation, so water status can be estimated indirectly<sup>98</sup>. The Crop Water Stress Index (CWSI) is one of the widely used indices that is based on thermal data and is defined as follows<sup>9</sup>:

$$\Delta T_{c-a} = T_c - T_a \quad (\text{Eq.4})$$

$$CWSI = \frac{\Delta T_{c-a} - \Delta T_{wet}}{\Delta T_{dry} - \Delta T_{wet}} \quad (\text{Eq.5})$$

where  $\Delta T_{ca}$  is the canopy- air temperature difference at the measurement moment.  $\Delta T_{dry}$ , and  $\Delta T_{wet}$  are when the crop has the stomata fully closed (drought condition) and when it is fully transpiring (well-

irrigated), respectively. As the formula indicates, segmentation of canopy from the surrounding area is needed to gain a correct estimation. Since the camera's distance from the target surface affects GSD, low-altitude platforms are preferred. Lower resolution images will return mixed pixels that include the values from the canopy, soil, and background elements. As a result, the higher the resolution, the higher the accuracy in the analysis, estimations, and predictions<sup>48,114</sup>. Hence, thermal images taken from satellites lack the resolution required for PA activities and CWSI in particular (Currently, satellites deliver thermal images with a resolution of tens of meters, the best resolution is for Landsat7 with 60 m). Consequently, studies using low altitude platforms and ground-based thermal imaging has been carried out for various crops, and in most of them, CWSI demonstrated satisfactory results.

Additional to the resolution of thermal imagery, timing and direction also affect the results of CWSI and other water status-related studies. Based on the literature, CWSI works best around noon. The canopies' segmentation from the soil and background is quite challenging in the early morning due to subtle temperature variation<sup>115</sup>. It is also important whether images are taken from the sunny or shaded side of the canopies since results might vary for sunlit and shaded areas<sup>110</sup>. CWSI has shown good correlations with Stem Water Potential (SWP) in pistachio<sup>28,109</sup>, almond<sup>26,105</sup>, and many other crops<sup>114</sup>. SWP is the most widely used plant water status indicator for irrigation scheduling in fruit trees and grapevines<sup>116,117</sup>. Besides SWP, CWSI is also correlated with other water status indicators such as stomatal conductance and leaf water potential<sup>118, 26</sup> that are used for irrigation management at farm scale<sup>28</sup>. Estimating water potentials is a big step forward since direct measurement using pressure chambers is very labor-intensive and time-consuming, requiring at least 10 minutes for each leaf<sup>101, 106</sup>.

When the water status of plants is estimated on a large scale, then other managerial and long-term goals such as the possibility of fighting water scarcity by drought-resistant genotyping, avoiding soil salinization, foiling nutrient losses, and practicing site-specific water supply would be attainable<sup>98</sup>. Additionally, it can help optimize the irrigation process, increasing yield efficiency. Studies on almonds and pistachios, for example, have revealed the positive effects of irrigation on both yield (lbs/ac) and nut size (g/nut)<sup>119</sup> even though they have a reputation of being drought-tolerant and producing modest yields

with very little water <sup>7</sup>[14]. In a study on almond, authors reported 96%, 35%, and 40% increase in the yield, nut size, and the number of nuts per tree, respectively, by 5-inch irrigation compared to no irrigation. While irrigating with 10 and 40 inches did not make much difference<sup>1197</sup>. Results of <sup>28</sup> attest to the feasibility of using high-resolution (35 cm) thermal imagery for integrating the crop response in management at farm scale.

#### 1.4.2 Disease control

Regardless of its abiotic or biotic nature, plant disease can be defined as “anything that prevents the plant from performing to its maximum potential”, reducing its economic or aesthetic value <sup>120</sup>. Biotic agents refer to microorganisms and parasitic plants that usually are called pathogens. The nonliving environmental and nutritional factors and chemical substances, on the other hand, are called abiotic agents<sup>121</sup>. Plant disease will occur if all the following unfavorable conditions are satisfied simultaneously.

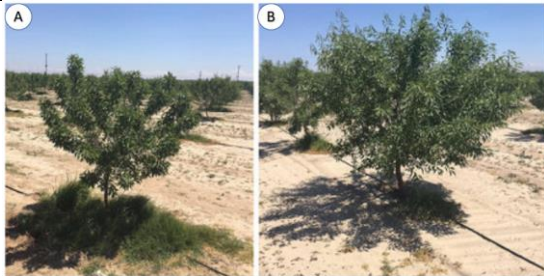

I) the plant becomes susceptible to disease for any reason. II) the plant pathogens are present in the vicinity. III) the environmental condition is favorable for the pathogens’ activity<sup>120</sup>.

Lucas and Campbell classified disease management methods into three main categories: prevention, genetic resistance, and chemotherapy<sup>121</sup>. Prevention can be achieved by proper site selection, planting date, or even proactive chemical application, to prevent the satisfaction of at least one of the three conditions mentioned. Genetic resistance management, which attracts increasing attention, is to identify the resistance sources genes in the plants and breed them to be naturally immune to a specific disease (will be discussed more in the phenotyping section)<sup>122,123</sup>. Chemotherapy or using synthetic chemicals is one of the oldest and the most widely used methods for disease control in plants. Although synthetic chemicals have been promising for food security and economic benefits, studies indicate that farmers tend to use more pesticides than needed <sup>124</sup>, resulting in severe side effects<sup>125</sup>. Moreover, excessive use of some pesticides makes pathogens become utterly resistant to that agent or decrease sensitivity<sup>126</sup>.

Precision Pest Management (PPM) can help alleviate the hazards of excessive pesticide applications. PPM, which is a subset of PA, can be defined as the application of the right amount of pesticide at the right place in the field and at the right time<sup>127</sup>. Two main steps of PPM are I) using remote sensing

techniques (mainly aerial imagery) to obtain site-specific information and II) providing localized solutions using variable rate applications<sup>128</sup>. The first step, which is similar to other PA practices, uses the sensing methods discussed in the sensors section. RGB cameras are widely used for visually detectable diseases and pests where leaf color changes due to a reduction of pigments that absorb light, thus increasing reflectance in specific bands of the visible region<sup>129</sup>. Multispectral sensors are suitable when the disease affects the photosynthesis rate decreasing detectable green biomass by reducing the reflectance of the Red-Edge/infrared region<sup>130</sup>. Hyperspectral sensors usually are used when pigment degradation and structural changes happen, and we are interested in determining the most informative wavelengths to detect disease effects<sup>9029</sup>. Additionally, hyperspectral imaging offers better opportunities for early detection and even discrimination of disease type than other methods. Changes in leaf structure and chemical composition of the tissues due to disease are somehow pathogen-specific. Hence, the leaf spectral signature varies when infected by different pathogens. As a result, following the footprints can lead to the source pathogen. Several studies proved that hyperspectral scanning could distinguish different fungal infections<sup>131</sup>. Thermal cameras, on the other hand, can only discriminate plants that have a higher temperature for any reason including disease<sup>132</sup>. Other sensors, such as lidar, can be used to monitor diseases that affect plants' physical properties<sup>133</sup> and growth rate to indirectly correlate to long-term diseases, such as nematodes<sup>134</sup>. Sometimes, several data from different sensors are processed in unison to get as much data as possible. For instance, at<sup>135</sup>, visible, infrared, and thermal cameras were used together to detect Huanglongbing in citrus. Table 1-4 shows two examples of remote sensing studies for disease detection and control in nut orchards.

Table 1-4- Examples of remote sensing application for disease detection and control in walnut and almond.

Orchard	Disease	Suggested or Proposed Sensor	Description
Walnut/ Almond	Root Lesion/ Knot Nematode	Lidar or photogrammetry for growth rate Hyperspectral for informative band detection	 <p>Difference in growth rate of almond rootstocks in nematode-infested soil. A) Infected tree B) healthy tree<sup>136</sup>. A similar pattern has been observed in walnut trees, and some rootstocks have shown good tolerance/resistance<sup>123</sup>.</p>
Almond	Red leaf blotch (Prunus amigdalus)	Thermal and Hyperspectral	 <p>Red leaf blotch is a fungal foliar disease widely effected almond production. The recently planted orchards are more susceptible, however, varieties have different level of susceptibility<sup>29</sup>.</p>

### 1.4.3 Yield mapping and prediction

Yield prediction is crucial in agricultural activities from a farm scale to a country or even a global scale.

Market management, fertilizer demand estimation, performance assessment of different cultivars, and timely import and export policies are examples of activities that demand accurate yield predictions<sup>137</sup>.

Conventionally, farmers used their experience and historical data to predict the approximate yield based on the field's current condition. However, for large-scale and economical production, a more reliable and accurate yield prediction method is required. The potential yield (the maximum yield possible) depends on various factors, such as the weather, soil properties, topography, irrigation, fertilizer management, and, more importantly, the plants' characteristics<sup>138</sup>. However, actual yield often falls significantly below potential yield due to one or more limiting factors at each stage<sup>139</sup>. The interplay of numerous factors makes yield prediction a complex problem, especially for alternate bearing nuts. However, these factors can be classified into three major categories: environmental factors, genotypic factors, and interaction of them<sup>140</sup>. The genotypic and interacting factors will be discussed in the phenotyping section.



Environmental factors include but are not limited to weather, precipitation, location of the orchard (mainly latitude and altitude), soil properties, water quantity and quality, and availability of pollinating factors. Studying environmental factors helps to find the limiting parameter and resolve it. For instance, a study on a pistachio orchard revealed that the irrigation water amount, soil soluble magnesium, soil electrical conductivity (EC), leaf phosphorus, and leaf nitrogen were the main determinant factors for yield in order of their importance<sup>141</sup>. A similar study on almond orchards showed that light interception was a highly influential factor in most orchards, so that one percent increase in light interception could increase the potential yield by 57.9 lbs kernel /acre<sup>139</sup>. Although it might not be practical to monitor and incorporate all the affecting environmental factors for yield prediction, remote sensing methods provide a cost-effective monitoring and data collection technique covering many constraining factors<sup>142</sup>.

Remotely sensed data for yield estimation can be classified into three categories. 1) physical characteristics of the trees such as canopy volume, height, and LAI, 2) visually identifiable features such as blossom or fruits, and 3) spectral features. In studies based on physical characteristics, usually, a drone equipped with a high-resolution RGB camera or a lidar collects data to create digital surface models (DSM) and digital terrain models (DTM). Then physical attributes of each tree such as height, crown area, and volume could be extracted<sup>103143</sup>. Additionally, the light interception can be estimated from the physical characteristics of canopies. Yield estimation based on blossom or fruit detection usually takes advantage of the distinct color of the flowers or the fruits to identify them, count them or estimate their percentage. Then, based on the weighted average, yield can be estimated<sup>144145</sup>. These methods heavily depend on image processing techniques as well as machine learning algorithms<sup>146</sup>.

The spectral radiance that is used for a variety of purposes can also be used for yield prediction. For example, the fraction of absorbed Photosynthetically Active Radiation (fPAR, 400–700 nm), a significant factor in yield, can be estimated from spectral data<sup>147</sup>, especially VIs such as the photochemical reflectance index (PRI)<sup>148</sup>.

Although each dataset (physical characteristics, visually identifiable features, and spectral features) can be used individually, in a comprehensive study, a mixture of these data should be used to estimate the yield

in an orchard. For example, Zhang et al. were used orchard physical characteristics, vegetation indices, orchard age, and weather data and used machine learning techniques to fuse data reaching almond yield prediction at the orchard level by  $R^2$  of 0.71 in California<sup>33</sup>. Currently, the main knowledge gap for yield prediction is a method to combine the affecting data of different resolutions and types to predict yield in a holistic picture.

#### 1.4.4 Nutrient management

Nutrient management is the practice of balancing the nutrient demands of a crop with the available sources during the growing season, considering all variations in the field, and maximizing nutrient efficiency while reducing the off-site transfer of nutrients<sup>149</sup>. The primary objective of nutrition management is to accommodate conditions that favor the growth of healthy trees capable of producing top-quality fruit in high quantities<sup>150</sup>. Even though it seems a simple task, nutrient management becomes challenging in practice due to the myriad of factors involved, sometimes factors with long-term effects or even contradicting factors. For example, controlling the runoff prevents the topsoil nutrients from being washed away; however, preventing excess water from exiting a field might increase the nutrient leaching problem, leading to even more severe consequences. As another example of nutrient management complexity, managerial measures, such as fertilizer applications or pruning, each year can affect the nutrient status in the following years, causing a cycling or residual nutrients state<sup>151</sup>. As a result, knowing the field's current condition with as many details as possible helps prepare a suitable comprehensive plan for managerial practices.

Conventionally, two data collection methods were used to obtain information from the orchards' nutrient status: soil sampling and leaf tissue sampling. Soil sampling is conducted either before planting the new orchard to determine the type and amount of lime required and the relative levels of minerals or in existing orchards to provide additional insight for interpreting leaf samplings<sup>150</sup>. However, studies found weak correlations between the results of soil and leaf samples in orchards. Low correlations might be due to shallow sampling depth, mis-selection sampling zones, and mobile nutrients that are stored in various parts of the trees. Additionally, soil sampling shows the "plant available" nutrients that are not necessarily

uptaken by plants. As a result, the focus on leaf-based nutrient analysis and management increased, and some standards were developed in response to noticeable variations in the results of samples collected at different growth stages, with different methods, and with different sample preparation and analysis procedures<sup>152 150</sup>. These efforts established the 'Critical Value' concept in which fertilizers are applied to ensure that leaf nutrient concentrations never fall below the previously established critical concentration associated with optimal yield levels for each plant<sup>153</sup>.

Based on the critical value concept, at least 14 mineral elements are identified as required for adequate nutrition of plants; six macronutrients and eight micronutrients <sup>154</sup>. Deficiency in any essential element will restrict the optimum tree function, and a severe shortage of an element presents some symptoms that will persist until the deficiency is compensated <sup>155</sup>. In addition to deficiencies, some other nutrient disorders and imbalances such as N/K – Nitrogen/Potassium- imbalance are identified that can adversely affect plants' performance <sup>156</sup>. Even though the critical value concept has been used widely for diagnosing nutrient deficiency over the past decades, it is now recognized that this approach has serious shortcomings. Some examples of the reported shortcomings are as follows 1) yield-based critical values for most of the minerals/plants are not available, 2) The recommended values does not satisfy the current yield levels, 3) since the standards are based on the leaf samples at the beginning of summer, they are not helpful early in the season<sup>153</sup>. Another fundamental inadequacy of the leaf sampling methodology is environmental concerns, especially regarding excess nitrogen application, leading to nitrate polluted underground waters. Subsequently, new legislations were implemented requiring the growers to apply nitrogen to meet, but not exceed, the annual N demand for crop and tree growth and nut production<sup>33</sup>.

To ameliorate the mentioned problems, recently, a nutrient budgeting based on I) the correct crop's demand (Right rate), II) accurate nutrient uptake time (Right time), III) proper place around the active root zone (Right placement), and IV) the correct form of the fertilizer, i.e., fertilizer, humus, etc. ( Right source), has gained widespread acceptance that is also known as 4R practice<sup>157,158</sup>. However, determining the correct Rs is challenging and needs constant monitoring of the plants and creating a nutrient status map that would be very expensive with traditional methods.

Remote sensing has shown great potential in providing sought-after data for nutrient management and addressing the barriers in site-specific management. For example, a survey in 2013 showed that satellite and aerial imagery for creating nutrient management zones and status maps increased from 31% in 2011 to 40% in 2013 <sup>159</sup>. Similarly, the Web of Science search results shows, Figure 1.1 that nutrition-related papers in agricultural fields are more than doubled during the five years of 2016-2020 compared to the previous five years of 2011-2015.

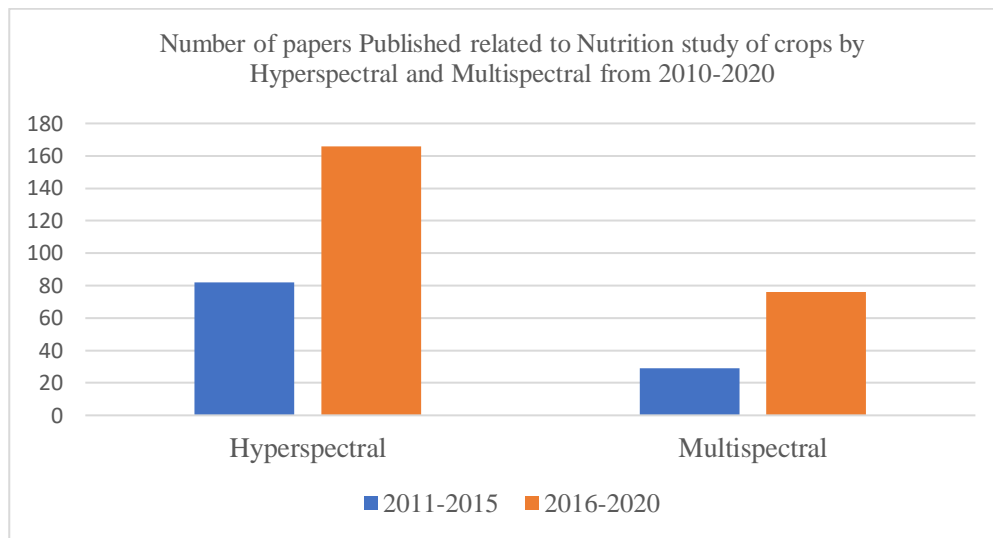


*Figure 1.5- The Web of Science search results from 2011 to 2020 for hyperspectral and multispectral aerial imaging. Results were retrieved by search keywords as follows: 1) hyperspectral (nutrient OR nutrition) (plants OR crops) and 2) (multispectral OR multi-spectral) (nutrient OR nutrition) (plants OR crops)*

Like other remote sensing techniques, the nutrient status estimation and management are mostly based on the plant's spectral reflectance. For a comprehensive comparison and explanation, refer to<sup>98</sup>. Most studies have tried to estimate the nitrogen content at a canopy level using spectral vegetation indices<sup>160 161</sup>. In contrast, as a new approach, some studies employed bands and wavelengths individually as a variable for predicting nutrient status, especially nitrogen<sup>162 83</sup>. Studies showed that leaf nitrogen content could explain up to 76% yield variation in almond orchards over two or three years<sup>163</sup>. However, we could not find any published research on nutrient status estimation by remote sensing techniques in nut trees, and this gap shows an opportunity for future research in this area.

#### 1.4.5 Salinity

Soil salinity is another significant environmental threat to sustainable food production globally. Studies indicate that if necessary measures were not taken, soil salinity's direct economic impacts would exceed \$1 billion annually by 2030, only in the Central Valley, California<sup>164</sup>. Saline soil is generally defined as soil that its electrical conductivity (EC) of the saturated soil-paste extract in the root zone is more than four dS m<sup>-1</sup> at 25 °C and contains 15% of exchangeable sodium <sup>165 166</sup>. Excess salt concentration in soil paste reduces its osmotic potential, which in turn decreases water uptake of the plant by increasing the energy cost of water extraction, transpiration, and photosynthetic rate, and finally decreasing production <sup>36</sup>. The main factors affecting the soil salinity include water quality and irrigation management, the soil's geological nature, excessive fertilization, drainage conditions, rainfall, and ET<sup>167</sup>. As a result, comprehensive management of the field is required to overcome salinity problem in susceptible areas. Among the influential factors on soil salinity, some of them, such as soil's geological nature and drainage condition, can be estimated for a long time by one-time assessment, while the other factors, such as irrigation practices, fertilization, and ET estimation, need ongoing evaluation due to their rapidly changing nature.

Soil salinity can be estimated in different ways. The traditional method of assessing soil salinity by soil sampling is the most direct way, which is expensive and ineffective for large-scale mapping. The remote sensing methods that are more efficient can be divided into two different categories; direct salinity assessment (using electromagnetic induction and soil's electrical conductivity)<sup>168 167</sup> and indirect estimation (form the symptoms of the plants) <sup>169 170</sup>. A crop suffering from soil salinity (in the root zone) might have a different reflectance and ET characteristic than a normal plant. Usually, an increase in the visible range and a decrease in the near-infrared (NIR) region of the electromagnetic spectrum are expected<sup>167</sup>. Vegetation indices such as NDVI and Canopy Response Salinity Index (CRSI) can be used for salinity quantification <sup>171</sup>. However, a similar change in spectral response might happen due to various reasons such as nematode, drought, and other stressors. As a result, it might be impractical to link the spectral features to a particular cause without additional knowledge about the field and plants condition.

A data fusion and analysis method that takes as many variables as possible and concludes based on the combined inputs would be inevitable in such studies.

#### 1.4.6 Phenotyping

The genetic composition, i.e., DNA sequences, of an organism is called a Genotype and can be determined by the genotyping process. However, plants with the same genotype might display completely different traits due to the environmental condition in which the plants are cultivated. All the plant's observable characteristics (the effects of genotype and environment combined) are called phenotype<sup>172</sup>. As a result, monitoring the characteristics of as many crops as possible with different combinations of genotype and environment would help determine the most efficient phenotype (the best genotype for a specific environment). The efficiency here can be the yield, size, or color of fruits, disease resistance, drought tolerance, adoption to a specific condition such as salinity, or any desirable trait sought after. It is perceived that phenotyping is one of the primary ways to increase the productivity of crops worldwide<sup>173</sup>. Therefore, the necessity for high-throughput data acquisition of trait data is inevitable. All the remote sensing applications discussed in the previous sections can be classified as a sub-set of phenotyping, so the methods used for those applications are also applicable for phenotyping. For example, a walnut orchard consisting of several cultivars can be monitored for nematode resistance by applying different treatments, and phenotypic data determine the most vigorous variety. Similarly, almond orchards can be monitored to determine the cultivars with the most desired bloom phenology<sup>20</sup>.

### 1.5 Data processing and analysis

After designing the experiment and selecting a suitable platform and sensor for the intended application, data needs to be collected, processed, and analyzed. Although there might be a slight difference in how datasets from different sensors are handled, the following steps present a broad pipeline that ensures the analysis's efficacy. This pipeline is divided into three main steps: preprocessing, processing, and analytics. In the following, each step will be discussed in detail.

#### 1.5.1 Preprocessing

Data acquired remotely are affected by several factors such as sensor characteristics, illumination, geometric alignments, and atmospheric conditions. In order to obtain temporally and spatially consistent

field results, data must go through a standard preprocessing pipeline. Throughout preprocessing, raw data (that are mainly in the form of Digital Numbers (DN)) need to be converted to meaningful values and attributed to their real-world correspondents such as reflectance or temperature. Radiometric calibration, converting raw data to physical units, and removing noise caused by external effects form the first preprocessing step. In the stitching step, images of different locations on the ground are laid and stitched together to generate an orthomosaic of the whole study area. Aligning all the data and staking them so that a specific position contains data from all the sensors, spatially and temporally, creates the georeferencing step.

#### *1.5.1.1 Radiometric Calibration*

Depending on their type, sensors might produce a single value per measurement, such as a point distance, a 2D data matrix, such as a single band image, or a 3D data cube, such as a multiple-band image. The FOV of the sensor determines the spatial extent that is going to be mapped on a two-dimensional array. Each element on the data arrays contains a DN value proportionate to the electric charge received at capture time. However, the values do not necessarily express the objects' actual radiation or reflectance due to several error interferences either by sensor operation or environmental factors referred to as noise. In satellite-based sensors, especially state-sponsored satellites, all calibrations and corrections are usually scrutinized prior to launch and are available as metadata to the users. However, private platforms tend to be more vulnerable to miscalibration effects.

Sensor noises emerge from the electrical, mechanical, and physical arrangement of the sensors that alter the DN values one way or another. For example, some sensors have a gradual increase in DN values horizontally or vertically regardless of the input radiance due to the electrical arrangements of photoreceptors. Besides the electronic noise, the lens and other structures within the sensor might affect the DNs. Vignetting is one of the well-known and prominent effects defined as a radial reduction in brightness from the center towards the image edges<sup>174</sup>. For high-quality fixed focal length lenses, vignetting can account for 30–40% of the intensity difference, and for zoom and wide-angle lenses, it might be even higher<sup>175</sup>.

Dark current is another sensor error source. In theory, if we take an RGB picture in an absolutely dark place, all pixels must be zero. However, in practice, this is not the case due to the noise in circuits, the Charged Couple Device (CCD) noise, working temperature, and other uncertainties. This noise, which can happen in any sensor type, is called dark current or black level noise<sup>176</sup>. However, this noise is usually negligible compared to other error sources if the working temperature and the circuits are almost constant. Understanding the error source and compensating for their effect helps produce more repeatable and accurate results. Most manufacturers provide adjustment matrixes that correct the vignetting and noise effects per band per pixel. Micasense, for instance, provides a formula for compensating the sensor's black-level, the sensitivity of the sensor, sensor gain, exposure settings, and lens vignette effects in their multispectral cameras.

Removing the environmental-dependent errors is the next step. The environmental effects can cause two or three times more errors than the sensor effects<sup>177</sup>. Environmental calibrations are adjustments needed for producing repeatable data in different environmental conditions. Most of the corrections required for satellites are negligible for low altitude flying remote sensing platforms<sup>177</sup>. For example, scattered or absorbed radiation from/by the particles in the atmosphere is usually ignored in lower altitudes. However, other corrections might become necessary when flying with UASs. The solar position with respect to the flight heading and the camera-object angle is an influential factor in the energy received by the sensor<sup>178</sup>. A hot spot in the antisolar point (a point on the ground that falls on the camera-sun line) is another issue that is not a very severe problem in satellite imaging<sup>179</sup> but might become a critical problem in UAS imagery. This problem causes an overexposed area in the antisolar point of the image that gradually decreases by distance, and it can happen even in line-scanner sensors. Although none of the papers in this review have considered the effects of the sun angle and bidirectional reflectance distribution function (BRDF) on the images, the literature suggests the effect is not negligible<sup>98 180</sup>.

Besides the calibrations discussed, the weather condition plays a critical role in the accuracy and the quality of the data gathered. For example, on partly cloudy days, radiance values might change drastically in a glimpse, reducing data reliability. A study showed that poor weather conditions (cloudy,



precipitation) deteriorate the final quality and accuracy of the photogrammetric product by an average of 25%<sup>181</sup>. Even in clear sky conditions, changing irradiance from the sun might affect the results. The two most commonly used methods for dealing with this situation are 1) using reference reflectance panels and 2) using ambient radiance sensors. The reflectance of reference panels is measured twice, before and after each flight, to compensate for the overall irradiance change. However, any sudden solar irradiance changes during the flight will remain uncaught. Using ambient radiance sensors might alleviate this problem. Figure 1.6 summarizes the noise discussed above.

Converting the corrected digital numbers to a meaningful physical unit is the next step. The SI unit of radiance is watt per steradian per square meter ( $W \cdot sr^{-1} \cdot m^{-2}$ ), while a DN has no unit. When DNs are converted to radiance, they can be used in every condition, and long-term comparisons will be possible. Usually, the sensor companies provide metadata that contains the parameters and information required for converting the DN to radiance or reflectance. However, some studies have shown that the factory-provided adjustment parameters of a sensor may change as it is utilized in real-world conditions, so a recalibration process is recommended<sup>182</sup>.

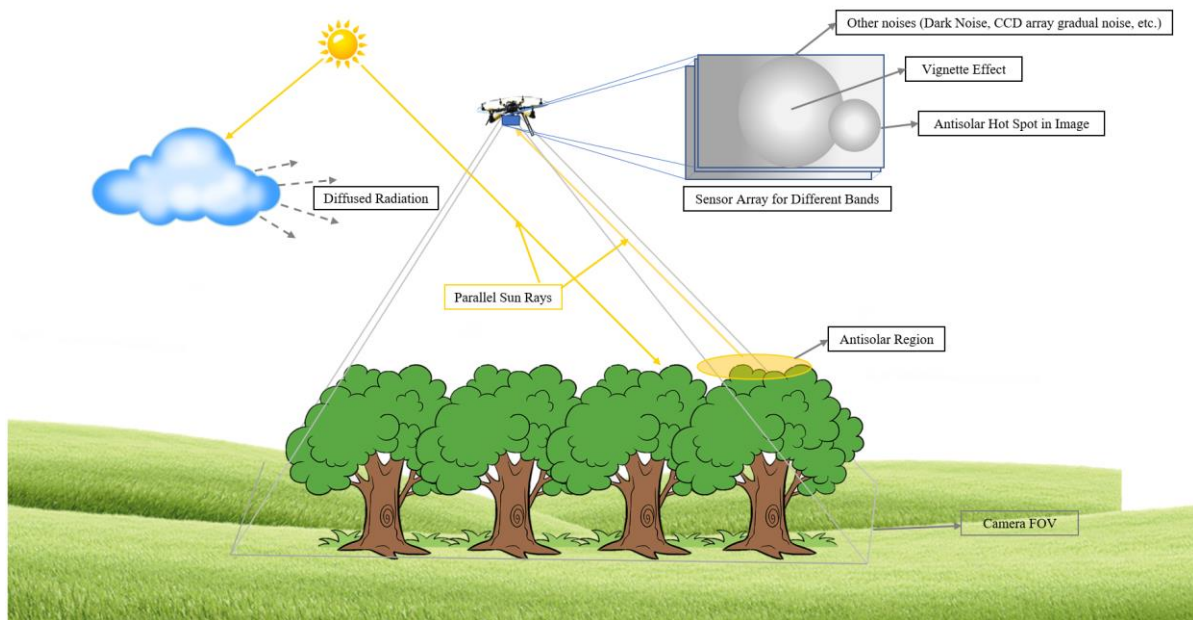


Figure 1.6- Types of noises affecting a remote sensing sensor; Environmental and Sensor-based noises.

Calibration of thermal cameras is slightly different from optic cameras, and usually, ground-based calibration targets (with known temperature) [45] measured by handheld infrared thermometers [79] are reported to be used for temperature adjustment. An accurate calibration guarantees data reliability and reduces the impact of errors on the modeling and interpretation. So, it is essential to perform a precise calibration before data extraction and interpretation.

#### *1.5.1.2 Georeferencing*

Georeferencing (image registration) can be defined as registering image coordinates to a specific geographic coordinate system. As a result, each pixel of the image will correspond to a point (a small area) on the ground and can be shown in geographic software. The output will precisely match the real-world coordinates if the data collection device is equipped with RTK-GPS. Lidar and SAR scanners usually work in this way. However, most of the devices use GPS receivers with more than a meter accuracy. As a result, the recorded data might be off by several meters. In this case, Ground Control Points (GCP, marked points on the ground with known coordinates) are used to align images, and the precision of alignment depends on the number (0.2-0.4 GCPs per acre) and distribution (edges of the study area plus inside the area) of the GCPs<sup>183 184</sup>. If absolute georeferencing is not required and several images need to be registered on top of each other, some prominent mutual features can be used as GCPs to align the images.

Georeferencing can be done either for a single image or for mosaics created using multiple stitched images. Some studies cover the whole study site in a single image avoiding commercial mosaicing software. In this approach, special attention must be paid to the effects of wide-angle imaging in calibration and GSD differences.

#### *1.5.1.3 Mosaicing*

Image mosaicing (also called compositing or stitching) is a technique used since the early days of photography to join two or more images with overlapping regions. Nowadays, image mosaicing is an indispensable part of remote sensing applications due to the extensive coverage of such images. For example, usually, satellite images do not cover the area of interest with a single image, or clouds block

some parts of the image. As a result, images from several dates can be used with mosaicing techniques to reconstruct a mosaic for the area of interest. In UAS applications, mosaicing is even more critical. UASs cover an area using tens or hundreds of relatively wide-FOV images used to generate a mosaic image of the whole area. The wider FOV results in images of the same place that look slightly different due to the view angle, making the mosaicing challenging.

Image mosaicing is still one of the hot subjects, especially for remote sensing applications. The two primary steps for image mosaicing include 1) image alignment and 2) blending<sup>185</sup>. In the alignment step, the common region of the overlapping images are used to align the images on top of each other using either the intensity-based methods, e.g., Normalized Cross-Correlation (NCC), that depend on the intensity of pixels, or the feature-based methods, e.g., Scale-invariant feature transform (SIFT), that rely on some distinct or salient features such as edges and points<sup>186</sup>. After the alignment process, overlapping regions should be blended with minimal artifacts. Discontinuities are often noticeable in the overlapping region resulting from misalignment errors or photometric differences between images. Blending algorithms, therefore, play an essential role in lightening such discontinuities. The blending methods can be classified into three groups: transition smoothing (weighted average of the constituent images), optimal seam finding (the least noticeable boundary detection), and hybrid blending<sup>185</sup>. However, as discussed throughout this chapter, remote sensing applications mostly rely on reflectance data, which are represented as intensity values in images. As a result, blending techniques must be practiced with the utmost precaution to avoid erroneous modification of the original reflectance data. Nevertheless, most of the software used in remote sensing (Pix4D and Agisoft, for example) use images taken with large front and side overlaps and then, based on some mathematical techniques and weighted averaging, create the mosaic files modifying the original data. As a result, for analyses that require precise reflectance values in different bands, employing software that alters the original reflectance values in the blending process is not recommended.

#### 1.5.1.4 *Point cloud and Digital Surface Models*

As discussed in the lidar section, point clouds result from numerous registered points that can represent the shape, size, position, and orientation of objects in space <sup>187</sup>. Processing dense point clouds faces three fundamental challenges: 1) need of powerful computer processing resources to handle hundreds of millions or even billions of points with geometric, colorimetric, and radiometric attributes, 2) lack of any semantic information or linkage among the points (points are discrete data entries), and 3) presence of noise <sup>188</sup>. The point cloud processing can be divided into segmentation and classification. The former refers to clustering points into subsets (typically called segments) based on one or more common characteristics (geometric, radiometric, etc.). In contrast, classification is assigning points to specific classes (labels) according to some predefined criteria [223]. However, the type and nature of the scene, e.g., agricultural versus municipal, can significantly influence the requirements of a data processing algorithm <sup>188</sup>. A comprehensive discussion and classification of all the steps of point cloud processing are presented at [223].

A low-precision alternative for LiDAR 3D reconstruction and point cloud generation can be obtained through photogrammetry. Photogrammetry is the science of making accurate measurements from photographs and using optics' principles, the camera's interior structure, and its orientation to reconstruct dimensions and positions of objects from overlapping images <sup>58</sup>. Usually, this method is applied to data derived from stereo cameras or cameras equipped with GPS and IMU to construct a point cloud by mathematical methods and computer vision techniques such as Structure-From-Motion (SFM) <sup>189</sup>. Additionally, higher image resolution and radiometric calibration of the images used for photogrammetry improve the accuracy of the outcoming point cloud <sup>184</sup>. Other factors that determine the accuracy of the results include i) the algorithm by which the program is extracting data, ii) the overlap of the images, iii) the quality and resolution of the images, and vi) the precision of the positioning and IMU devices used during the flight.

DSMs and Digital Terrain Models (DTM) are two of the most valuable point cloud processing products used to extract canopy structure characteristics. DSM is a land model, including all trees, shrubs, ridges,

and furrows in a 2.5D form in which each point has X, Y, and Z (elevation from the sea level) values. DTM, or bare ground model, is derived from DSM by excluding all objects above the ground. For flat or fixed-slope orchards, DTM generation is straightforward. However, it might be challenging for orchards on uneven terrain or when canopies are too dense that the ground in the aerial view is blocked. Once a DTM was calculated, a Canopy Height Model (CHM) can be driven by subtracting the DTM from the DSM. By compensating for the variations in the field surface, CHM displays all objects and trees on a flat surface (zero line), so the height of the trees would be an absolute number and can be easily compared <sup>190</sup>. Figure 1.7 shows these terms graphically.

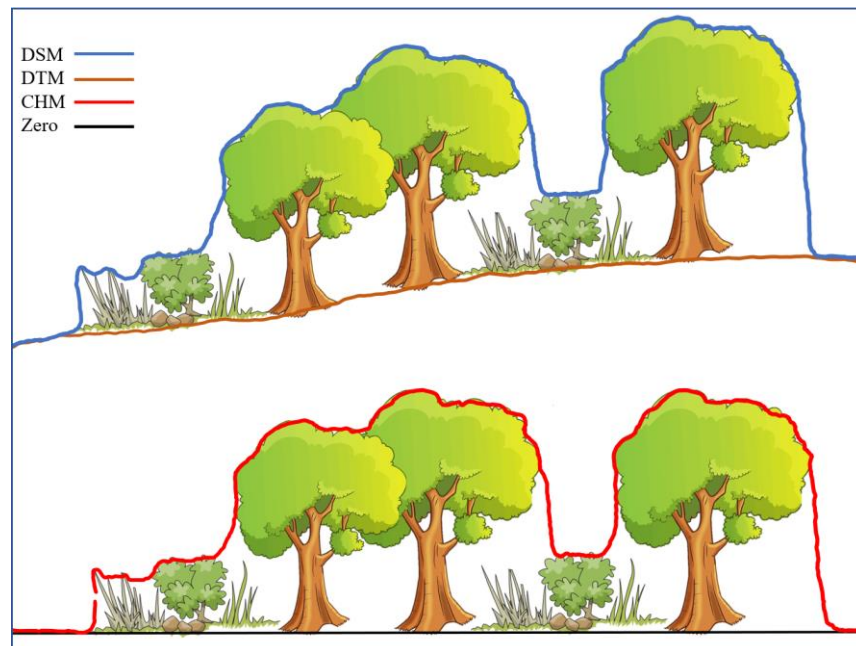


Figure 1.7- Graphical representation of DSM, DTM, CHM, and zero line. DSM and DTM are measured as sea level elevation, while CHM represents the height of each element from the ground level.

Several commercial software, such as Pix4D and Agisoft, are available for photogrammetry processing in an agricultural setting, and 3D models of many orchards reconstructed by this method, e.x., almond <sup>24</sup>. However, a noticeable shortcoming of photogrammetric point clouds is the weak penetration power of optic cameras compared to laser scanners, limiting information obtained from lower layers of canopies.

### 1.5.2 Processing

When data passed through the preprocessing steps, the main processing steps start. Processing here is referred to the noise removal and extraction of specific features and traits from datasets to be used in

analytics. The processing steps might vary for different applications, and each problem requires specific considerations. However, the overall steps are presented in the following.

#### *1.5.2.1 Noise removal and segmentation*

One of the challenging steps in processing remote sensing data is to extract knowledge from raw data that includes noise ranging from band-level to pixel-level. In satellite-based multispectral sensing, for example, some bands are impaired by atmospheric gases and particles, making them unsuitable for ground remote sensing, although they are essential for atmospheric studies. These bands are referred to as noisy bands and should be excluded from further processing. Additionally, some data elements of the target bands in the region of interest might contain unreasonable data or No Data (None) values that must be identified and solved before analysis to ensure reliable results. In pixel-level noise elimination, two approaches are imaginable: sub-pixel Spectral Mixture Analysis (SMA) or pixel segmentation. In theory, each pixel value would be a linear combination of pure spectral signatures of its constituent components (i.e., endmembers), weighted by their subpixel fractional cover<sup>191</sup>. In large pixels, each pixel contains several endmembers. SMA could be used to estimate the percentage of endmembers within each pixel and in the whole region of interest. In fine pixel sizes (cm level ,e.g.), usually, the mixed pixels (such as canopy boundaries) would be segmented out along with other undesirable pixels<sup>26 30</sup>. As a result, segmentation is an essential and influential part of processing.

The segmentation process is even more challenging when the trees are in the early growth stage and the canopies are sparse. In this situation, most pixels will contain mixed spectral from the vegetation and the background (mostly soil). Thus, either using an SMA or collecting higher resolution imagery is inevitable to ensure data coming from the vegetation only. For this purpose usually, masks based on vegetation indices such as NDVI <sup>7</sup> and Excessive Green Index (EGI) are used<sup>162</sup>. However, using vegetation indices as a means of masking has two drawbacks: (1) losing some data variation and (2) the need for a dynamic threshold. Using spectral-based masking techniques overlooks some variations in the dataset that might contain valuable information. NDVI, as an example, has been widely used for masking with different thresholds based on the crop and field condition. By thresholding, all data below a value will be excluded

regardless of their origin: soil or an unhealthy leaf. As a result, segmentation methods that do not depend on spectral characteristics, such as using the canopy's 3D structure or point cloud, are of great interest<sup>192</sup>. Additionally, a fixed threshold cannot handle all datasets, and a dynamic threshold might be needed, making the processing and the results less objective. For example, even a subtle change in NDVI thresholding could alter the intended model significantly<sup>7</sup>. As a result, making a decision/conclusion based on absolute values of vegetation indices might be questionable.

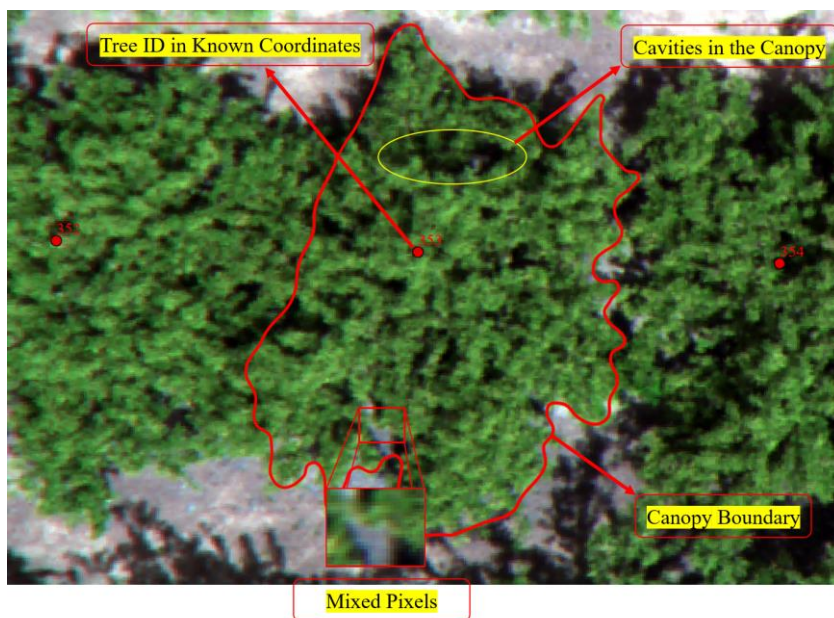


Figure 1.8 - Image segmentation of an aerial multispectral image from an almond orchard. An individual tree canopy is isolated, and a unique tree ID is designated. Cavity region, shadowy areas, and mixed pixels along the boundary line must be removed from the calculations.

Figure 1.8 shows an example of noise removal and segmentation process from a current project at Digital Ag Lab, UC Davis. The image is related to an almond orchard where each tree is marked by a unique ID and includes its coordinates. Canopy boundaries and cavities within the canopy are excluded, and the remaining pixels can be considered to extract the spectral signature of each canopy.

#### 1.5.2.2 Raw Feature Extraction

When an efficient mask is created, it can segment all the stacked data (layers from different bands or sensors). As a side note, before applying the mask to the layers of data, it is preferable to resample all layers to the finest pixel size to match each other. What remains after segmentation would be numerous pixels from one or multiple bands based on the available sensors. For example, thermal data have one

band only, while hyperspectral data can have hundreds of bands. Most of the published literature has used the pixels' average in each band as a representative of the crop/band. However, some researchers reported higher correlations when using quartiles (25% and 75%) instead of simple averaging, particularly in thermal data<sup>48</sup>. Anyway, when a whole canopy is reduced to a single number, especially when using machine learning and artificial intelligence techniques, a large part of valuable information is being discarded. As a result, a sub-canopy level<sup>7</sup> or even a pixel level<sup>162</sup> data augmentation might help capture the most information possible.

The features extracted from the segmented images are referred to as raw features that include but are not limited to the minimum, maximum, average, median, standard deviation, and other histogram features. These data represent the variations in a specific band in the region of interest. Sometimes the raw features exhibit a strong correlation with the response variable. But usually, the raw features alone cannot explain all the variability in response, raising the need for the engineered features that are explained in the feature engineering part.

### 1.5.3 Analytics

Analytics, the last processing step, can unveil trends and aspects that would otherwise be lost in the mass of information. This knowledge can be used for predictions and managerial practices. However, data analytics might result in misleading conclusions if not processed correctly. In the following, the most common problems and methods are discussed.

#### 1.5.3.1 *Multicollinearity*

Multicollinearity is a phenomenon in which two or more independent variables, used collectively to model a dependent variable, are highly correlated (they can be linearly predicted from each other)<sup>193</sup>. For example, if canopy height and volume are highly correlated, using them both for modeling yield will suffer from multicollinearity issues. Multicollinearity adversely affects the statistical significance of the independent variables in common regression analysis methods, such as least squares, causes drastic fluctuations in estimated coefficients, and weakens the statistical power<sup>194</sup>. When the number of independent variables is limited, understanding and handling multicollinearity is relatively simple and



sometimes negligible. However, increasing the number of input variables makes the multicollinearity issue rather tricky. For example, hyperspectral data contain hundreds of highly correlated bands that should be handled before modeling. Usually, this leads to feature selection and feature engineering techniques discussed in the next section.

#### *1.5.3.2 Feature engineering and feature selection*

Data gathered in a remote sensing process contains specific information called features, as mentioned in 1.5.2.2. However, most of the time, the raw features are not adequate or sometimes are redundant to be used in the modeling process. As a result, feature engineering and feature selection methods gained attention. Feature engineering (sometimes called feature extraction) is the technique of creating new (more meaningful) features from the original features<sup>195</sup>. For example, NDVI can be considered a feature engineering in agriculture since the reflectance values of the two bands are transformed to create a more tangible feature. Using any other transformation, such as data normalization and data standardization, that creates new features from the raw features is also feature extraction. One should note that an infinite number of transformations are possible for any given dataset, and as a result, unlimited features can be generated. However, too many features cannot be used for modeling, even with machine learning techniques, especially when the number of data points is not very large, which is the case in most agricultural applications by expensive samplings. In many instances, even the raw features are too many that cause a dimensionality problem: many variables corresponding to a few samples<sup>196</sup>. Therefore, a variable reduction is usually inevitable, either through projection methods, feature selection, or a combination of both.

Projection methods work on the feature engineering principle: they transform data from a higher dimension to a lower dimension, as in principal component analysis (PCA). In an effective transform, a few variables (sometimes called latent variables or components) would explain most of the variation in the response. Although these techniques are prevalent, they have a severe drawback: losing links to the original variables and hence foiling interpretability<sup>197</sup>.

On the other hand, feature selection is an approach in which a subset of the input features (either the raw or engineered features) is selected based on their significance and contribution to the model, and redundant or irrelevant features are removed<sup>197</sup>. In addition to the redundancy elimination, feature selection improves the models' interpretability and understanding of the relationship between the explanatory variables and the response<sup>196</sup>. Feature selection should typically improve performance or at least reduce dimensionality with minimal performance degradation. For example, in a yield prediction study, removing 40% of a total of 65 features led to a less than 3 % increase in the mean absolute error<sup>195</sup>. Although feature section techniques might not gain much attention when the explanatory variables are limited, in most remote sensing studies, especially in those involving various spectral bands such as hyperspectral data, feature selection is inevitable. For instance, a study showed that less than 0.45 percent of the features (6 out of 1339 bands) in a hyperspectral dataset are informative<sup>198</sup>. So, based on the input variables and the modeling problem, suitable feature engineering and feature selection approaches must be employed to ensure the correct data are used in the modeling process<sup>83</sup>.

#### *1.5.3.3 Data mining*

Sometimes the available data is huge, and there is no evident relationship between variables, and as a result, traditional modeling and data interpretation techniques fail. This can be due to the high dimensionality of the dataset, the missing productive factors in the model, or it can be due to noisy data and the presence of outliers. In this case, unsupervised clustering methods could be beneficial for finding hidden relations within data and also for determining outliers. Unsupervised methods, machine learning algorithms that analyze and cluster unlabeled datasets bypass the need for labels and have shown great potential in revealing unknown patterns in data. K-means, self-organization mapping (SOM)<sup>199</sup>, (PCA)<sup>200</sup>, and hierarchical clustering are among the frequently used unsupervised algorithms on remote sensing data. Although unsupervised algorithms might not perform as good as supervised methods<sup>201</sup>, their independence from labels makes them a reasonable choice for most problems, especially for clustering and noise removal. Moreover, a combination of supervised and unsupervised techniques might increase the models' performance<sup>202</sup>. These methods can be used in a row with modeling as well.

#### 1.5.3.4 *Regression\classification*

When linking explanatory and response variables, the outcome can be either classification or regression.

In classification problems, the output would be a prediction/classification of discrete values as in healthy and diseased groups. On the other hand, regression algorithms are used to predict the continuous values, such as the amount of yield in an orchard. However, linear regression, due to its simplicity and interpretability, has gained a lot of attention and is implemented in numerous studies. Table 1-5 includes explanatory variables, response variables, and modeling methods used in the selected papers. As shown in the table, more than 70 percent of the papers have used linear regression as a primary, or in some cases secondary, modeling method.

Analysis methods can be categorized into two general classes of linear and nonlinear algorithms. Among linear algorithms, simple (one input variable) and multiple (multiple input variables) linear regressions (MLR) are the most common methods utilized in numerous agricultural studies for predicting yield<sup>163</sup>, LAI<sup>203</sup>, stem water potential<sup>204</sup>, nitrogen status<sup>205</sup>, and many more. MLR has attracted lots of attention, especially since it can be combined with the feature selection step to select the most contributing factors and the best model at the same time. For a limited number of input variables, linear regressions are very reliable, and the relationship between the input variables and the response can be easily interpreted. However, in some remote sensing studies, especially recent publications that include several sensors, many variables are extracted to predict a response factor and the increasing number of explanatory variables makes the MLR model selection process more challenging. Moreover, many agricultural processes are better represented by nonlinear models than linear models<sup>206</sup>. As a result, alternatives to linear approaches, such as computational methods, emerged regardless of their complexity and lack (or difficulty) of interpretability.

Table 1-5-Analysis parameters of the selected papers

Crop	Explanatory variable (s)	Response variable(s)	Modeling method	Other methods used	Reference
Alm.	NDVI	SWP	Linear regression	-	7
Alm.	Temperature	Stomatal conductance	Linear regression	-	22
Alm.	Height, volume, bloom density	Yield	Tukey HSD test	Linear regression	23 / 24
Pista.	RGB image	Tree heights	T-test	Linear regression	25
Alm.	EBI <sup>1</sup>	Bloom coverage	Linear regression	SVM <sup>2</sup>	20
Alm.	Inter/intra-crown $\sigma T^3$	SWP	Linear regression	-	26
Alm.	Tc – Ta <sup>4</sup> / CWSI	SWP	Linear regression	2nd order polynomial regression	27
Pista.	CWSI/DLSI <sup>5</sup>	SWP	Non-Linear regression	Linear regression	28
Alm.	46+ VIs	Red leaf blotch (disease)	Multivariate Analyses	ANOVA, HSD Tukey, SVM, LDA <sup>6</sup>	29
Alm.	SIF <sup>7</sup> / CWSI	Stomatal conductance	ANOVA	Linear regression, Tukey HSD test	30
A/P	NDVI/ CWSI	SWP	Non-Linear regression	Linear regression	21
Alm.	Tc – Ta /CWSI	VPD <sup>8</sup>	Linear regression	-	31
A/P	Four water sensitive spectral indices <sup>9</sup>	CWC <sup>10</sup>	Continuous wavelet analysis	Linear regression, Multiple linear regression	32
Alm.	15 input variables <sup>11</sup>	Yield	Stochastic Gradient Boosting (ML <sup>12</sup> )		33
Alm.	UAVSAR L-band	Land Cover type	Jeffries-Matusita distance	Classification	34
A/W/P	Spectral & Thermal bands	LST <sup>13</sup>	ANOVA	post-hoc Tukey's tests	35
Pista.	METRIC <sup>14</sup>	ET	Linear regression	Stepwise linear regression	36
Alm.	METRIC	ET	Linear regression	-	37
Pista.	DEM <sup>15</sup> , NDVI	Tree Elevation	Classification	-	38

1- Enhanced Bloom Index

2- Support Vector Machine- Classification

3- The standard deviation of temperature

4- Differential between canopy and air temperature

5- Days Since Last Irrigation

6- Linear Discriminant Analysis

7- Solar-induced fluorescence

8- Vapor Pressure Deficit

9- The Water Index (WI), NDWI, The Normalized Difference Infrared Index (NDII)

10- Canopy Water Content

11- Historic yield, orchard age, temperature, NDVI, etc.

12- Machine Learning

13- land surface temperature

14- Mapping Evapotranspiration at high Resolution with Internalized Calibration (Inputs: NDVI, LST, Albedo, LAI)

15- Digital Elevation Mode

Computational intelligence (artificial intelligence) and expert systems, such as Artificial Neural Networks (ANN) or more advanced machine learning methods, which are considered a subdivision of nonlinear algorithms, have gained increasing attention due to several reasons: their ability to handle quantitative and qualitative data simultaneously, their capacity to weight variables based on their importance, their potential to manage both linear and nonlinear responses and the growing computational power of new computers<sup>199</sup>. Since these methods use their internal transformations (through weights and activation functions), an optimal combination of the features (engineered features) will be formed inside the

algorithms, making these techniques a powerful modeling tool in many fields. Methods such as ANN<sup>207</sup>, Regression (decision) Trees (RT) <sup>208</sup>, Partial Least Squares Regression (PLSR) <sup>209</sup>, and Random Forest (RF)<sup>210</sup> are widely utilized in agricultural fields. However, regardless of their outstanding success in different areas, artificial intelligence methods need a relatively large number of samples (labels) that dwarfs their advantage in most remote sensing applications. As a result, finding a technique that combines artificial intelligence with other statistical methods to preserve AI methods' advantages while minimizing their need for large amounts of samples is of broad and current interest. An ambitious model should take all the determining factors into account, weigh them based on their importance level, and use all available information so that the combination of inputs can represent a more accurate prediction. To reach such a model, a data fusion framework is needed to combine data from various layers of information to fill the knowledge gap.

## 1.6 Conclusions

As Throughout this chapter, the necessity, collection methods, and processing pipelines of remote sensing data using available platforms and sensors for various applications with a focus on nut orchards were discussed. Due to the rapidly growing acreage of nut orchards, and the increasing need for food in general, new agricultural methods based on remote sensing data are inevitable. The available remote sensing platforms can be classified into satellites, manned aircraft, and UAS, each with pros and cons, making platform selection a subject-dependent task. Sensors are also mostly problem-dependent, and the requirements of the issue determine the best possible sensor. However, in many cases, a combination of sensors and platforms is combined for the best results. Remote sensing applications are diverse, including irrigation management, disease control, yield estimation, nutrition mapping, salinity control or detection, phenotyping, and other managerial applications. However, reviewing the published papers on nut crops showed that most of the papers focused on water management problems and other applications are limited or not practiced, indicating research opportunities and the gap in the knowledge.

Before analyzing data, some preprocessing steps should be taken to ensure refinement and remove unsupportive/redundant data. Radiometric correction is an essential preprocessing step that has not been

taken seriously in most studies, although it is crucial, especially for long-term temporal comparisons. Additionally, since remote sensing data rely on electromagnetic reflectance, preserving the original reflectance values (pure pixel) is of great concern, and employing software that manipulates the original reflectance values are not recommended. Before feature extraction, noise and outlier detection and removal, which can be achieved using supervised and unsupervised methods, guarantee the accuracy and repeatability of the results. In many cases, the raw features cannot explain all the variability in response, raising the need for feature engineering and feature selection. Features can be used in linear or non-linear models. Although linear models, such as linear regression, are potent and most practiced approaches in modeling, nonlinear methods such as machine learning and artificial intelligence techniques, which tackle many input variables and capture the most relevant information from the input features, are expected to increase. A favorable analytics model or a data fusion framework would determine all essential factors, weight them based on their importance level, and use all available information for the best prediction possible.

## 2 Impact of Sun-View Geometry on Canopy Spectral Reflectance Variability

### 2.1 Introduction

The application of lightweight multi- and hyperspectral camera technologies aboard drones, also known as Uncrewed Aerial Systems (UASs), is increasing rapidly for various remote sensing purposes. These applications include phenotyping <sup>211</sup>, stress detection <sup>212</sup>, nutrition status mapping <sup>213</sup>, yield prediction <sup>214</sup>, precision agriculture <sup>215</sup>, forest monitoring <sup>216</sup>, and many more. In all mentioned applications, analyses are based on the objects' precise geometric and reflectance characteristics. In this regard, a robust image rectification methodology is required to ensure data quality that leads to consistent outputs regardless of measurement conditions. A widespread issue in UAS-based remote sensing is the model bias to the specific time and space of the dataset used for model training and consequently, the results are barely generalizable and repeatable. In most studies, advanced machine learning techniques were used and led to high modeling scores and  $R^2$  values. However, the resulting models often cannot handle new data sets. This inconsistency roots in the variation sources that alter the measured reflectance factor of the plants.

Reflectance factor (the ratio of radiance of a surface to radiance of an ideal-lossless- and diffuse - Lambertian- standard surface reflected in the same wavelength, into the same direction, and measured under the same illumination conditions <sup>217</sup>), which is independent of environmental factors and measurement devices, is the foundation of quantitative remote sensing <sup>218</sup>. Based on the definition, the reflectance factor is a function of several factors, and errors in measuring any of the factors would accumulate to an enormous uncertainty in the outputs. Radiance, irradiance, and geometry (the sun-camera view angles) are the primary factors affecting reflectance calculations. However, each factor could be touched with some noise discussed in the following.

Radiance is the first factor to measure, and it is recorded by the cameras. However, cameras' output is in the form of digital numbers (DN) that is a function of various factors, including the objects' spectral response. DN is affected by sensor characteristics <sup>219</sup>, stray lights <sup>220</sup>, illumination variation, light source-sensor geometry <sup>221</sup>, as well as other environmental factors such as atmospheric effects. As a result, cameras' radiometric correction, compensating for external effects and converting DNs into either surface

spectral radiance ( $W \cdot sr^{-1} \cdot m^{-2} \cdot nm$ ) or reflectance, is crucial (by reflectance, in this text, we mean reflectance factor,  $R$ , that should not be confused with reflectance,  $\rho$ <sup>217</sup>). Radiometric calibrations, nowadays, are well practiced in aerial remote sensing and results suffer the least from its noises.

Irradiance is the second factor. Regardless of the platform and sensor in use, reflectance calculation requires an accurate estimation or measurement of irradiance at the object's surface ( $E_{at}$ )<sup>222</sup>. Currently, there are four methods to determine irradiance: 1- Direct measurement using an irradiance sensor on top of the UAS, 2- Direct measurement using a static device near the study field, 3- Simulation of irradiance using atmospheric radiative transfer models based on accurate knowledge of the atmosphere condition at the flight time and location, and 4- Estimation of irradiance using targets with known reflectance factors. In practice, each method is based on assumptions that might not hold for all situations. When using a UAS-based irradiance sensor, it is assumed that the atmospheric effect in the distance between the UAS and the target is negligible (i.e., the atmospheric transmittance is considered equal to one and the object's radiance reaches the sensor intact). For low flight altitudes (below 150m), the atmospheric effect is reported to be between 1.5 % - 6% of the measured reflectance and differs based on wavelength<sup>218,223</sup> and air quality parameters such as humidity<sup>224</sup>. In the second method, the assumption is that irradiance recorded by the static sensor is the same at all locations in the field (i.e., homogeneous irradiance in the whole experiment area), and the radiance of the targets passes through the air reaching the camera with negligible atmospheric effect<sup>225</sup>. The third method, which is not very accurate, is usually used for specific purposes such as fluorescence studies<sup>226</sup>. The fourth method, standard reflectance panels, is the most practiced and low-cost technique since it does not need absolute values of radiance and irradiance. This method determines the reflectance factor by ratioing the target and the reference panel, assuming the same irradiance and imaging conditions<sup>222</sup>. Some studies have combined two approaches, usually the fourth method with one of the other methods, to improve the shortcomings of a single method<sup>227</sup>. Irradiance measurements still pose serious detrimental effects on accurate reflectance conversions.

Sun-sensor geometry (the last primary factor) is mostly neglected in agricultural remote sensing applications since it is frequently assumed that view, and illumination directions do not significantly



affect the reflectance in the camera's field of view (FOV). This assumption is misleading, especially in clear sky conditions <sup>228</sup>, when the high ratio of the directional to diffuse components in the solar irradiance (which can be as high as 94 percent of total irradiance <sup>229</sup>) seriously affects the radiance measured from different angles, also known as the directional effect. For instance, Royer et al. reported a significant difference (mean relative variation of 60%) in the radiance of several natural land covers measured with a 72°-FOV multispectral camera. They reported that maximum variation, which was asymmetric close to the nadir view, happened when the scan direction of the line scanner sensor was parallel to the principal solar plane, indicating strong effects of directional radiations <sup>230</sup>. Similarly, Aleksandra et al. reported up to 60% systematic mean difference in DN values along the principal plane in images captured with a Sony NEX-5T camera (FOV 110°) at 75 m altitude <sup>231</sup>. In these examples, flight campaigns were short enough (~ 5 minutes) so the solar zenith and azimuth angles were assumed to be fixed. For longer flights, where the change in solar angles is not negligible, or when data were collected in different dates (with different solar irradiation conditions), reflectance values also depend on sun direction changes during the flight. Even in constant solar angles, the variations in radiance due to the directional effects recorded by wide-angle cameras (the typical type of sensor for all UAS-based remote sensing devices) are not negligible <sup>232</sup>. Near the hotspot (a bright region in the area where the view and sun angles are the same), a minor view angle variation of 2.5° can cause more than 35% difference in reflectance <sup>233</sup>.

Physical-Based Models (PBM) and Radiative Transfer Models (RTMs) such as ProSail are helpful tools to analyze the effects of different factors on reflectance and compare them with acquired data. RTMs and PBMs aim to use our understanding of physics to better interpret remote sensing data or even simulate the scenarios based on physics laws. RTMs often focus more on the medium through which electromagnetic radiation passes (like within the canopy), while Physical-Based Models focus more on the target and its physical characteristics and biophysical characteristics of the plants, such as chlorophyll, water, dry matter contents, and canopy architecture (primarily leaf area index, leaf inclination distribution, and relative leaf size) <sup>234</sup> besides irradiance and geometry to estimate reflectance. RTM or PBM calculate the

Bidirectional Reflectance Factor (BRF) and its distribution over the hemisphere, forming the bidirectional reflectance distribution function (BRDF), a pivotal factor in remote sensing nomenclature <sup>235</sup>. Using BRDF, the reflectance in a specific direction can be estimated. Estimation of reflectance in different condition is a valuable resource that can be used to evaluate the accuracy of the sensors and adjusting for the inconsistencies. Furthermore, these models are powerful tools to do a reverse analysis and estimate the constituents of the leaves or canopies using reflectance data. For example, nitrogen concentration, or water content can be potentially estimated from reflectance data. However, these models are still in their nascent stage and due to computationally expensive algorithms, more effort is needed to be able to generate realistic BRDF for most crops and fields.

The BRDF also depends on the wavelength, similar to the illumination and sun-view geometry. As a result, the anisotropic effects can easily propagate to normalized indices such as NDVI and NDRE, although to a lesser extent. For instance, <sup>236</sup> showed that the sun-angle variations introduced 7% - 10% uncertainty in estimating NDVI from geostationary satellite images. Goniometer measurements revealed the same pattern for winter wheat; NDVI and NDRE changed about 12% in the  $\pm 60^\circ$  view angle range, while the difference for individual bands in visible and NIR regions was more than 260% and 90%, respectively <sup>237</sup>. It is worth mentioning that the directional radiations (anisotropy) conversely affect NDVI and NDRE compared to individual bands. In other words, single bands' reflectance values increase on the principal plane toward the hotspot while NDVI and NDRE decrease <sup>232,237</sup>.

Anisotropic characteristics of an object determine the extent of variation in reflectance due to directional reflectance. For a sample with known anisotropic properties, radiance at each view angle can be converted to a specific direction (e.g., nadir view angle), enabling quantitative comparison for a given solar angle. However, determining accurate anisotropic properties of plants and vegetation (combination of leaves, branches, and physical form in a specific setting and environment) is expensive, laborious, and impractical due to their ever-changing nature, as well as due to the presence of other objects/materials/plants along with the target plants <sup>238,239</sup>. Additionally, forward and backscattering

regions exhibit different reflectance. For example, Hasegava et al. reported higher reflectance in the backscattering region than the forward scattering region, attributing this variation to the ratio of shade in each region (less shade more reflectance- the same concept as a hotspot, which is a specific case in backscattering) <sup>240</sup>. These variations in the reflectance and magnitude of the hotspot produce a pattern, referred to as the "angular signature," that may provide information about canopy structures and help feature identification <sup>241</sup>. The canopy clumping index, as an example, has been derived from hotspot data to quantify the leaf distributions in canopies <sup>242–244</sup>.

The main focus of this chapter is to investigate the canopy reflectance variability associated with the solar and view angles due to the anisotropic properties of surfaces in UAS-based remote sensing and to compare the 4Sail RTM <sup>245,246</sup> simulations with UAS-based data. Specifically, we are looking for methods to eliminate or reduce the dependency of reflectance analysis on directional effects. The primary hypothesis of this study is that the effects of solar and view angle lead to a significant difference in the reflectance of objects in cameras' FOV. Additionally, we assume that the angular signature of different surfaces can be retrieved from wide-FOV cameras. Hence, this chapter describes methods and results of real-world experiments to measure and quantify directional effects in solar radiation on reflectance, compare them with the well-established 4Sail model, and account for them in UAS-based remote sensing analysis. In turn, accounting for these effects will significantly improve the reliability, generalizability, and repeatability of the outputs. Accordingly, this study will first represent the methods and materials as well as the experimental setups. The results of the experiments will be presented, followed by a comprehensive discussion.

## 2.2 Materials and methods

This section is divided into three subsections: Formulation, Experimental fields, and Data collection and processing.

### 2.2.1 Formulation

Reflectance factor at the surface of an object is defined as <sup>247</sup>:

$$R_s = \frac{L_s(\theta_i, \phi_i; \theta_r, \phi_r; \lambda)}{L_{id}(\theta_i, \phi_i; \lambda)} \quad (\text{Eq. 2.1})$$

where  $L_s$  and  $L_{id}$  are the reflected radiances from the object's surface and an ideal (lossless) and diffuse (Lambertian) surface, under identical illumination and view geometry.  $\theta$  and  $\phi$  are zenith and azimuth angles incident and reflected (shown by subscript  $i$  and  $r$ ) rays with a wavelength of  $\lambda$ , respectively. In practice, near-Lambertian panels exist, but they are not lossless. As a result, the reflectivity of the panel should be taken into account, which yields <sup>228</sup>:

$$R_s = \frac{L_s(\theta_i, \phi_i; \theta_r, \phi_r; \lambda)}{L_{id}(\theta_i, \phi_i; \lambda)} R_{ref} \quad (\text{Eq. 2.2})$$

Assuming directional view and illumination, equation 1 results in BRDF <sup>247</sup>:

$$BRDF = f(\theta_i, \phi_i; \theta_r, \phi_r; \lambda) = \frac{dL_r(\theta_i, \phi_i; \theta_r, \phi_r; \lambda)}{dE_i(\theta_i, \phi_i; \theta_r, \phi_r; \lambda)} [sr^{-1}] \quad (\text{Eq. 2.3})$$

Where  $E$  is directional irradiance at the surface ( $dA$ ) and  $L_r$  is radiance at  $\theta_r, \phi_r$ . By definition, directional rays are in an infinitesimally small solid angle, so they cannot be measured directly. However, they can be used as a starting point to calculate quantities such as BRF, biconical reflectance factor, or hemispherical-directional reflectance factor (HDRF). For an ideal diffuse panel, we have:

$$BRF = \pi \cdot BRDF = \pi \cdot f(\theta_i, \phi_i; \theta_r, \phi_r; \lambda) \quad (\text{Eq. 2.4})$$

As mentioned in the introduction, solar radiation consists of direct radiant flux and diffuse components that make a mixture of directional and hemispherical illumination conditions. By dividing irradiance at each point ( $L_i$ ) into a direct ( $E_{dir}$  with angles  $\theta_0, \phi_0$ ) and an isotropic (i.e., independent of the angles) diffuse part ( $L_i^{dif}$ ), HDRF can be defined as:

$$HDRF = \frac{L_s(\theta_i, \phi_i; 2\pi; \theta_r, \phi_r; \lambda)}{L_{id}(\theta_i, \phi_i; 2\pi; \lambda)} = R(\theta_0, \phi_0; \theta_r, \phi_r; \lambda)d + R(2\pi; \theta_r, \phi_r; \lambda)(1 - d) \quad (\text{Eq. 2.5})$$

where  $d$  corresponds to the fractional amount of direct radiant flux which can be measured or estimated <sup>248</sup>.

$$d = \frac{(1/\pi) E_{dir}(\theta_0, \phi_0; \lambda)}{(1/\pi) E_{dir}(\theta_0, \phi_0; \lambda) + L_i^{dif}} \quad (\text{Eq. 2.6})$$

In reality, solar radiation and what can be measured with sensors are conical rather than directional. However, we assume directional view and radiation due to the relatively small solid angles, which is a

fair assumption <sup>249</sup>. Figure 2.1 shows the diagram of directional and diffuse light components reaching a point and its reflectance at a specific angle with variables used in this chapter.

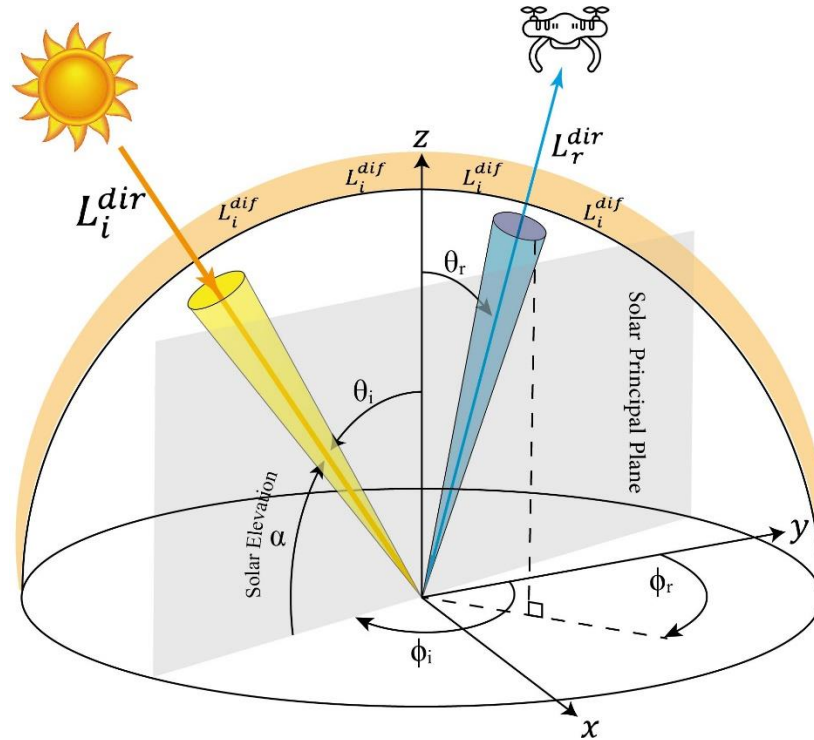


Figure 2.1- Diagram of solar light components, directional and diffuse, radiating on a surface and its directional (conical) reflection.

### 2.2.2 Experimental fields and data collection

This study primarily started with aerial data from a commercial citrus field, and then two other crops, almond, and vine, were added to test the consistency of the results and the impacts of crop type. The citrus data included 2-year-long monitoring of a 2-ha commercial citrus orchard (Figure 2.2) at Strathmore, CA. The almond data was collected from a research orchard located at Kearney Agricultural Research and Extension Center (Parlier, CA), and grape data was collected from a part of a commercial vineyard in Shafter Valley, CA. Data collection and site information are presented in Table 2.2.

In this study, two multispectral cameras commonly used in agricultural remote sensing were deployed to perform the experiments: Micasense RedEdge 3 (MRE) mounted on a DJI Matrice 210 and DJI Phantom 4 multispectral (P4M). Specifications of these cameras are listed in Table 2.1<sup>250,251</sup>.

Table 2-1- Specifications of the cameras used in this study.

Item	Micasense RedEdge 3	DJI Phantom 4 multispectral	
Focal length	5.4 mm	5.74 mm	
Imager size (horizontal × vertical)	4.8 × 3.6 mm	4.96 × 3.72 mm	
FOV (H × V)	47.9 × 36.9 °	50.6 × 42 °	
FOV (Diagonal)	58.1 °	62.7 °	
Pixels (W × H)	1280×960	1600×1300	
Camera on Gimbal	No	Yes	
DLS on Gimbal	No	No	
Filters (Center wavelength ± FWHM)	Blue	475 nm ± 10 nm	450 nm ± 16 nm
	Green	560 nm ± 10 nm	560 nm ± 16 nm
	Red	668 nm ± 5 nm	650 nm ± 16 nm
	RedEdge	717 nm ± 5 nm	730 nm ± 16 nm
	NIR	840 nm ± 20 nm	840 nm ± 26 nm

Both cameras are equipped with a downwelling light sensor (DLS) which measures the incident light, providing irradiance data. However, the lack of a reliable cosine corrector or a gimbal for DLS sensors makes their readings extremely tilt-dependent. In other words, even in a stable sky condition, the DLS sensor records varying data due to the UAS movements: high values when the angle between the DLS and solar ray is decreased and vice versa (see Figure A.4 in the Appendix). As a result, the flight mission paths were adjusted to be perpendicular to the solar direction, minimizing the DLS readings' dependence on the UAS's pitch angles (yaw has no effect, and roll variations are negligible in direct routes) - see Figure A.2 and Figure A.3 in the Appendix for clarification. For additional information about the flights, refer to Table 2.2.



Figure 2.2- The citrus block of the experiments.

Flights were conducted between 20 to 60 m Above Ground Level (AGL), producing a Ground Sampling Distance (GSD) of about 1- 4 cm. The images were collected with 80% front overlap and 75-80 % side overlap, all taken at nadir view (roll  $\approx$  pitch  $\approx$  0), around solar noon. Standard reflectance reference images (panel from Micasense and a fabric tarp -Group 8 Technology, Inc, USA) were also captured from different altitudes before and after each flight with the panels placed in the center of the images ( $\theta_r = 0$ ). Table 2.2 summarizes data collection dates, local times, weather conditions, and flight parameters from the experiment sites.

Table 2-2- summary of data collection from the crop sites.

Date (yy/mm/dd)	Sky condition	Flight Start Time/ Elevation $\alpha$	Flight End Time/ Elevation $\alpha$	Solar Noon Time/Elevation $\alpha$	Alt. (m)	Cam. Type
<b>Citrus / 119.0242689°W 36.1714388°N / 960 trees</b>						
19/03/18	Sunny	14:19/49.1	14:36/47.3	13:04/53	60	MRE
19/06/12	Sunny	14:02/70.7	14:13/68.9	12:56/77	60	MRE
19/09/05	Sunny/ Cloudy	12:31/60	12:43/60.4	12:54/61	60	MRE
19/12/03	Sunny	13:47/25	13:58/23.9	11:46/32	60	MRE
19/12/17	Sunny	12:33/29.7	12:43/29.3	11:52/30	60	MRE
20/06/17	Sunny	13:26/75.8	13:37/74.6	12:57/77	60	P4M
20/09/29	Sunny	12:55/51	13:08/50.7	12:46/54	60	P4M
20/11/20	Partly Cloudy	12:49/31.7	13:02/30.8	11:42/34	60	P4M
20/12/16	Sunny	12:41/29.4	12:50/28.9	11:52/30	60	P4M
<b>Almond / 119.5132331°W 36.5982516°N / 1.5 ha / 450 trees</b>						
19/05/29	Sunny	10:07/51	10:22/54	12:54/76.2	45	MRE
19/07/26	Cloudy	12:03/69	12:17/70.9	13:03/73.9	45	MRE
20/06/02	Partly Cloudy	11:38/68.7	11:54/71.3	12:55/76.8	45	P4M
20/07/08	Sunny	12:00/71.1	12:15/73.3	13:02/76.9	45	P4M
<b>Grape / 119.2818661°W 35.4403658°N / 0.3 ha / 204 vines</b>						
21/06/23	Sunny	13:40/ 75	14:01/72	12:59/77.9	20	P4M
21/08/17	Sunny	12:34/ 66.9	12:59/ 67.7	13:01/67.7	20	P4M

### 2.2.3 Processing

Radiometric calibration steps were followed closely to produce reflectance images for each data set. The procedure for converting DN values to radiance and lens corrections for the MRE and P4M can be found at <sup>252</sup> and <sup>253</sup>, respectively. In summary, DNs were first normalized for both cameras based on the sensor's bit-depth, followed by dark current and vignetting corrections, then normalized by gain and exposure

time, and finally, lens distortion correction (and row gradient correction for MRE). On sunny days, where no drastic illumination change occurred during the flights, instantaneous irradiance was interpolated from the before and after-flight irradiances based on reference panels. For partially cloudy days, however, DLS data were used in addition to the panels to estimate the irradiance changes and compensate for it.

Then the radiometrically calibrated images were georeferenced individually (more than 4000 5-band images). A point showing the canopy center (tree crown center) and a rectangle containing the whole crown were created for each tree, and a unique number was assigned to it, as shown in Figure 2.2. Due to the high front and side overlaps, each tree appears in 15-20 images at different locations of the frame, i.e., different view angles ( $\theta_r, \phi_r$ ) as shown in Figure 2.3.

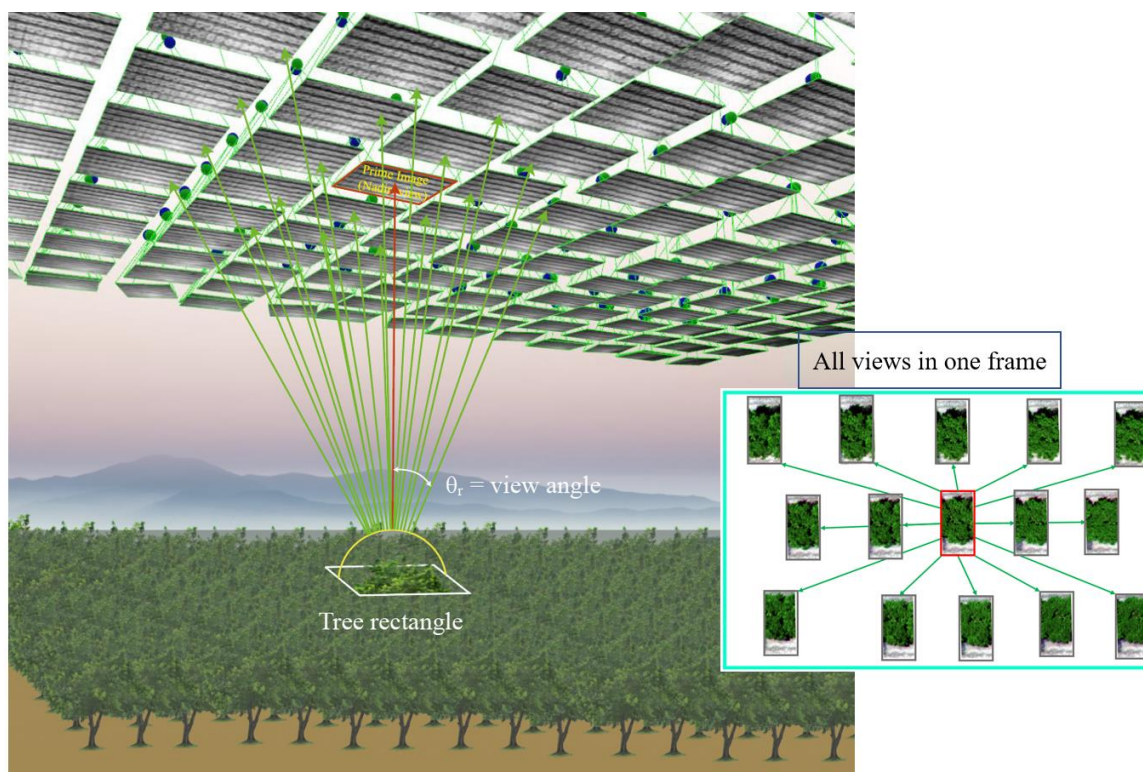


Figure 2.3- Different view angles of the same tree due to the overlapping images.

The canopy BRDF can be estimated by comparing reflectance in different directions. For each tree, the image in which the tree center is closest to the image center was selected as the prime image (or nearest to the nadir view,  $\theta_r \approx 0$ ). Since the number of images is usually less than the number of trees, the prime



view for several trees would be selected from one image. Meanwhile, the view angles ( $\theta_r, \phi_r$ ) for each tree were calculated based on their distance from the center of the image. The camera on the P4M is mounted on a gimbal that ensures the camera's roll and pitch angles remain zero regardless of UAS movements. In MRE, however, the UAS' movements affect the camera's roll and pitch angles, which need to be compensated in view angle analysis. In practice, calculating the camera's roll and pitch for each image is challenging unless a reliable inertial measurement unit (IMU) records the movement data. Moreover, based on the field location and image capture time, solar angles ( $\theta_i, \phi_i$ ) were also extracted for each image. Then for each tree, the prime view and all other views were segmented from all images that included the target tree. As mentioned earlier, this resulted in 15-20 off-nadir views for each tree in addition to the prime view. An approach similar to the one presented in <sup>254</sup> using Otsu's multi-threshold method <sup>255</sup> on the excessive green index (EGI) and NDVI was used to segment the canopy from the background and eliminate the shadowy and mixed pixels.

Reflectance data for each band were analyzed separately. Statistical analyses were conducted to find: 1) reflectance variation magnitude due to the changes in view angle; 2) the possibility of determining a minimum range for  $\theta_r$  and  $\phi_r$  around nadir in which the reflectance variation is negligible; 3) a general model to describe the effect of solar directional radiations, and 4) the feasibility of predicting the nadir reflectance ( $\theta_r = 0$ ) from any other  $\theta_r$  and  $\phi_r$ .

#### 2.2.4 Modeling

To ease the calculations, the x and y-axis (Figure 2.4) was rotated ( $\pi - \phi_i$ ) degrees and transferred the origin to the hotspot location. As a result, the new y-axis,  $y_{sp}$ , matches the solar plane and the new x-axis,  $x_{sp}$ , is perpendicular to it, as shown in Figure 2.4. In this way, the reflectance variations due to view angles in the solar plane and perpendicular to it can be treated separately. Additionally, this rotation makes results compatible to RTM outputs since they also make similar rotation and  $\phi_i = 0$  would show the sun's azimuth. Then the view angles were calculated based on each tree's distance from the hotspot and used to model the changes. Based on the literature, <sup>243</sup>, <sup>256</sup>, and <sup>257</sup>, the relationship between  $\theta_r$  and reflectance fits an exponential function featuring a sharp increase to reach a climax at hotspot followed by

a sharp decrease. Even though the relationship might not be symmetrical around the hotspot, an exponential function in the form of the Laplace distribution stood out after several attempts. For  $x_{sp}$ , the variations were not as sharp however a similar pattern was present. As a result, Equation 7 was used for modeling. Then for each band, five to ten percent of trees that presented highly comparable reflectance were selected to train the model and the rest of the trees were used for testing.

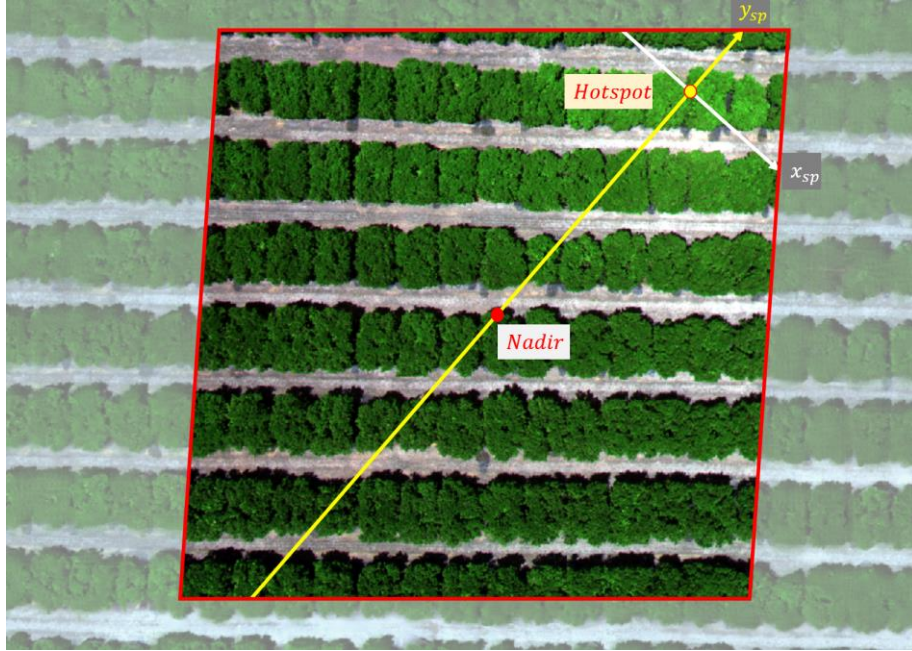


Figure 2.4- Defining new coordinates based on the hotspot. Note the change of reflectance along each axis.

$$z = a1 + a2 \left( \frac{\sigma_y}{2} e^{-\left| \frac{y}{\sigma_y} \right|} \right) \left( \frac{\sigma_x}{2} e^{-\left| \frac{x}{\sigma_x} \right|} \right) \quad (\text{Eq. 2.7})$$

This equation combines two Laplace distribution functions in  $x_{sp}$  and  $y_{sp}$  directions with four coefficients:  $a1$ ,  $a2$ ,  $\sigma_y$ , and  $\sigma_x$ . The  $a1$  and  $a2$  coefficients shift the surface to fit the variations better while  $\sigma_y$  and  $\sigma_x$  (Scale parameters) determine the magnitude of the hotspot in each direction.

To compare the measured data with a well established RTM, the field was simulated with the 4Sail model. The 4Sail models canopies as a layer of turbid-medium, assuming an infinite horizontal and homogeneous layer for canopies, infinitesimally small and bi-Lambertian leaves that their azimuth angles are randomly distributed while their zenith angles are defined by a function (Leaf Inclination Distribution Function-LIDF), and Lambertian soil <sup>258</sup>. To be able to compare aerial data with the 4Sail model, pairs of view

angles  $(\theta_r, \phi_r)$  were generated with one-degree interval within the cameras' FOV and used for simulation. The rest of the required parameters for 4Sail are presented in Table 3. For Leaf reflectance and transmittance, several leaves were randomly collected, and their reflectance and transmittance were measured with a HR-1024i SVC spectrometer (Spectra Vista Corp, Poughkeepsie, NY, USA) and an integrating sphere.

Table 2-3- Parameters used in 4SAIL models.

	q*	Leaf Reflect.	Leaf Transmit.	LIDF (a,b)	LAI	Zenith angle ( $\theta_i$ )	Azimuth angle ( $\phi_i$ )	Sun-Sensor Azimuth ( $\phi_i - \phi_r$ )	Soil Reflect.
In general	Estimated	Measured	Measured	Estimated	Estimated	Measured	Measured	Measured	Default dry soil library
For the presented results	0.08	Measured	Measured	(-0.35, -0.15) Spherical	0.08	20°	235° (From north)	Variable for each view	Default dry soil library

\* Hotspot factor- leaf length/canopy height

## 2.3 Results

The effect of directional radiance was found to be significantly influential on all bands and in all solar and view angle settings. Table A.1 in the Appendix contains results from all experiments outlined in Table 2.2. To clarify the results, one dataset (the 2019/06/12 citrus dataset, tabulated in Table 2-4) is discussed in detail.

Table 2-4- The results of directional effects and modeling on the citrus dataset collected on 2019/06/12 in a sunny condition and close to solar noon ( $\theta_i \sim 21^\circ$ ) with a hotspot inside the camera's FOV. The explanation of the table parameters are as follows:

Blue, Green, Red, RedEdge, and NIR, bands are shown as B, G, R, RE, and NIR, respectively. The Prime's mean and STD columns show the average reflectance of the prime views of all trees in the dataset (960 for citrus) and their Standard Deviation as an indication of reflectance variation. The "Mean of min" and "Mean of max" columns indicate the average of minimum and maximum reflectance for all trees. In other words, from 15-20 different view angles of each tree, the minimum and maximum reflectance were selected then averaged for all trees. Then percent of change and Average RMSD (Root Mean Square Deviation) is calculated based on the reflectance deviation of all trees from their prime views- refer to Equation 8 in Appendix.

	Band	Primes' mean	Primes' STD	Mean of min (all views)	Mean of max (all views)	Percent of deviation from the Primes (total)	A- RMSD	Model coefficients [ $a_1, a_2, \sigma_y, \sigma_x$ ]	RMS of prime errors	Average fit $r^2$
19/06/12	B	2.9	0.24	2.17	3.92	-24 to 37 (61)	0.53	[0.0151, 0.646e-6, 59.2, 29.2]	0.16	0.83
	G	11.4	0.93	8.97	15.31	-22 to 33 (55)	1.93	[0.052, 1.46e-6, 80.2, 38.4]	0.57	0.84
	R	3.9	0.34	3.1	5.5	-22 to 39 (61)	0.72	[0.0263, 1.36e-6, 45.9, 22.3]	0.2	0.82
	RE	25	1.48	20.1	32.5	-20 to 29 (49)	3.71	[0.115, 2.23e-6, 97.2, 42.3]	1.09	0.87
	NIR	46.8	2.6	40.8	56.4	-12 to 21 (33)	4.58	[0.36, 4.29e-6, 79.5, 27.8]	1.27	0.85

Figure 2.5 a-f shows the variations in reflectance of tree canopies in different bands as well as in NDVI in  $y_{sp}$ . According to Table 2-4, the total reflectance variation is 61%, 55%, 61%, 49%, and 33% of the mean of the prime views at each band, blue, green, red, red edge, and NIR, respectively (see Figure A.1 in Appendix for percent of reflectance variations graph at each band). This variation is caused by the directional solar radiations, resulting in RMSDs (reflectance deviation from the prime view) twice as

large as Primes' STDs. For example, the STD of reflectance in the blue band for the prime views is 0.24%, while RMSD is 0.53% for all views. Statistical analysis confirmed that changing the view angle as small as 2 degrees can cause a significant difference in the reflectance of canopies. The variation in the prime views (Primes' STDs) emerges from the differences in tree canopies (the desired variation, which is the primary purpose of environmental remote sensing), directional solar radiation effects (in 10 degrees- see Figure 2.5), and unaccounted irradiance changes. Suppose the whole variation in the prime views is considered the desired variation (intrinsic variation of trees), and the directional solar radiation is the only error source. In that case, variations due to the error source are twice larger than the dynamic range of the desired variations. Consequently, drawing conclusions based on this data is risky without subtracting the error variations. The same pattern exists for all other bands. Interestingly, for cloudy datasets (ex. 19/09/05 cloudy), the Primes' STDs and A-RMSD are almost equal, confirming that the directional solar radiation is the source of substantial undesirable variations and in cloudy conditions this error source does not exist (under these conditions diffuse radiation from the sky is closer to isotropic).

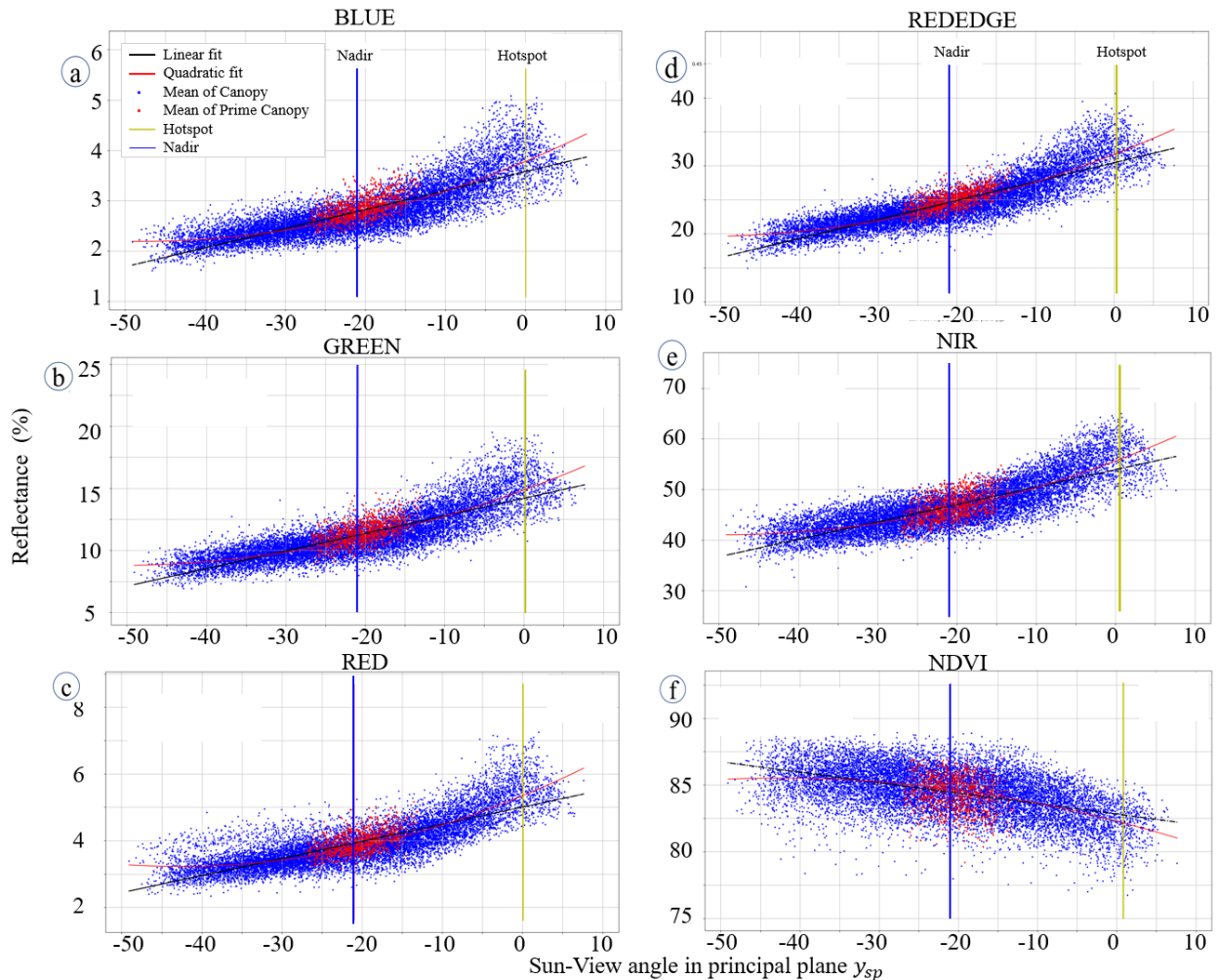


Figure 2.5- The effect of directional solar radiation on the reflectance of Blue, Green, Red, RedEdge, NIR bands as well as NDVI shown in a-f, respectively. Each point represents canopy mean reflectance from a particular sun-view setting. Clearly, view angle significantly affect the measured reflectance (as well as NDVI) under direct solar flux.

### 2.3.1 Variation modeling

We obtained quite promising results for modeling the variations. Average  $r^2$  in Table 2-4 shows how well the model fits the reflectance of trees from different view angles on average. In other words, given the reflectance of a tree in a particular angle, the model could predict reflectance in any other view angles with  $r^2$  stated in the table. In most datasets, including the Table 2-4 dataset, the residuals of the model in both  $x_{sp}$  and  $y_{sp}$  directions were normally distributed, indicating robust model performance. However, error distribution was skewed toward the hotspot for some datasets, i.e., higher residuals near the hotspot, showing a potential for further improvements. Figure 2.6 shows data distribution in  $y_{sp}$  (Figure 2.6 b), in  $x_{sp}$  (Figure 2.6 c), and the 3D representation of the points and the model (Figure 2.6 a) the interactive 3D

plot is accessible at: <https://chart-studio.plotly.com/~hamid39/1> . For more graphical data, refer to the Appendix and metadata.

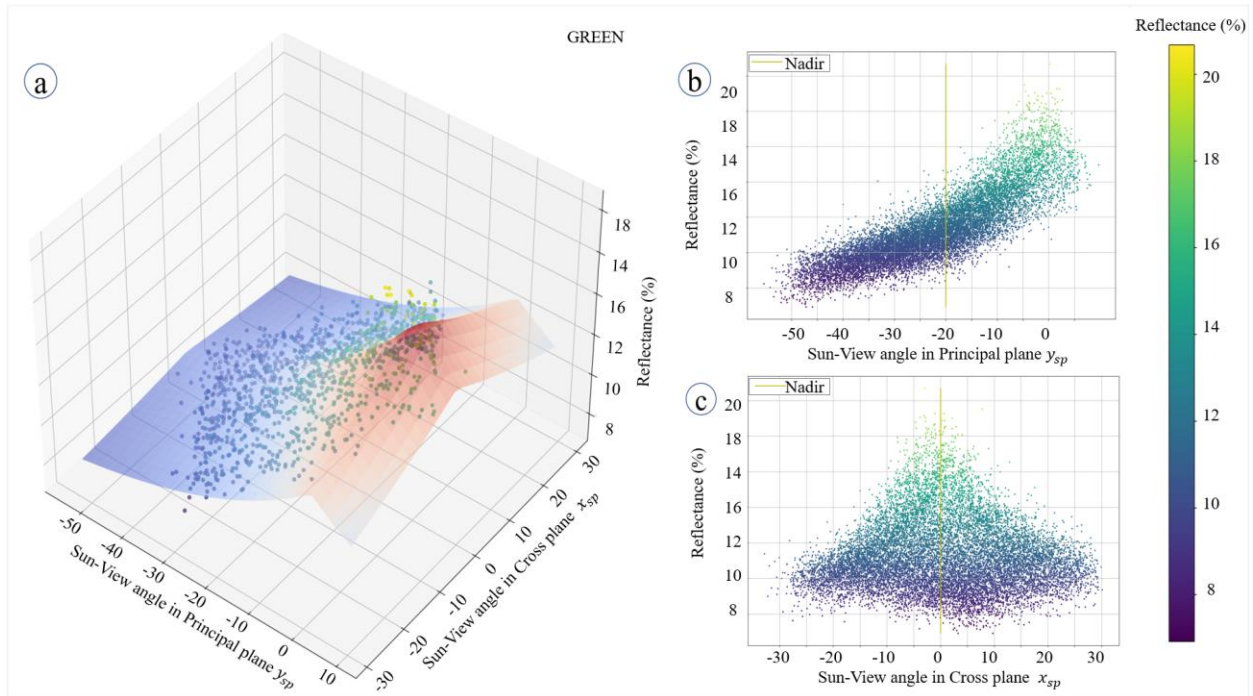


Figure 2.6- 3D representation of data points and fitted model(a). data distribution in principal plane ( $y_{sp}$ ) direction (b), and data distribution in cross plane ( $x_{sp}$ ) direction (c). The proposed model can predict the reflectance from different view angles by  $R^2$  of 0.85. (the interactive 3D plot is accessible at: <https://chart-studio.plotly.com/~hamid39/1>)

The effect of directional radiations was large enough to dwarf all other variation sources. Figure 2.7 shows the magnitude of reflectance variations due to the anisotropic properties of the canopies and view angles in different bands. In this figure, orange bars (right) show the whole reflectance variation (RMSD) in the camera's FOV. Blue bars (middle) show the standard deviation of the prime views, and the gray bars (left) show the primes' variation from the model prediction (potential error due to solar radiation in prime views). The error term (reflectance variation due to the directional radiation) is almost half of the reflectance variation of the Prime views (in  $\sim 10^\circ$ -FOV) for all bands. In other words, based on the model predictions, about half of the variations in the prime views result from directional radiations.

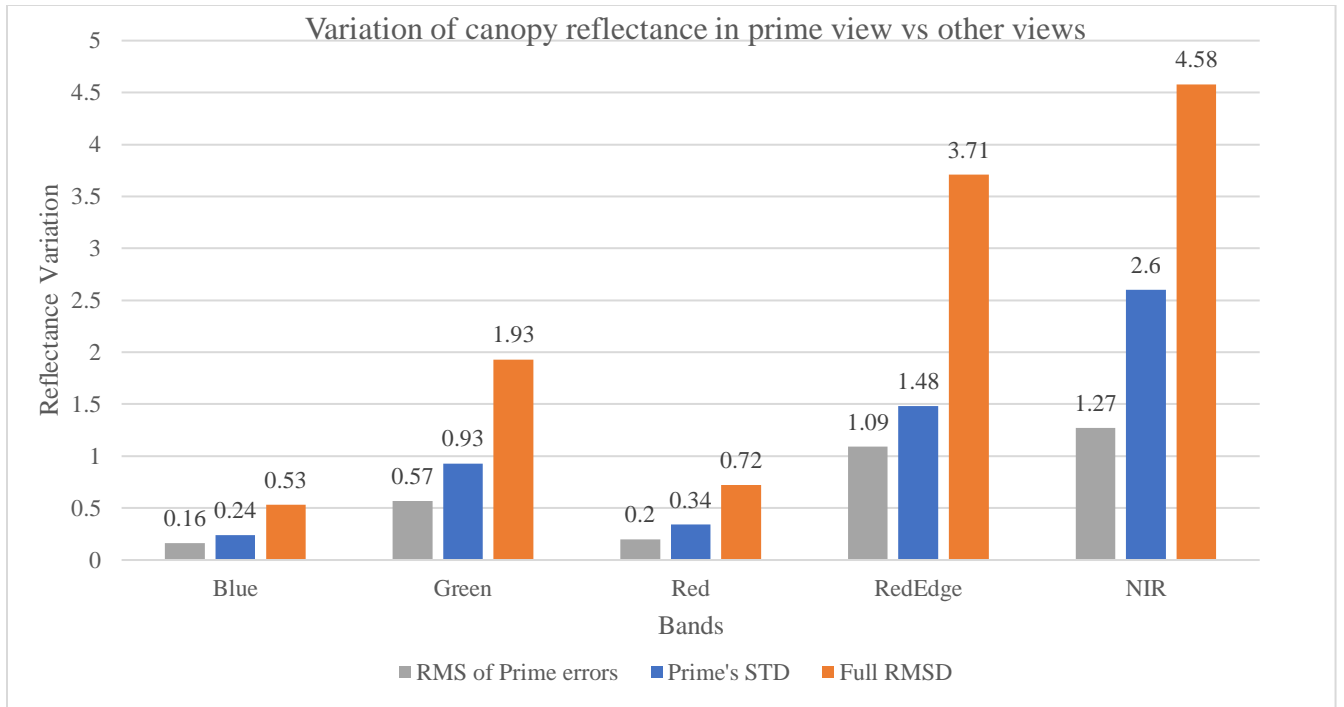


Figure 2.7- Variation of canopy reflectance in prime view (close to nadir) vs. other views (off-nadir). Reflectance variation in different views emerges from objects' anisotropic properties and directional solar radiations. RMS of prime errors (difference between predicted Prime ( $\theta_r=0$ ) and measured Prime ( $\theta_r \sim 0$ ), Prime's STD, and RMSD of all trees show the magnitude of directional effects. Note that the variations at each band are proportional to the magnitude of reflectance.

### 2.3.2 Physical-based Simulation

4Sail results for the same wavelengths as the MRE camera with the parameters presented in Table 2.3 are compared to actual UAS-based data and are shown in Figure 2.8. It is clear that the hotspot effect is very concentrated in the 4Sail results, but in reality, the hotspot effect is much wider and gradually diminishes toward the edges. However, the magnitude of the effect is more or less similar in both 4Sail simulation and actual UAS-based data. Additionally, the hotspot effect clearly propagates to the NDVI as can be seen in both data.

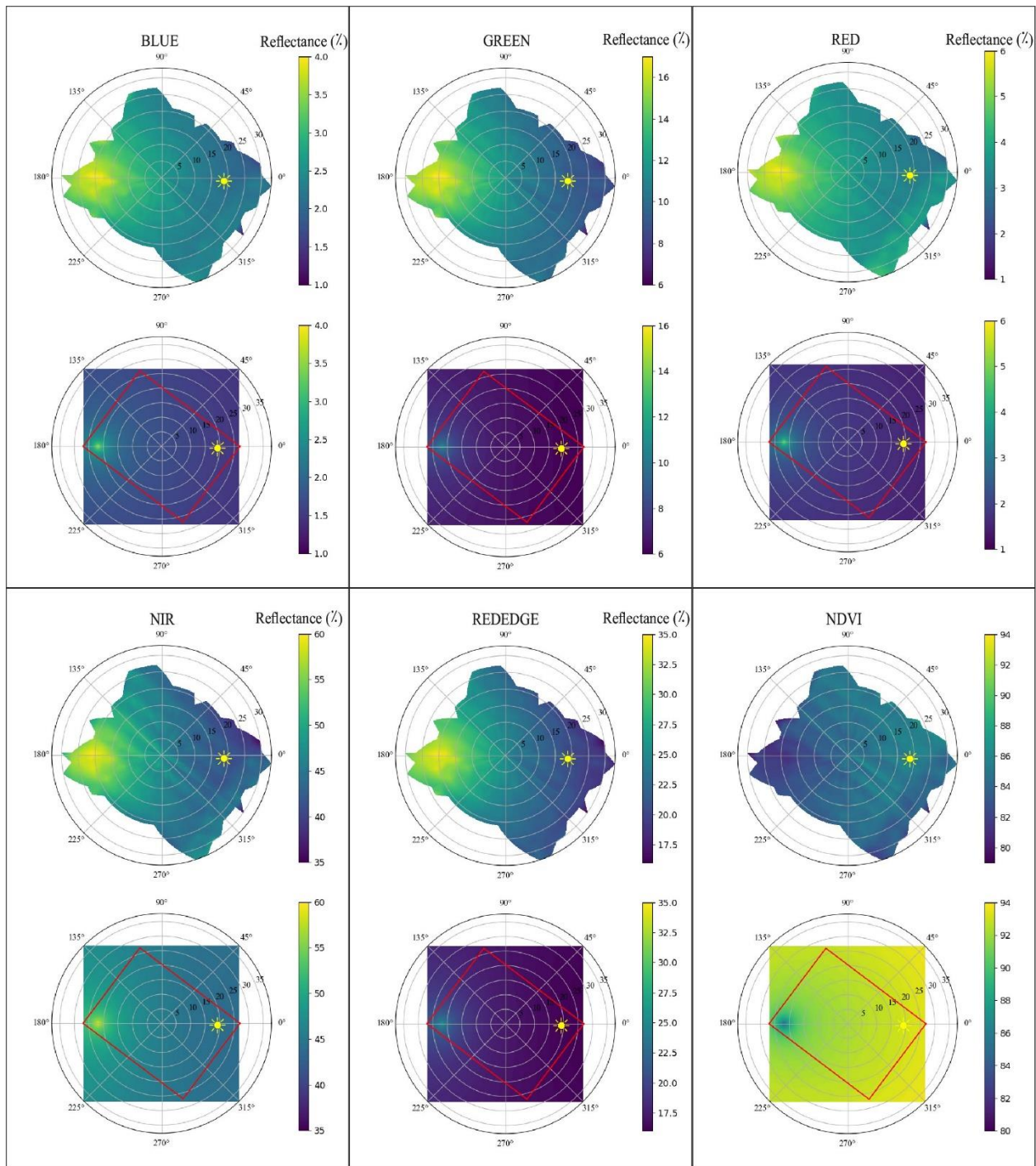


Figure 2.8- Reflectance values for UAS-based measurements (top) compared to 4Sail simulation results (bottom) for all bands of the MRE camera plus NDVI. Sun's relative position is shown by \* symbol and red polygon in 4Sail simulations shows the same area as the multispectral images. Hotspot effect in measured data is wider than the simulation results and spreads through the image. Additionally, the hotspot effect propagates to the NDVI which is obvious in both measured data and simulations.



Another interesting observation was related to the reflectance variations throughout the year linked to the solar elevation changes. Plotting reflectance of each canopy based on sun-view angle difference ( $\theta_r - \theta_i$ ) for the 2019 citrus dataset results in a graph shown in Figure 2.9. Data in this graph represent an analogous pattern in all individual datasets forming a larger scale of sun-view angle variations and confirming the model's accuracy. As shown in Figure 2.9, when  $\theta_i$  is small (higher solar elevation,  $\alpha$ , during summer months), due to the proximity of the hotspot to the image frame, the reflectance values increase, and the pattern becomes steeper. On the other hand, larger  $\theta_i$  indicates that the hotspot is far from the image frame, and the reflectance values increase smoothly. However, even a dataset with large  $\theta_i$  ( $60^\circ$  in December) did not show a flat response, and variations due to the directional effect were noticeable. The December 3<sup>rd</sup> dataset that has the highest  $\theta_i$  showed that in view angles lower than  $-60^\circ$ , a dark spot emerges that is in accordance with the literature <sup>259</sup>. A dark spot, as opposed to a hotspot, occurs when the view angle and sun angle have a setting in which the camera sees maximum shadows, minimizing the reflectance.

The last factor to consider when correcting reflectance data is irradiance changes. Instantaneous irradiance measurement plays a critical role in generating accurate reflectance data as well as modeling the directional radiation. For instance, the 19/09/05 citrus dataset contains two parts: sunny and cloudy. Due to the irradiance fluctuations, relying only on panels for radiometric calibration produced inaccurate results. Hence, relying on DLS data were inevitable for irradiance correction. Therefore, radiometric calibration using both panel and DLS data generated optimum results. However, the modeling results were unsatisfactory since two different patterns appeared for sunny and cloudy parts. The distribution of points on the  $y_{sp}$ - Reflectance graph for the sunny part was inclined, similar to other sunny datasets, while for the cloudy part it was almost flat. Separating the dataset by cloud condition improved the results significantly. Figure 2.9 contains only the sunny part of the 19/09/05 dataset.

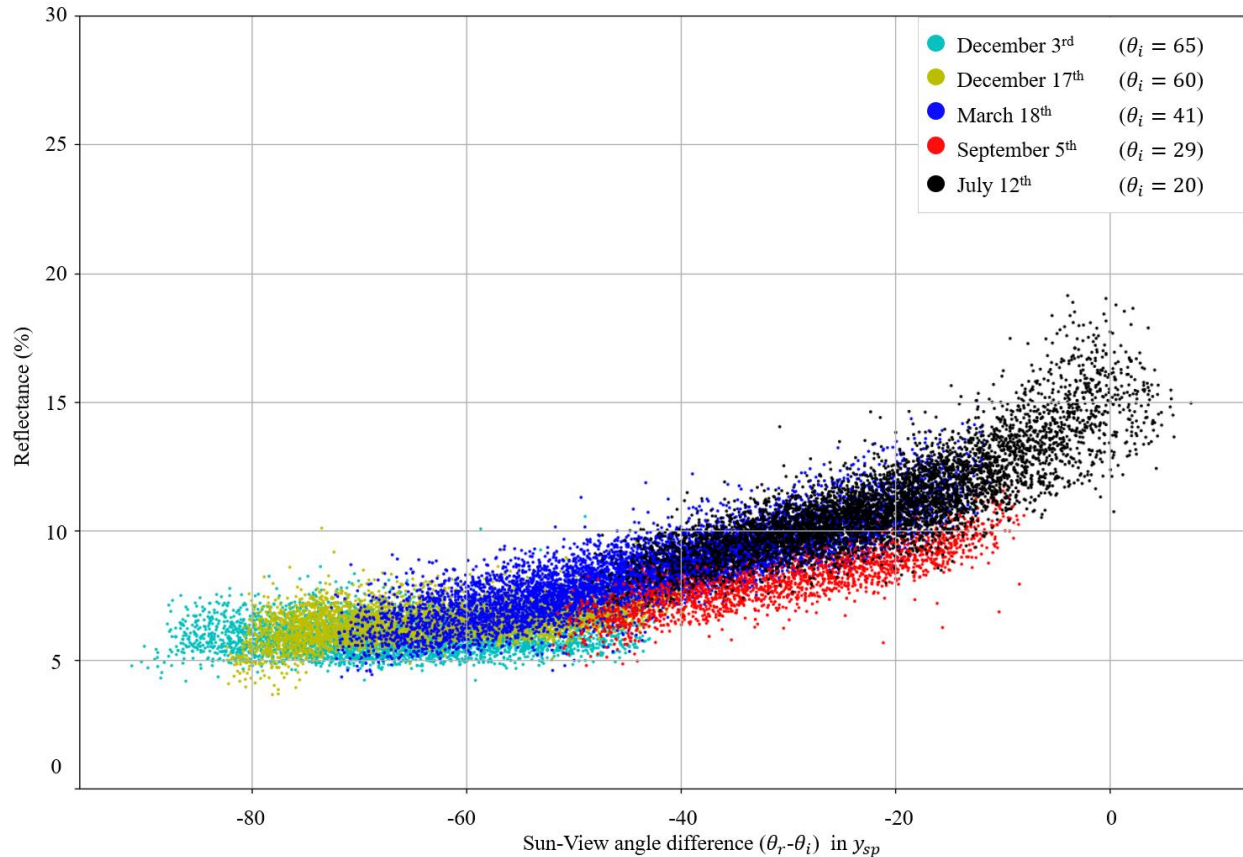


Figure 2.9- Reflectance variations due to the sun-view angle difference ( $\theta_r - \theta_i$ ) throughout the year 2019 for the citrus dataset. The variations in the reflectance under direct illumination are steeper in lower  $\theta_i$  (higher solar elevation) and vice versa.

## 2.4 Discussion

Determining and accounting for the error sources affecting reflectance values is crucial for achieving reliable results in quantitative remote sensing. Nowadays, most studies try to increase their statistical parameters using complex machine learning techniques while, the quality and reliability of their data are questionable<sup>260</sup>. Most of these studies assume that view and illumination directions do not significantly affect the reflectance in the camera's field of view (FOV)<sup>221</sup>. In this research, we investigated the effect of the directional solar radiation on recorded reflectance from different view angles and compared them to 4Sail RTM. We showed that view angle significantly affects reflectance due to directional solar radiation even in small view angle changes. Additionally, results show the importance of instantaneous (real-time) irradiance measurement/estimation. Here, the essential findings of this research are presented, followed

by recommendations to alleviate the detrimental effects of directional radiations on reflectance and improve the results in UAS-based remote sensing data.

The results of the 4Sail simulation are similar to the actual measured data, especially from the magnitude standpoint. However, the span (broadness) of the effect is more concentrated in the 4Sail results than in the actual data. One reason for the concentration of solar effect might be the underlying assumptions that the 4Sail model is based on (such as a homogeneous horizontal plane layer of the canopy while canopies might be very diverse). Newer canopy level RTMs, such as The Discrete Anisotropic Radiative Transfer Model (DART), which are based on Ray Tracing techniques might simulate this effect more accurately. However, these methods are very expensive, time consuming, varying for each field or crop, and they are still under development.

Like other natural phenomena, reflectance variation due to the hotspot effect is a gradual transition with a maximum in the hotspot center, not an abrupt change. Hence, it cannot be treated as a regional issue or separable by a threshold. The results showed that even when the hotspot is outside the image frame, the gradual reflectance increases toward the hotspot. Similar results are presented in <sup>261</sup>.

The closer the hotspot center is to the image frame, the steeper the reflectance dependence on the view angle. As a result, when the hotspot appears inside the image frame, reflectance variation due to the directional solar radiation is maximum. Hence, despite regular recommendations in the literature regarding data collections at solar noon, it is a good practice to adjust the flight time to avoid having the hotspot inside the frame. During solar noon, irradiance variation is minimal and usually negligible (or the variations can be linearly interpolated), which is necessary for panel-based radiometric calibration. However, the unfavorable effects of a hotspot inside the image frames outweigh the benefits of steady irradiance.

When the hotspot does not appear inside the image frame, instead of the complex Laplacian function presented here, a simple linear or quadratic adjustment could be used to increase the accuracy of reflectance values. The camera's FOV and solar elevation (which depends on the site's altitude, date, and time) determine when a dark or hotspot emerges inside the image frame. Figure 2.10 shows the

recommended flight time for a 60°-FOV camera in the central valley of California (the citrus site coordinates are used for this graph) to avoid dark spot and hotspot inside the image frame. The black lines in this figure indicate the upper and lower thresholds to circumvent dark spot in the evenings and mornings. On the other hand, the red lines show the onset and end time of the hotspot within the image frame. As a result, for this specific location and with a 60°-FOV camera, the area between black and red lines is suitable for data collection without hotspot and dark spot disturbances throughout the year.

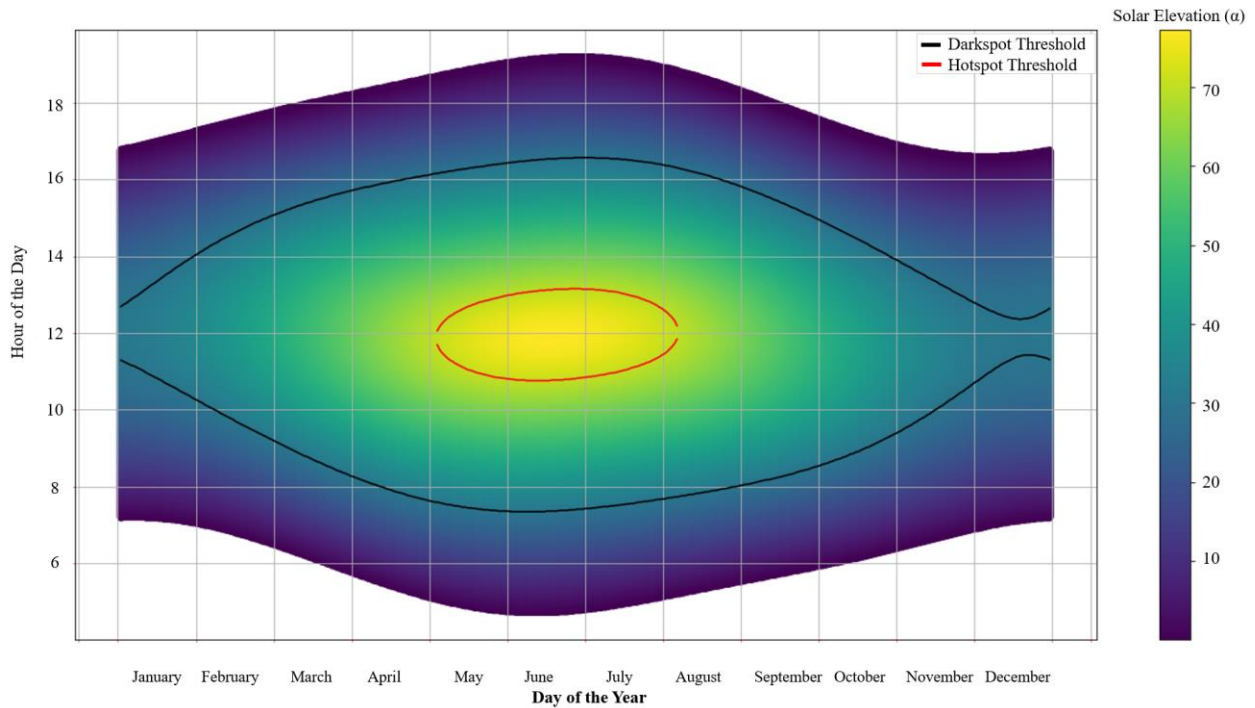


Figure 2.10- Recommended flight time in the central valley of California to avoid darkspot and hotspot throughout the year. The times are without considering daylight saving times.

It is always necessary to correct the reflectance data for different view angles since reflectance data from different view angles are not comparable unless mapped to a reference angle (ex. nadir). However, when the required equipment is unavailable, using a small portion of the image, i.e., similar view angles, that covers the crops of interest could be a quick fix to reduce the directional reflectance variation. For instance, if images are collected with 80% and 85% side and front overlaps, the maximum unique area in each image would be 20% by 15%. Consequently, if 20% by 15% of each image were selected from the center, they could be used to extract the semi-nadir reflectance with minimal directional effects. Slight

adjustments might still be required since the results confirmed that reflectance varies even in small view angle changes. However, the larger the camera FOV, the wider the reflectance variation range. These outputs indicated that data processed by commercial mosaicking software that combine all reflectance values from all view angles and create a mosaic based on averaging techniques are not suitable for agricultural spectral analysis, particularly for specialty crops, where there is a high degree of variability in surface normal.

Following the previous point, more accurate data could be collected by increasing the overlaps. However, larger overlapping increases the operation cost, processing difficulties, and flight time. A longer flight time exposes the images to higher solar angle variations and illumination conditions, which is unfavorable. As a result, a trade-off between image overlaps and flight time is inevitable. An overlap between 75% to 90% is recommended based on crop type and condition, field size, the camera's field of view, and the availability of a suitable time window on the flight date (Figure 2.10).

As explained in the materials and methods, when using DLS that is neither equipped with a reliable cosine corrector nor installed on a gimbal, the flight path should remain perpendicular to the solar plane to ensure that the UAS's pitch fluctuations minimally affect the DLS readings. Refer to Figure A. 2, Figure A. 3, Figure A. 4 in the Appendix for more information.

The panel type used as a reference should be selected carefully. Based on equation 2, reference panels with known loss and near-Lambertian characteristics are required in reflectance calculations. However, near-Lambertian is a general term that does not reflect the accuracy of the calibration needed for agricultural purposes. Particularly, when fabric panels are being used as a reference, the near-Lambertian requirement is entirely questionable due to their anisotropic reflections that show the fabric panels are not even close to near-Lambertian requirement for use as a reference panel. In a future study, reflectance variations due to sun-view angle differences from these panels will be studied.

The modeling and results were consistent for citrus, almond, and grape. However, more research is needed to expand these results for other crops. In fact, the hotspot magnitude (studied extensively in radiate transfer models) depends on the size and distances between the leaves, canopy size and height, as

well as the distribution of leaves' surface normal (the way the leaf surfaces are distributed, ex., erectophile or planophile)<sup>256</sup>. This leads to the fact that a single canopy can be in the hotspot center under two different sun-view geometry (e.g.,  $\theta_r = \theta_i = 30$ , and  $\theta_r = \theta_i = 20$ , which results in  $\theta_r - \theta_i = 0$ ) yet show different reflectance values. Knowledge about the anisotropic reflectance of the canopy is necessary to handle all variation sources.

Numerous studies focused on nitrogen estimation, yield prediction, water stress, etc., using NDVI and NDRE. The values of NDVI for tree canopies usually start from around 0.80 and become saturated at around 0.90<sup>262</sup>. As a result, all conclusions are based on a slight variation (5% of the whole dynamic range) of NDVI. However, as presented in Figure 2.5- f, as well as 4Sail results, the normalized indices such as NDVI could also be affected by directional radiations since it is a wavelength-dependent effect. For instance, in the 19/06/12 dataset, the NDVI variation within the camera's FOV is 40% higher than the variation in Prime views, which agrees with<sup>263</sup> for hyperspectral UAV data and<sup>236</sup> for satellite images.

A similar study with a hyperspectral camera could shed light on the dependency level of different wavelengths on directional radiations. Simultaneously, it would be interesting to investigate different ratios of directional radiations to diffuse radiations,  $d$  in Equation 2.5, on reflectance measured from different angles. It is expected that the slope of the model will increase with increasing  $d$ .

## 2.5 Conclusion

In this study, the effect of directional solar radiation on the reflectance data was discussed. Results showed that the reflectance in each band significantly depends on the sun-view angle. Reflectance variations for individual bands and for NDVI in the camera's FOV could vary as high as 100% and 40% from the prime view, respectively. The 4Sail simulations were in agreement with the measured data. The effect of dark-spot/ hotspot is not an abrupt change or a regional issue, but it is a gradual change that appears in all sun-view angle settings. Without considering these effects, any analytics might be erroneous, and conclusions could be misleading. Appropriate time of flight should be calculated and used based on the camera FOV, time of the year, and site location latitude to reduce the detrimental impact of darkspot/ hotspot (similar to Figure 2.10). If equipment or resources for correcting all images are not

available, using a small portion from the center of each image to extract near-nadir data could produce better results than commercial stitching software that combine all images to form a mosaic. As discussed in the chapter, a DLS sensor equipped with a reliable cosine corrector or installed on a gimbal would be necessary. Alternatively, a UAS with reliable IMU data could be used to account for both camera and DLS roll and pitch corrections.

Using the developed model, the nadir view ( $\theta_r=0$ ) reflectance for each canopy could be calculated from other (non-nadir) views. The nadir reflectance ensures that directional radiation factors do not affect the measured values in a specific sun angle. The results of this research are based on the analysis of aerial multispectral imagery of three crops (citrus, almond, and grape). Although we expect similar results from other crops, especially those with similar leaf size and distribution, more research is needed to generalize the developed model. Repeating this experiment with hyperspectral data could help determine the spectral dependency of variations due to the directional radiations.

### 3 Overall Conclusions and Future Work

#### 3.1 Overall Discussion and Conclusions

Even though remote sensing and digital agriculture has the potential to revolutionize the agricultural industry, lack of a standard data collection procedure, the noises introduced to the data at different stages from data collection step to the processing step, prevents producing reliable and generalizable results. In this study, we tried to understand these problems and take a step forward solving them and improve data quality. For this purpose, we investigated the important assumptions in remote sensing and identified those that lead to unreliable results.

The crucial requirement of remote sensing data for drawing conclusions is that the collected data must depend only on the surface texture and body properties of the object, not anything else. This is the most critical point in remote sensing that form the foundation of radiometric calibration that tries to account for external factors such as changes in environment illumination, sensor setting, noises, and imperfections. The main assumption is that the environmental effects and other noises are either accounted for or are negligible. As a result, the measurements that we make with our sensors depend only on the object and its properties. For example, in case of a plant leaf the measured reflectance must be related to constituents of the leaf and its surface. However, based on definition, reflectance depends on the view angle and also illumination angle (if the illumination is not completely diffuse, which is the case in almost all remote sensing applications) as well. As a result, view angle and illumination angles are two factors that affect reflectance but have been considered negligible based on some assumptions.

The first common assumption is that the effect directional irradiance (i.e., sun in clear sky) is negligible. In other words, remote sensing images taken at different hours of a day and different dates in a season knowing the sky irradiance (hemispherical irradiance) without considering solar elevation (zenith angle) can be used for analysis. This raises serious issues, especially, when the flight mission takes place in different dates or hours of a day. To better understand this issue, assume a canopy with a fixed sensor on top of it that measures radiance continuously from sunrise to sunset. Moreover, an irradiance sensor next to the tree with a perfect cosine corrector measures the irradiance continuously to account for illumination



changes. In this scenario, the reflectance values would differ for different hours even after accounting for illumination changes since the interaction between sun direction and physical properties of the canopy such as the leaf inclination distribution function (LIDF), affect the reflectance. Based on the results in this study, directional light significantly affects the reflectance values measured from the same canopy. A similar reasoning exposes the problems throughout seasons. As a common practice, it is suggested to collect data during “solar noon” to minimize the changes irradiance. However, solar elevation varies tens of degrees at solar noon in different seasons. As a result, solar noon cannot be a reliable reference point for data collection. In a special case, this causes hotspot problem, which drastically affects the measured reflectance.

The second common assumption is that the effect of view angle on reflectance within the FOV of the camera is negligible, hence taking nadir images results in a similar response within the image frame. In other words, all areas within a single shot image (this is partially true for line scanned images) can be considered the same. However, our experiments showed that this assumption is also incorrect and the results of measurements in these conditions are not comparable. As a result, the two trees in a single image where one tree is viewed from exactly nadir angle and another viewed slightly from one side, could not be compared.

Considering the effect of view angle and sun angle in reflectance of canopies, only two scenarios to account for the variations are conceivable:

- 1) Taking measurements only from a specific view angle and only when the sun is in a specific direction.

In other words, the camera must have a very narrow horizontal and vertical field of view (FOV), less than  $2^\circ$ , and it must maintain the same view angle throughout the experiment (e.g., nadir). Consequently, covering a field would require significantly more time. Furthermore, the solar elevation (zenith of the sun) must remain consistent across all data collection campaigns. Therefore, data collection hours (of the day) could vary significantly throughout the year, as the sun reaches its highest elevation at a lower angle in the fall than it does at solar noon in the summer. In other words, solar elevation of  $45^\circ$  might occur in different times of day throughout season depending on the latitude. This scenario restricts data collection

to narrow time windows each day. Consequently, this approach is not practical and conflicts with the goals of remote sensing. Capturing narrow-FOV nadir images demands a substantial amount of time, while the available time window, determined by the sun's angle, is excessively brief. Therefore, this approach is impractical.

2) The other possible method is to quantify the effects of view angle and sun angle on the reflectance and calculate the reflectance in a way that it can be comparable to the scenario in which data are collected with a narrow-FOV camera from nadir view and a constant sun angle. We tried to achieve this goal in our study and presented a correction way that with up to 88% accuracy can account for view angle and sun angle variations. However, our study showed that the coefficients differ depending on the crops. Additionally, highly overlapping images are needed to create the correction model.

### 3.2 Future research

In this study, the importance of considering view angle and sun angle on the reflectance readings were investigated and we concluded that quantifying the effects and accounting for them is a potential solution for this issue. Another elegant way of dealing with angles is using computers and technology to realistically simulate the field condition and examine various view angle and sun angles. This enables us to calculate BRDF or HRDF and use it as a tool to calculate reflectance in any direction given one direction. This can be done using Radiative Transfer Model (RTM) in which all components affecting reflectance including soil, leaves, branches, leaf constituents, other plants, etc. are simulated and then sun angle and its irradiance also enters the simulation. Then based on different methods such as ray tracing reflectance in any direction can be accurately estimated. Using RTM and physical based approach can potentially revolutionize remote sensing process since not only can we calculate reflectance in any direction, but also, we can use it to check and balance our sensors and collected data. Investigating RTMs are highly suggested as a future work in this area.

## 4 REFERENCES

1. Campbell M. 5 Main Food Groups. Published December 2018. Accessed December 30, 2019. <https://healthyeating.sfgate.com/5-main-food-groups-3976.html>
2. Alasfoor D, Rajab H, Al-Rassasi B. Food based dietary guidelines, technical background and description. *Muscat Minist Health*. Published online 2007.
3. Shahbandeh M. Per capita consumption of tree nuts in the U.S. 2017. Statista. Published January 29, 2019. Accessed December 30, 2019. <https://www.statista.com/statistics/184216/per-capita-consumption-of-tree-nuts-in-the-us-since-2000/>
4. (California Department of Food and Agriculture. *California Agricultural Statistics Review*. (California Department of Food and Agriculture; 2018:12. Accessed December 18, 2019. <https://www.cdffa.ca.gov/Statistics/PDFs/2017-18AgReport.pdf>
5. United States Department of Agriculture. USDA - National Agricultural Statistics Service - California - Specialty and Other Releases. Published 2020. Accessed February 19, 2021. [https://www.nass.usda.gov/Statistics\\_by\\_State/California/Publications/Specialty\\_and\\_Other\\_Releases/](https://www.nass.usda.gov/Statistics_by_State/California/Publications/Specialty_and_Other_Releases/)
6. (California Department of Food and Agriculture. *2018 California Almond Acreage Report*. (California Department of Food and Agriculture; 2019. [https://www.nass.usda.gov/Statistics\\_by\\_State/California/Publications/Specialty\\_and\\_Other\\_Releases/Almond/Acreage/201904almac.pdf](https://www.nass.usda.gov/Statistics_by_State/California/Publications/Specialty_and_Other_Releases/Almond/Acreage/201904almac.pdf)
7. Zhao T, Stark B, Chen YQ, Ray AL, Doll D. Challenges in Water Stress Quantification Using Small Unmanned Aerial System (sUAS): Lessons from a Growing Season of Almond. *J Intell Robot Syst Theory Appl*. 2017;88(2-4):721-735. doi:10.1007/s10846-017-0513-x
8. García-Tejero IF, Durán-Zuazo VH, Muriel-Fernández JL. Towards sustainable irrigated Mediterranean agriculture: implications for water conservation in semi-arid environments. *Water Int*. 2014;39(5):635-648. doi:10.1080/02508060.2014.931753
9. Costa JM, Grant OM, Chaves MM. Thermography to explore plant–environment interactions. *J Exp Bot*. 2013;64(13):3937-3949. doi:10.1093/jxb/ert029
10. Fedoroff NV, Battisti DS, Beachy RN, et al. Radically rethinking agriculture for the 21st century. *science*. 2010;327(5967):833-834.
11. Lubin DA, Esty DC. The sustainability imperative. *Harv Bus Rev*. 2010;88(5):42-50.
12. Whelan BM, McBratney AB. The “null hypothesis” of precision agriculture management. *Precis Agric*. 2000;2(3):265-279.
13. Rosegrant MW, Koo J, Cenacchi N, et al. *Food Security in a World of Natural Resource Scarcity: The Role of Agricultural Technologies*. Intl Food Policy Res Inst; 2014.
14. Estes J, Kline K, Collins E. Remote Sensing. In: Smelser NJ, Baltes PB, eds. *International Encyclopedia of the Social & Behavioral Sciences*. Pergamon; 2001:13144-13150. doi:10.1016/B0-08-043076-7/02526-2

15. Jones HG, Vaughan RA. *Remote Sensing of Vegetation: Principles, Techniques, and Applications*. Oxford university press; 2010.
16. Matese A, Toscano P, Di Gennaro SF, et al. Intercomparison of UAV, aircraft and satellite remote sensing platforms for precision viticulture. *Remote Sens*. 2015;7(3):2971-2990. doi:10.3390/rs70302971
17. Manfreda S, McCabe MF, Miller PE, et al. On the use of unmanned aerial systems for environmental monitoring. *Remote Sens*. 2018;10(4):641.
18. Watts AC, Ambrosia VG, Hinkley EA. Unmanned aircraft systems in remote sensing and scientific research: Classification and considerations of use. *Remote Sens*. 2012;4(6):1671-1692.
19. Stöcker C, Bennett R, Nex F, Gerke M, Zevenbergen J. Review of the current state of UAV regulations. *Remote Sens*. 2017;9(5):459.
20. Chen B, Jin Y, Brown P. An enhanced bloom index for quantifying floral phenology using multi-scale remote sensing observations. *ISPRS J Photogramm Remote Sens*. 2019;156:108-120.
21. Bellvert J, Adeline K, Baram S, Pierce L, Sanden BL, Smart DR. monitoring crop evapotranspiration and crop coefficients over an almond and pistachio orchard throughout remote sensing. *Remote Sens*. 2018;10(12). doi:10.3390/rs10122001
22. Crawford KE. *Remote Sensing of Almond and Walnut Tree Canopy Temperatures Using an Inexpensive Infrared Sensor on a Small Unmanned Aerial Vehicle*. University of California, Davis; 2014.
23. López-Granados F, Torres-Sánchez J, Jiménez-Brenes FM, Arquero O, Lovera M, de Castro AI. An efficient RGB-UAV-based platform for field almond tree phenotyping: 3-D architecture and flowering traits. *Plant Methods*. 2019;15(1):1-16.
24. Torres-Sánchez J, de Castro AI, Pena JM, et al. Mapping the 3D structure of almond trees using UAV acquired photogrammetric point clouds and object-based image analysis. *Biosyst Eng*. 2018;176:172-184.
25. Erfanifard SY, Chenari A, Dehghani M, Amiraslani F. Effect of spatial resolution of UAV aerial images on height estimation of wild pistachio (*Pistacia atlantica* Desf.) trees. *Iran J For Poplar Res*. 2019;27(2).
26. Gonzalez-Dugo V, Zarco-Tejada P, Berni JAJ, Suárez L, Goldhamer D, Fereres E. Almond tree canopy temperature reveals intra-crown variability that is water stress-dependent. *Agric For Meteorol*. 2012;154-155:156. doi:10.1016/j.agrformet.2011.11.004
27. Gonzalez-Dugo V, Zarco-Tejada P, Nicolás E, et al. Using high resolution UAV thermal imagery to assess the variability in the water status of five fruit tree species within a commercial orchard. *Precis Agric*. 2013;14(6):660-678. doi:10.1007/s11119-013-9322-9
28. Gonzalez-Dugo V, Goldhamer D, Zarco-Tejada PJ, Fereres E. Improving the precision of irrigation in a pistachio farm using an unmanned airborne thermal system. *Irrig Sci*. 2015;33(1):43-52.

29. López-López M, Calderón R, González-Dugo V, Zarco-Tejada P, Fereres E. Early Detection and Quantification of Almond Red Leaf Blotch Using High-Resolution Hyperspectral and Thermal Imagery. *Remote Sens.* 2016;8(4):276. doi:10.3390/rs8040276
30. Camino C, Zarco-Tejada P, Gonzalez-Dugo V. Effects of heterogeneity within tree crowns on airborne-quantified SIF and the CWSI as indicators of water stress in the context of precision agriculture. *Remote Sens.* 2018;10(4):604.
31. Roy S, Ophori D. Estimation of crop water stress index in almond orchards using thermal aerial imagery. *J Spat Hydrol.* 2014;12(1).
32. Cheng T, Riaño D, Ustin SL. Detecting diurnal and seasonal variation in canopy water content of nut tree orchards from airborne imaging spectroscopy data using continuous wavelet analysis. *Remote Sens Environ.* 2014;143:39-53. doi:10.1016/j.rse.2013.11.018
33. Zhang Z, Jin Y, Chen B, Brown P. California almond yield prediction at the orchard level with a machine learning approach. *Front Plant Sci.* 2019;10:809.
34. Li H, Zhang C, Zhang S, Atkinson PM. Full year crop monitoring and separability assessment with fully-polarimetric L-band UAVSAR: A case study in the Sacramento Valley, California. *Int J Appl Earth Obs Geoinformation.* 2019;74:45-56. doi:10.1016/j.jag.2018.08.024
35. Shivers SW, Roberts DA, McFadden JP. Using paired thermal and hyperspectral aerial imagery to quantify land surface temperature variability and assess crop stress within California orchards. *Remote Sens Environ.* 2019;222:215-231. doi:10.1016/j.rse.2018.12.030
36. Jin Y, He R, Marino G, et al. Spatially variable evapotranspiration over salt affected pistachio orchards analyzed with satellite remote sensing estimates. *Agric For Meteorol.* 2018;262:178-191. doi:10.1016/j.agrformet.2018.07.004
37. He R, Jin Y, Kandelous M, et al. Evapotranspiration estimate over an almond orchard using landsat satellite observations. *Remote Sens.* 2017;9(5):436.
38. Fadaei H, Sakai T, Torii K. Investigation on pistachio distribution in the mountain regions of northeast Iran by ALOS. *Front Agric China.* 2011;5(3):393. doi:10.1007/s11703-011-1108-0
39. Kramer H. UAVSAR - eoPortal Directory - Airborne Sensors. Published 2013. Accessed February 19, 2021. <https://earth.esa.int/web/eoportal/airborne-sensors/uavsar>
40. Dempsey ME, Rasmussen S. Eyes of the army—US Army roadmap for unmanned aircraft systems 2010–2035. *US Army UAS Cent Excell Ft Rucker Alabma.* 2010;9.
41. Federal Aviation Administration. Fact Sheet – Small Unmanned Aircraft Regulations (Part 107). Published 2020. Accessed June 22, 2020. [https://www.faa.gov/news/fact\\_sheets/news\\_story.cfm?newsId=22615](https://www.faa.gov/news/fact_sheets/news_story.cfm?newsId=22615)
42. FAADroneZone. FAADroneZone. Published 2020. Accessed February 20, 2021. <https://faadronezone.faa.gov/#/>

43. Andrew Simpson, T. Stombaugh, L. Wells, J. Jacob. Imaging Techniques and Applications for UAV's in Agriculture. In: 2003, *Las Vegas, NV July 27-30, 2003*. American Society of Agricultural and Biological Engineers; 2003. doi:10.13031/2013.14929
44. MIT Technology Review. 10 Most Important Technology Milestones for 2014. MIT Technology Review. Published 2014. Accessed January 3, 2020. <https://www.technologyreview.com/lists/technologies/2014/>
45. Federal Aviation Administration. FAA Releases Aerospace Forecast. Published 2018. Accessed December 23, 2019. <https://www.faa.gov/news/updates/?newsId=89870>
46. Mazur M, Wisniewski A, McMillan J. Clarity from above: PwC global report on the commercial applications of drone technology. *Wars Drone Powered Solut PriceWater House Coopers*. Published online 2016.
47. Barnes J. Drones vs Satellites: Competitive or Complementary? | Commercial UAV News. Published 2018. Accessed January 2, 2020. <https://www.commercialuavnews.com/infrastructure/drones-vs-satellites-competitive-complimentary>
48. Zhao T. REMOTE SENSING OF WATER STRESS IN ALMOND TREES USING UNMANNED AERIAL VEHICLES. Published online 2018:131.
49. García-Tejero IF, Ortega-Arévalo CJ, Iglesias-Contreras M, et al. Assessing the crop-water status in almond (*Prunus dulcis* mill.) trees via thermal imaging camera connected to smartphone. *Sens Switz*. 2018;18(4). doi:10.3390/s18041050
50. FAA U. Summary of small unmanned aircraft rule (part 107). *Wash DC Fed Aviat Adm*. Published online 2016.
51. Hunt ER, Hively WD, Fujikawa SJ, Linden DS, Daughtry CST, McCarty GW. Acquisition of NIR-Green-Blue Digital Photographs from Unmanned Aircraft for Crop Monitoring. *Remote Sens*. 2010;2(1):290-305. doi:10.3390/rs2010290
52. National Agricultural Aviation Association. Published 2001. Accessed January 23, 2020. <https://www.agaviation.org/industryhistory>
53. Rees WG. *Physical Principles of Remote Sensing*. Cambridge University Press; 2013.
54. Schmutge T, Blanchard B, Anderson A, Wang J. SOIL MOISTURE SENSING WITH AIRCRAFT OBSERVATIONS OF THE DIURNAL RANGE OF SURFACE TEMPERATURE 1. *JAWRA J Am Water Resour Assoc*. 1978;14(1):169-178.
55. Schmutge TJ, Jackson TJ, McKim HL. Survey of methods for soil moisture determination. *Water Resour Res*. 1980;16(6):961-979.
56. Sarah Lundeen, Ken Gowey. AVIRIS - Airborne Visible / Infrared Imaging Spectrometer - Data Processing. Published 2021. Accessed February 26, 2020. [https://aviris.jpl.nasa.gov/aviris/data\\_facility.html](https://aviris.jpl.nasa.gov/aviris/data_facility.html)

57. Bellvert J, Zarco-Tejada PJ, Marsal J, Girona J, González-Dugo V, Fereres E. Vineyard irrigation scheduling based on airborne thermal imagery and water potential thresholds. *Aust J Grape Wine Res.* 2016;22(2):307-315. doi:10.1111/ajgw.12173
58. Campbell JB, Wynne RH. *Introduction to Remote Sensing*. Guilford Press; 2011.
59. Stafford JV. Implementing precision agriculture in the 21st century. *J Agric Eng Res.* 2000;76(3):267-275.
60. Hawley AJ. *Remote Sensing: With Special Reference to Agriculture and Forestry*. JSTOR; 1971.
61. von Bueren S, Burkart A, Hueni A, Rascher U, Tuohy M, Yule I. Comparative validation of UAV based sensors for the use in vegetation monitoring. *Biogeosciences Discuss.* 2014;11(3):3837-3864.
62. Walter V, Saska M, Franchi A. Fast mutual relative localization of uavs using ultraviolet led markers. In: *2018 International Conference on Unmanned Aircraft Systems (ICUAS)*. IEEE; 2018:1217-1226.
63. Gordon IE, Rothman LS, Hill C, et al. The HITRAN2016 molecular spectroscopic database. *J Quant Spectrosc Radiat Transf.* 2017;203:3-69.
64. Jensen JR. *Remote Sensing of the Environment: An Earth Resource Perspective 2/e*. Pearson Education India; 2009.
65. Liang S, Wang J. *Advanced Remote Sensing: Terrestrial Information Extraction and Applications*. Academic Press; 2019.
66. History of the camera. In: *Wikipedia*. ; 2020. Accessed July 8, 2020. [https://en.wikipedia.org/w/index.php?title=History\\_of\\_the\\_camera&oldid=963373872](https://en.wikipedia.org/w/index.php?title=History_of_the_camera&oldid=963373872)
67. Padmavathi K, Thangadurai K. Implementation of RGB and grayscale images in plant leaves disease detection—comparative study. *Indian J Sci Technol.* 2016;9(6):1-6.
68. Woebbecke DM, Meyer GE, Von Bargen K, Mortensen DA. Shape features for identifying young weeds using image analysis. *Trans ASAE.* 1995;38(1):271-281.
69. Neto JC. *A Combined Statistical-Soft Computing Approach for Classification and Mapping Weed Species in Minimum-Tillage Systems*. The University of Nebraska-Lincoln; 2004.
70. Hague T, Tillett ND, Wheeler H. Automated crop and weed monitoring in widely spaced cereals. *Precis Agric.* 2006;7(1):21-32.
71. Kataoka T, Kaneko T, Okamoto H, Hata S. Crop growth estimation system using machine vision. In: *Proceedings 2003 IEEE/ASME International Conference on Advanced Intelligent Mechatronics (AIM 2003)*. Vol 2. IEEE; 2003:b1079-b1083.
72. Montalvo M, Guerrero JM, Romeo J, Emmi L, Guijarro M, Pajares G. Automatic expert system for weeds/crops identification in images from maize fields. *Expert Syst Appl.* 2013;40(1):75-82.
73. Zheng H, Cheng T, Li D, et al. Evaluation of RGB, color-infrared and multispectral images acquired from unmanned aerial systems for the estimation of nitrogen accumulation in rice. *Remote Sens.* 2018;10(6):824.

74. Ashapure A, Jung J, Chang A, Oh S, Maeda M, Landivar J. A comparative study of RGB and multispectral sensor-based cotton canopy cover modelling using multi-temporal UAS data. *Remote Sens.* 2019;11(23):2757.
75. Qin J, Chao K, Kim MS, Lu R, Burks TF. Hyperspectral and multispectral imaging for evaluating food safety and quality. *J Food Eng.* 2013;118(2):157-171.
76. Adão T, Hruška J, Pádua L, et al. Hyperspectral imaging: A review on UAV-based sensors, data processing and applications for agriculture and forestry. *Remote Sens.* 2017;9(11):1110.
77. MicaSense. RedEdge-MX | MicaSense. Published 2020. Accessed February 27, 2021. <https://micasense.com/rededge-mx/>
78. Liu JG. REMOTE SENSING | Passive Sensors☆. In: *Reference Module in Earth Systems and Environmental Sciences*. Elsevier; 2013. doi:10.1016/B978-0-12-409548-9.02956-0
79. Stark B, Smith B, Chen Y. Survey of thermal infrared remote sensing for Unmanned Aerial Systems. In: *2014 International Conference on Unmanned Aircraft Systems (ICUAS)*. IEEE; 2014:1294-1299.
80. Myneni RB, Hall FG, Sellers PJ, Marshak AL. The interpretation of spectral vegetation indexes. *IEEE Trans Geosci Remote Sens.* 1995;33(2):481-486.
81. Xue J, Su B. Significant remote sensing vegetation indices: A review of developments and applications. *J Sens.* 2017;2017.
82. Soo Chin Liew. Principles of Remote Sensing - Centre for Remote Imaging, Sensing and Processing, CRISP. Published 2001. Accessed July 25, 2020. <https://crisp.nus.edu.sg/~research/tutorial/optical.htm>
83. Omid R, Moghimi A, Pourreza A, El-Hadedy M, Eddin AS. Ensemble Hyperspectral Band Selection for Detecting Nitrogen Status in Grape Leaves. *ArXiv Prepr ArXiv201004225*. Published online 2020.
84. Kim MS, Daughtry CST, Chappelle EW, McMurtrey JE, Walthall CL. The use of high spectral resolution bands for estimating absorbed photosynthetically active radiation (A par). Published online 1994.
85. Ishimwe R, Abutaleb K, Ahmed F. Applications of thermal imaging in agriculture—A review. *Adv Remote Sens.* 2014;3(03):128.
86. Palluconi FD, Meeks GR. Thermal infrared multispectral scanner (TIMS): An investigator's guide to TIMS data. Published online 1985.
87. Deane S, Avdelidis NP, Ibarra-Castanedo C, et al. Comparison of Cooled and Uncooled IR Sensors by Means of Signal-to-Noise Ratio for NDT Diagnostics of Aerospace Grade Composites. *Sensors.* 2020;20(12):3381.
88. Matese A, Di Gennaro SF. Practical applications of a multisensor UAV platform based on multispectral, thermal and RGB high resolution images in precision viticulture. *Agric Switz.* 2018;8(7). doi:10.3390/agriculture8070116



89. Fuchs M. Infrared measurement of canopy temperature and detection of plant water stress. *Theor Appl Climatol*. 1990;42(4):253-261. doi:10.1007/BF00865986
90. Calderón R, Navas-Cortés JA, Lucena C, Zarco-Tejada PJ. High-resolution airborne hyperspectral and thermal imagery for early detection of Verticillium wilt of olive using fluorescence, temperature and narrow-band spectral indices. *Remote Sens Environ*. 2013;139:231-245.
91. Berni JAJ, Zarco-Tejada PJ, Suárez L, Fereres E. Thermal and narrowband multispectral remote sensing for vegetation monitoring from an unmanned aerial vehicle. *IEEE Trans Geosci Remote Sens*. 2009;47(3):722-738. doi:10.1109/TGRS.2008.2010457
92. Dubayah RO, Drake JB. Lidar remote sensing for forestry. *J For*. 2000;98(6):44-46.
93. Morsy S, Shaker A, El-Rabbany A. Multispectral LiDAR data for land cover classification of urban areas. *Sensors*. 2017;17(5):958.
94. Lim K, Treitz P, Wulder M, St-Onge B, Flood M. LiDAR remote sensing of forest structure. *Prog Phys Geogr*. 2003;27(1):88-106.
95. Steele-Dunne SC, McNairn H, Monsivais-Huertero A, Judge J, Liu PW, Papathanassiou K. Radar remote sensing of agricultural canopies: A review. *IEEE J Sel Top Appl Earth Obs Remote Sens*. 2017;10(5):2249-2273.
96. UAVSAR. What is UAVSAR? - UAVSAR. Published 2014. Accessed February 2, 2020. <https://uavsar.jpl.nasa.gov/education/what-is-uavsar.html>
97. Noviello C, Esposito G, Fasano G, Renga A, Soldovieri F, Catapano I. Small-UAV Radar Imaging System Performance with GPS and CDGPS Based Motion Compensation. *Remote Sens*. 2020;12(20):3463.
98. Maes WH, Steppe K. Perspectives for remote sensing with unmanned aerial vehicles in precision agriculture. *Trends Plant Sci*. 2019;24(2):152-164.
99. Jones HG. Irrigation scheduling: advantages and pitfalls of plant-based methods. *J Exp Bot*. 2004;55(407):2427-2436. doi:10.1093/jxb/erh213
100. Flexas J, Escalona JM, Evain S, et al. Steady-state chlorophyll fluorescence (Fs) measurements as a tool to follow variations of net CO<sub>2</sub> assimilation and stomatal conductance during water-stress in C<sub>3</sub> plants. *Physiol Plant*. 2002;114(2):231-240.
101. Fulton A, Grant J, Buchner R, Connell J. Using the Pressure Chamber for Irrigation Management in Walnut, Almond and Prune. Published online May 1, 2014. doi:10.3733/ucanr.8503
102. Savage MJ, Wiebe HH, Cass A. In situ field measurement of leaf water potential using thermocouple psychrometers. *Plant Physiol*. 1983;73(3):609-613.
103. Underwood JP, Hung C, Whelan B, Sukkarieh S. Mapping almond orchard canopy volume, flowers, fruit and yield using lidar and vision sensors. *Comput Electron Agric*. 2016;130:83-96.
104. Mahajan S, Tuteja N. Cold, salinity and drought stresses: an overview. *Arch Biochem Biophys*. 2005;444(2):139-158.

105. García-Tejero I, Durán-Zuazo VH, Arriaga J, Hernández A, Vélez LM, Muriel-Fernández JL. Approach to assess infrared thermal imaging of almond trees under water-stress conditions. *Fruits*. 2012;67(6):463-474. doi:10.1051/fruits/2012040
106. Gomes-Laranjo J, Coutinho JP, Galhano V, Cordeiro V. Responses of five almond cultivars to irrigation: Photosynthesis and leaf water potential. *Agric Water Manag*. 2006;83(3):261-265.
107. McCutchan H, Shackel KA. Stem-water potential as a sensitive indicator of water stress in prune trees (*Prunus domestica* L. cv. French). *J Am Soc Hortic Sci*. 1992;117(4):607-611.
108. Thenot F, Méthy M, Winkel T. The Photochemical Reflectance Index (PRI) as a water-stress index. *Int J Remote Sens*. 2002;23(23):5135-5139.
109. Testi L, Goldhamer DA, Iniesta F, Salinas M. Crop water stress index is a sensitive water stress indicator in pistachio trees. *Irrig Sci*. 2008;26(5):395-405. doi:10.1007/s00271-008-0104-5
110. Dhillon R, Udompetaikul V, Rojo F, et al. Detection of plant water stress using leaf temperature and microclimatic measurements in almond, walnut, and grape crops. *Trans ASABE*. 2014;57(1):297-304.
111. Gao BC. NDWI—A normalized difference water index for remote sensing of vegetation liquid water from space. *Remote Sens Environ*. 1996;58(3):257-266.
112. Peñuelas J, Filella I, Biel C, Serrano L, Save R. The reflectance at the 950–970 nm region as an indicator of plant water status. *Int J Remote Sens*. 1993;14(10):1887-1905.
113. Pourreza A, Lee WS, Profile S, Roberts PD. *Development of a Multiband Sensor for Citrus Black Spot Disease Detection Virtual Orchard View Project Watermelon Kousik View Project.*; 2016. <https://www.researchgate.net/publication/307460923>
114. González-Dugo MP, Moran MS, Mateos L, Bryant R. Canopy temperature variability as an indicator of crop water stress severity. *Irrig Sci*. 2006;24(4):233.
115. Bellvert J, Zarco-Tejada PJ, Girona J, Fereres E. Mapping crop water stress index in a ‘Pinot-noir’ vineyard: Comparing ground measurements with thermal remote sensing imagery from an unmanned aerial vehicle. *Precis Agric*. 2014;15(4):361-376. doi:10.1007/s11119-013-9334-5
116. Cole J, Pagay V. Usefulness of early morning stem water potential as a sensitive indicator of water status of deficit-irrigated grapevines (*Vitis vinifera* L.). *Sci Hortic*. 2015;191:10-14.
117. Jones HG. Monitoring plant and soil water status: established and novel methods revisited and their relevance to studies of drought tolerance. *J Exp Bot*. 2006;58(2):119-130.
118. Carrasco-Benavides M, Antunez-Quilobrán J, Baffico-Hernández A, et al. Performance Assessment of Thermal Infrared Cameras of Different Resolutions to Estimate Tree Water Status from Two Cherry Cultivars: An Alternative to Midday Stem Water Potential and Stomatal Conductance. *Sensors*. 2020;20(12):3596.
119. Shackel K, Edstrom J, Fulton A, et al. Drought survival strategies for established almond orchards on shallow soil. *Modesto CA*. 2011;2012.

120. Timmerman AD, Korus K. Introduction to Plant diseases. *Board Regents Univ Neb*. Published online 2014. <https://extensionpublications.unl.edu/assets/pdf/ec1273.pdf>
121. Lucas GB, Campbell L. *Introduction to Plant Diseases: Identification and Management*. Springer Science & Business Media; 2012.
122. Brown JK. Durable resistance of crops to disease: a Darwinian perspective. *Annu Rev Phytopathol*. 2015;53:513-539.
123. Omid R, Pourreza A, Moghimi A, et al. A Semi-supervised approach to cluster symptomatic and asymptomatic leaves in root lesion nematode infected walnut trees. *Comput Electron Agric*. 2022;194:106761. doi:10.1016/j.compag.2022.106761
124. Lechenet M, Dessaint F, Py G, Makowski D, Munier-Jolain N. Reducing pesticide use while preserving crop productivity and profitability on arable farms. *Nat Plants*. 2017;3(3):1-6.
125. Pourreza A, Moghimi A, Niederholzer FJA, et al. Spray Backstop: A Method to Reduce Orchard Spray Drift Potential without Limiting the Spray and Air Delivery. *Sustainability*. 2020;12(21):8862. doi:10.3390/su12218862
126. Avenot HF, Morgan DP, Quattrini J, Michailides TJ. Resistance to thiophanate-methyl in *Botrytis cinerea* isolates from Californian vineyards and pistachio and pomegranate orchards. *Plant Dis*. 2020;104(4):1069-1075.
127. Strickland RM, Ess DR, Parsons SD. Precision farming and precision pest management: the power of new crop production technologies. *J Nematol*. 1998;30(4):431.
128. Iost Filho FH, Heldens WB, Kong Z, de Lange ES. Drones: innovative technology for use in precision pest management. *J Econ Entomol*. 2020;113(1):1-25.
129. Sugiura R, Tsuda S, Tamiya S, et al. Field phenotyping system for the assessment of potato late blight resistance using RGB imagery from an unmanned aerial vehicle. *Biosyst Eng*. 2016;148:1-10.
130. Albetis J, Duthoit S, Guttler F, et al. Detection of Flavescence dorée grapevine disease using Unmanned Aerial Vehicle (UAV) multispectral imagery. *Remote Sens*. 2017;9(4). doi:10.3390/rs9040308
131. Mahlein AK. Plant disease detection by imaging sensors—parallels and specific demands for precision agriculture and plant phenotyping. *Plant Dis*. 2016;100(2):241-251.
132. Calderón R, Navas-Cortés J, Zarco-Tejada P. Early detection and quantification of *Verticillium* wilt in olive using hyperspectral and thermal imagery over large areas. *Remote Sens*. 2015;7(5):5584-5610.
133. Husin NA, Khairunniza-Bejo S, Abdullah AF, Kassim MS, Ahmad D, Azmi AN. Application of Ground-Based LiDAR for Analysing oil palm canopy properties on the occurrence of Basal Stem Rot (BSR) Disease. *Sci Rep*. 2020;10(1):1-16.
134. Westphal A. New Ways of Managing Plant-Parasitic Nematodes Under Study. Published 2019. Accessed December 12, 2019. <https://californiaagnet.com/2019/05/24/new-ways-of-managing-plant-parasitic-nematodes-under-study/>

135. Sankaran S, Maja J, Buchanon S, Ehsani R. Huanglongbing (citrus greening) detection using visible, near infrared and thermal imaging techniques. *Sensors*. 2013;13(2):2117-2130.
136. Westphal A, Maung ZTZ, Doll DA, Yaghmour MA, Chitambar JJ, Subbotin SA. First Report of the Peach Root-Knot Nematode, *Meloidogyne floridensis* Infecting Almond on Root-Knot Nematode Resistant “Hansen 536” and “Bright’s Hybrid 5” Rootstocks in California, USA. *J Nematol*. 2019;51:1-3. doi:10.21307/jofnem-2019-002
137. Khaki S, Wang L. Crop yield prediction using deep neural networks. *Front Plant Sci*. 2019;10:621.
138. Chlingaryan A, Sukkarieh S, Whelan B. Machine learning approaches for crop yield prediction and nitrogen status estimation in precision agriculture: A review. *Comput Electron Agric*. 2018;151:61-69.
139. Jin Y, Chen B, Lampinen BD, Brown PH. Advancing agricultural production with machine learning analytics: yield determinants for California’s almond orchards. *Front Plant Sci*. 2020;11:290.
140. Heslot N, Akdemir D, Sorrells ME, Jannink JL. Integrating environmental covariates and crop modeling into the genomic selection framework to predict genotype by environment interactions. *Theor Appl Genet*. 2014;127(2):463-480.
141. Esfandiarpour-Borujeni I, Javad Hosseinifard S, Shirani H, Zeinadini M, Asghar Besalatpour A. Identifying soil and plant nutrition factors affecting yield in irrigated mature pistachio orchards. *Commun Soil Sci Plant Anal*. 2018;49(12):1474-1490.
142. Maimaitijiang M, Sagan V, Sidike P, Hartling S, Esposito F, Fritschi FB. Soybean yield prediction from UAV using multimodal data fusion and deep learning. *Remote Sens Environ*. 2020;237:111599.
143. Sarron J, Malézieux É, Sané CAB, Faye É. Mango yield mapping at the orchard scale based on tree structure and land cover assessed by UAV. *Remote Sens*. 2018;10(12):1900.
144. Lin G, Tang Y, Zou X, Li J, Xiong J. In-field citrus detection and localisation based on RGB-D image analysis. *Biosyst Eng*. 2019;186:34-44.
145. Horton R, Cano E, Bulanon D, Fallahi E. Peach flower monitoring using aerial multispectral imaging. *J Imaging*. 2017;3(1):2.
146. Chen Y, Lee WS, Gan H, et al. Strawberry yield prediction based on a deep neural network using high-resolution aerial orthoimages. *Remote Sens*. 2019;11(13):1584.
147. Majasalmi T, Stenberg P, Rautiainen M. Comparison of ground and satellite-based methods for estimating stand-level fPAR in a boreal forest. *Agric For Meteorol*. 2017;232:422-432. doi:10.1016/j.agrformet.2016.09.007
148. Peng D, Zhang H, Yu L, et al. Assessing spectral indices to estimate the fraction of photosynthetically active radiation absorbed by the vegetation canopy. *Int J Remote Sens*. 2018;39(22):8022-8040.
149. Delgado JA, Lemunyon J. Nutrient management. In: *Encyclopedia of Soil Science*. Marcel Decker New York; 2006:1157-1160.

150. Stiles WC. Orchard nutrition management. Published online 1991.
151. Delgado JA, Lemunyon J. Nutrient management. In: *Encyclopedia of Soil Science*. Marcel Decker New York; 2006:1157-1160.
152. Obreza TA, Zekri M, Hanlon EA, Morgan K, Schumann A, Rouse R. Soil and leaf tissue testing for commercial citrus production. *Univ Fla Ext Serv SL253*. 2010;4.
153. Saa S, Muhammad S, Brown PH. Development of leaf sampling and interpretation methods and nutrient budget approach to nutrient management in almond (*Prunus dulcis* (Mill.) DA Webb). In: *VII International Symposium on Mineral Nutrition of Fruit Crops 984*. ; 2012:291-296.
154. White PJ, Brown PH. Plant nutrition for sustainable development and global health. *Ann Bot*. 2010;105(7):1073-1080.
155. Obreza TT, Morgan KT. Nutrition of Florida citrus trees. *EDIS*. 2008;2008(2).
156. Shunfeng GE, Zhanling ZHU, Ling P, Qian C, JIANG Y. Soil nutrient status and leaf nutrient diagnosis in the main apple producing regions in China. *Hortic Plant J*. 2018;4(3):89-93.
157. Muhammad S, Khalsa SDS, Brown PH. Nitrogen Management in Citrus and Avocado. *Univ Calif Div Agric Nat Resour UC ANR*. Published online 2018.
158. Roberts TL. Right product, right rate, right time and right place... the foundation of best management practices for fertilizer. *Fertil Best Manag Pract*. 2007;29:1-8.
159. Erickson B, Widmar D, Holland J. *Survey: An inside Look at Precision Agriculture in 2013*.; 2013.
160. Prado Osco L, Marques Ramos AP, Roberto Pereira D, et al. Predicting canopy nitrogen content in citrus-trees using random forest algorithm associated to spectral vegetation indices from UAV-Imagery. *Remote Sens*. 2019;11(24):2925.
161. Osco LP, Ramos APM, Moriya ÉAS, et al. Improvement of leaf nitrogen content inference in Valencia-orange trees applying spectral analysis algorithms in UAV mounted-sensor images. *Int J Appl Earth Obs Geoinformation*. 2019;83:101907.
162. Moghimi A, Pourreza A, Zuniga-Ramirez G, Williams LE, Fidelibus MW. A Novel Machine Learning Approach to Estimate Grapevine Leaf Nitrogen Concentration Using Aerial Multispectral Imagery. *Remote Sens*. 2020;12(21):3515.
163. Zarate-Valdez JL, Muhammad S, Saa S, Lampinen BD, Brown PH. Light interception, leaf nitrogen and yield prediction in almonds: a case study. *Eur J Agron*. 2015;66:1-7.
164. Howitt RE, Kaplan J, Larson D, et al. The economic impacts of Central Valley salinity. *Univ Calif Davis Final Rep State Water Resour Control Board Contract*. Published online 2009:05-417.
165. Wallender WW, Tanji KK. *Agricultural Salinity Assessment and Management*. American Society of Civil Engineers (ASCE); 2011.
166. Shrivastava P, Kumar R. Soil salinity: a serious environmental issue and plant growth promoting bacteria as one of the tools for its alleviation. *Saudi J Biol Sci*. 2015;22(2):123-131.

167. Scudiero E, Corwin D, Anderson R, et al. Remote sensing is a viable tool for mapping soil salinity in agricultural lands. *Calif Agric.* 2017;71(4):231-238.
168. Corwin DL, Scudiero E. Mapping soil spatial variability with apparent soil electrical conductivity (ECa) directed soil sampling. *Soil Sci Soc Am J.* 2019;83(1):3-4.
169. Lobell DB, Lesch SM, Corwin DL, et al. Regional-scale assessment of soil salinity in the Red River Valley using multi-year MODIS EVI and NDVI. *J Environ Qual.* 2010;39(1):35-41.
170. Scudiero E, Skaggs TH, Corwin DL. Regional-scale soil salinity assessment using Landsat ETM+ canopy reflectance. *Remote Sens Environ.* 2015;169:335-343.
171. Scudiero E, Skaggs TH, Corwin DL. Regional scale soil salinity evaluation using Landsat 7, western San Joaquin Valley, California, USA. *Geoderma Reg.* 2014;2:82-90.
172. Scitable. phenotype / phenotypes | Learn Science at Scitable. Published 2014. Accessed November 29, 2020. <https://www.nature.com/scitable/definition/phenotype-phenotypes-35/>
173. Mir RR, Reynolds M, Pinto F, Khan MA, Bhat MA. High-throughput phenotyping for crop improvement in the genomics era. *Plant Sci.* 2019;282:60-72.
174. Kelcey J, Lucieer A. Sensor correction of a 6-band multispectral imaging sensor for UAV remote sensing. *Remote Sens.* 2012;4(5):1462-1493.
175. Goldman DB. Vignette and exposure calibration and compensation. *IEEE Trans Pattern Anal Mach Intell.* 2010;32(12):2276-2288.
176. Aasen H, Burkart A, Bolten A, Bareth G. Generating 3D hyperspectral information with lightweight UAV snapshot cameras for vegetation monitoring: From camera calibration to quality assurance. *ISPRS J Photogramm Remote Sens.* 2015;108:245-259.
177. Guo Y, Senthilnath J, Wu W, Zhang X, Zeng Z, Huang H. Radiometric calibration for multispectral camera of different imaging conditions mounted on a UAV platform. *Sustainability.* 2019;11(4):978.
178. Sekrecka A, Wierzbicki D, Kedzierski M. Influence of the Sun Position and Platform Orientation on the Quality of Imagery Obtained from Unmanned Aerial Vehicles. *Remote Sens.* 2020;12(6):1040.
179. Chen JM, Cihlar J. A hotspot function in a simple bidirectional reflectance model for satellite applications. *J Geophys Res Atmospheres.* 1997;102(D22):25907-25913.
180. Stark B, Zhao T, Chen Y. An analysis of the effect of the bidirectional reflectance distribution function on remote sensing imagery accuracy from small unmanned aircraft systems. In: *2016 International Conference on Unmanned Aircraft Systems (ICUAS)*. IEEE; 2016:1342-1350.
181. Wierzbicki D, Kedzierski M, Fryskowska A. Assessment of the influence of uav image quality on the orthophoto production. *Int Arch Photogramm Remote Sens Spat Inf Sci.* 2015;40(1):1.
182. Mamaghani B, Salvaggio C. Multispectral sensor calibration and characterization for sUAS remote sensing. *Sensors.* 2019;19(20):4453.

183. Martínez-Carricondo P, Agüera-Vega F, Carvajal-Ramírez F, Mesas-Carrascosa FJ, García-Ferrer A, Pérez-Porras FJ. Assessment of UAV-photogrammetric mapping accuracy based on variation of ground control points. *Int J Appl Earth Obs Geoinformation*. 2018;72:1-10.
184. Tagle Casapia MX. Study of radiometric variations in Unmanned Aerial Vehicle remote sensing imagery for vegetation mapping. *Lund Univ GEM Thesis Ser*. Published online 2017.
185. Pandey A, Pati UC. Image mosaicing: A deeper insight. *Image Vis Comput*. 2019;89:236-257. doi:10.1016/j.imavis.2019.07.002
186. Ait-Aoudia S, Mahiou R, Djebli H, Guerrou E. Satellite and Aerial Image Mosaicing - A Comparative Insight. In: *2012 16th International Conference on Information Visualisation*. ; 2012:652-657. doi:10.1109/IV.2012.113
187. Grilli E, Menna F, Remondino F. A review of point clouds segmentation and classification algorithms. *Int Arch Photogramm Remote Sens Spat Inf Sci*. 2017;42:339.
188. Che E, Jung J, Olsen MJ. Object Recognition, Segmentation, and Classification of Mobile Laser Scanning Point Clouds: A State of the Art Review. *Sensors*. 2019;19(4):810. doi:10.3390/s19040810
189. Weiss M, Baret F, Weiss M, et al. Using 3D Point Clouds Derived from UAV RGB Imagery to Describe Vineyard 3D Macro-Structure To cite this version : HAL Id : hal-01454675 Using 3D Point Clouds Derived from UAV RGB Imagery to Describe Vineyard 3D Macro-Structure. Published online 2017. doi:10.3390/rs9020111
190. Perko R, Raggam H, Deutscher J, Gutjahr K, Schardt M. Forest assessment using high resolution SAR data in X-band. *Remote Sens*. 2011;3(4):792-815.
191. Somers B, Asner GP, Tits L, Coppin P. Endmember variability in spectral mixture analysis: A review. *Remote Sens Environ*. 2011;115(7):1603-1616.
192. Xu R, Li C, Paterson AH, Jiang Y, Sun S, Robertson JS. Aerial images and convolutional neural network for cotton bloom detection. *Front Plant Sci*. 2018;8:2235.
193. Allen MP. The problem of multicollinearity. *Underst Regres Anal*. Published online 1997:176-180.
194. Kutner MH, Nachtsheim CJ, Neter J, Li W. *Applied Linear Statistical Models*. Vol 5. McGraw-Hill Irwin New York; 2005.
195. Bocca FF, Rodrigues LHA. The effect of tuning, feature engineering, and feature selection in data mining applied to rainfed sugarcane yield modelling. *Comput Electron Agric*. 2016;128:67-76.
196. Mehmood T, Liland KH, Snipen L, Sæbø S. A review of variable selection methods in partial least squares regression. *Chemom Intell Lab Syst*. 2012;118:62-69.
197. Senawi A, Wei HL, Billings SA. A new maximum relevance-minimum multicollinearity (MRmMC) method for feature selection and ranking. *Pattern Recognit*. 2017;67:47-61.
198. Vanegas F, Bratanov D, Weiss J, Powell K, Gonzalez F. Multi and hyperspectral UAV remote sensing: Grapevine phylloxera detection in vineyards. In: *IEEE Aerospace Conference Proceedings*. Vol 2018-March. IEEE Computer Society; 2018:1-9. doi:10.1109/AERO.2018.8396450

199. Pantazi XE, Moshou D, Alexandridis T, Whetton RL, Mouazen AM. Wheat yield prediction using machine learning and advanced sensing techniques. *Comput Electron Agric.* 2016;121:57-65.
200. Zabalza J, Ren J, Yang M, et al. Novel folded-PCA for improved feature extraction and data reduction with hyperspectral imaging and SAR in remote sensing. *ISPRS J Photogramm Remote Sens.* 2014;93:112-122.
201. Chang Z, Du Z, Zhang F, et al. Landslide Susceptibility Prediction Based on Remote Sensing Images and GIS: Comparisons of Supervised and Unsupervised Machine Learning Models. *Remote Sens.* 2020;12(3):502. doi:10.3390/rs12030502
202. Alajlan N, Bazi Y, Melgani F, Yager RR. Fusion of supervised and unsupervised learning for improved classification of hyperspectral images. *Inf Sci.* 2012;217:39-55. doi:10.1016/j.ins.2012.06.031
203. Colombo R, Bellingeri D, Fasolini D, Marino CM. Retrieval of leaf area index in different vegetation types using high resolution satellite data. *Remote Sens Environ.* 2003;86(1):120-131.
204. Williams LE, Araujo FJ. Correlations among predawn leaf, midday leaf, and midday stem water potential and their correlations with other measures of soil and plant water status in *Vitis vinifera*. *J Am Soc Hortic Sci.* 2002;127(3):448-454.
205. Xue L, Cao W, Luo W, Dai T, Zhu Y. Monitoring leaf nitrogen status in rice with canopy spectral reflectance. *Agron J.* 2004;96(1):135-142.
206. Archontoulis SV, Miguez FE. Nonlinear regression models and applications in agricultural research. *Agron J.* 2015;107(2):786-798.
207. Moghimi A, Yang C, Anderson JA. Aerial hyperspectral imagery and deep neural networks for high-throughput yield phenotyping in wheat. *Comput Electron Agric.* 2020;172:105299.
208. Zheng H, Chen L, Han X, Zhao X, Ma Y. Classification and regression tree (CART) for analysis of soybean yield variability among fields in Northeast China: The importance of phosphorus application rates under drought conditions. *Agric Ecosyst Environ.* 2009;132(1-2):98-105.
209. Herrmann I, Bdolach E, Montekyo Y, Rachmilevitch S, Townsend PA, Karnieli A. Assessment of maize yield and phenology by drone-mounted superspectral camera. *Precis Agric.* 2020;21(1):51-76.
210. Fu Z, Jiang J, Gao Y, et al. Wheat growth monitoring and yield estimation based on multi-rotor unmanned aerial vehicle. *Remote Sens.* 2020;12(3):508.
211. Moghimi A, Yang C, Anderson JA. Aerial hyperspectral imagery and deep neural networks for high-throughput yield phenotyping in wheat. *Comput Electron Agric.* 2020;172:105299.
212. Espinoza CZ, Khot LR, Sankaran S, Jacoby PW. High resolution multispectral and thermal remote sensing-based water stress assessment in subsurface irrigated grapevines. *Remote Sens.* 2017;9(9). doi:10.3390/rs9090961



213. Liu H, Zhu H, Li Z, Yang G. Quantitative analysis and hyperspectral remote sensing of the nitrogen nutrition index in winter wheat. *Int J Remote Sens.* 2020;41(3):858-881. doi:10.1080/01431161.2019.1650984
214. Zhang X, Pourreza A, Cheung KH, Zuniga-Ramirez G, Lampinen BD, Shackel KA. Estimation of Fractional Photosynthetically Active Radiation From a Canopy 3D Model; Case Study: Almond Yield Prediction. *Front Plant Sci.* 2021;12. Accessed March 28, 2022. <https://www.frontiersin.org/article/10.3389/fpls.2021.715361>
215. Oliveira RA, Näsi R, Niemeläinen O, et al. Machine learning estimators for the quantity and quality of grass swards used for silage production using drone-based imaging spectrometry and photogrammetry. *Remote Sens Environ.* 2020;246:111830. doi:10.1016/j.rse.2020.111830
216. Dash JP, Watt MS, Pearse GD, Heaphy M, Dungey HS. Assessing very high resolution UAV imagery for monitoring forest health during a simulated disease outbreak. *ISPRS J Photogramm Remote Sens.* 2017;131:1-14. doi:10.1016/j.isprsjprs.2017.07.007
217. Schaepman-Strub G, Schaepman ME, Painter TH, Dangel S, Martonchik JV. Reflectance quantities in optical remote sensing—definitions and case studies. *Remote Sens Environ.* 2006;103(1):27-42. doi:10.1016/j.rse.2006.03.002
218. Suomalainen J, Oliveira RA, Hakala T, et al. Direct reflectance transformation methodology for drone-based hyperspectral imaging. *Remote Sens Environ.* 2021;266:112691. doi:10.1016/j.rse.2021.112691
219. Smith GM, Milton EJ. The use of the empirical line method to calibrate remotely sensed data to reflectance. *Int J Remote Sens.* 1999;20(13):2653-2662.
220. Rykowski RF, Kreysar DF. Stray light correction method for imaging light and color measurement system. Published online December 13, 2005.
221. Stow D, Nichol CJ, Wade T, Assmann JJ, Simpson G, Helfter C. Illumination Geometry and Flying Height Influence Surface Reflectance and NDVI Derived from Multispectral UAS Imagery. *Drones.* 2019;3(3):55. doi:10.3390/drones3030055
222. Aasen H, Honkavaara E, Lucieer A, Zarco-Tejada PJ. Quantitative remote sensing at ultra-high resolution with UAV spectroscopy: a review of sensor technology, measurement procedures, and data correction workflows. *Remote Sens.* 2018;10(7):1091.
223. Guo Y, Senthilnath J, Wu W, Zhang X, Zeng Z, Huang H. Radiometric calibration for multispectral camera of different imaging conditions mounted on a UAV platform. *Sustainability.* 2019;11(4):978.
224. Kedzierski M, Wierzbicki D, Sekrecka A, Fryskowska A, Walczykowski P, Siewert J. Influence of Lower Atmosphere on the Radiometric Quality of Unmanned Aerial Vehicle Imagery. *Remote Sens.* 2019;11(10):1214. doi:10.3390/rs11101214
225. Burkart A, Cogliati S, Schickling A, Rascher U. A Novel UAV-Based Ultra-Light Weight Spectrometer for Field Spectroscopy. *IEEE Sens J.* 2014;14(1):62-67. doi:10.1109/JSEN.2013.2279720

226. Zarco-Tejada PJ, González-Dugo V, Berni JAJ. Fluorescence, temperature and narrow-band indices acquired from a UAV platform for water stress detection using a micro-hyperspectral imager and a thermal camera. *Remote Sens Environ.* 2012;117:322-337. doi:10.1016/j.rse.2011.10.007
227. Bendig J, Gautam D, Malenovský Z, Lucieer A. Influence of Cosine Corrector and Uas Platform Dynamics on Airborne Spectral Irradiance Measurements. In: *IGARSS 2018 - 2018 IEEE International Geoscience and Remote Sensing Symposium.* ; 2018:8822-8825. doi:10.1109/IGARSS.2018.8518864
228. Suomalainen J, Hakala T, Peltoniemi J, Puttonen E. Polarised Multiangular Reflectance Measurements Using the Finnish Geodetic Institute Field Goniospectrometer. *Sensors.* 2009;9(5):3891-3907. doi:10.3390/s90503891
229. Peterson WA, Dirmhirn I. The Ratio of Diffuse to Direct Solar Irradiance (Perpendicular to the Sun's Rays) with Clear Skies? A Conserved Quantity Throughout the Day. *J Appl Meteorol Climatol.* 1981;20(7):826-828. doi:10.1175/1520-0450(1981)020<0826:TRODTD>2.0.CO;2
230. Royer A, Vincent P, Bonn F. Evaluation and correction of viewing angle effects on satellite measurements of bidirectional reflectance. *Photogramm Eng Remote Sens.* 1985;51(12):1899-1914.
231. Sekrecka A, Wierzbicki D, Kedzierski M. Influence of the Sun Position and Platform Orientation on the Quality of Imagery Obtained from Unmanned Aerial Vehicles. *Remote Sens.* 2020;12(6):1040.
232. Stark B, Zhao T, Chen Y. An analysis of the effect of the bidirectional reflectance distribution function on remote sensing imagery accuracy from small unmanned aircraft systems. In: *2016 International Conference on Unmanned Aircraft Systems (ICUAS).* IEEE; 2016:1342-1350.
233. Li Z, Roy DP, Zhang HK. The incidence and magnitude of the hot-spot bidirectional reflectance distribution function (BRDF) signature in GOES-16 Advanced Baseline Imager (ABI) 10 and 15 minute reflectance over north America. *Remote Sens Environ.* 2021;265:112638. doi:10.1016/j.rse.2021.112638
234. Jacquemoud S, Verhoef W, Baret F, et al. PROSPECT+ SAIL models: A review of use for vegetation characterization. *Remote Sens Environ.* 2009;113:S56-S66.
235. Nicodemus FE, Richmond JC, Hsia JJ, Ginsberg IW, Limperis T. Geometrical considerations and nomenclature for reflectance. *NBS Monogr.* 1992;160:4.
236. Ma X, Huete A, Tran NN, Bi J, Gao S, Zeng Y. Sun-Angle Effects on Remote-Sensing Phenology Observed and Modelled Using Himawari-8. *Remote Sens.* 2020;12(8):1339. doi:10.3390/rs12081339
237. He L, Song X, Feng W, et al. Improved remote sensing of leaf nitrogen concentration in winter wheat using multi-angular hyperspectral data. *Remote Sens Environ.* 2016;174:122-133. doi:10.1016/j.rse.2015.12.007
238. Grenzdörffer GJ, Niemeyer F. UAV based BRDF-measurements of agricultural surfaces with pfiiffikus. *Int Arch Photogramm Remote Sens Spat Inf Sci.* 2011;38:229-234.
239. Honkavaara E, Hakala T, Saari H, Markelin L, Mäkynen J, Rosnell T. A process for radiometric correction of UAV image blocks. *Photogramm Fernerkund Geoinformation.* 2012;(2):115-127.

240. Hasegawa K, Matsuyama H, Tsuzuki H, Sweda T. Improving the estimation of leaf area index by using remotely sensed NDVI with BRDF signatures. *Remote Sens Environ.* 2010;114(3):514-519. doi:10.1016/j.rse.2009.10.005
241. Cerstl SAW, Simmer C. Radiation physics and modelling for off-nadir satellite-sensing of non-Lambertian surfaces. *Remote Sens Environ.* 1986;20(1):1-29. doi:10.1016/0034-4257(86)90011-8
242. He L, Chen JM, Pisek J, Schaaf CB, Strahler AH. Global clumping index map derived from the MODIS BRDF product. *Remote Sens Environ.* 2012;119:118-130. doi:10.1016/j.rse.2011.12.008
243. Lacaze R, Chen JM, Roujean JL, Leblanc SG. Retrieval of vegetation clumping index using hot spot signatures measured by POLDER instrument. *Remote Sens Environ.* 2002;79(1):84-95. doi:10.1016/S0034-4257(01)00241-3
244. Wei S, Fang H. Estimation of canopy clumping index from MISR and MODIS sensors using the normalized difference hotspot and darkspot (NDHD) method: The influence of BRDF models and solar zenith angle. *Remote Sens Environ.* 2016;187:476-491. doi:10.1016/j.rse.2016.10.039
245. Verhoef W. Earth observation modeling based on layer scattering matrices. *Remote Sens Environ.* 1985;17(2):165-178. doi:10.1016/0034-4257(85)90072-0
246. Verhoef W, Jia L, Xiao Q, Su Z. Unified Optical-Thermal Four-Stream Radiative Transfer Theory for Homogeneous Vegetation Canopies. *IEEE Trans Geosci Remote Sens.* 2007;45(6):1808-1822. doi:10.1109/TGRS.2007.895844
247. Standards USNB of, Nicodemus FE. *Geometrical Considerations and Nomenclature for Reflectance*. Vol 160. US Department of Commerce, National Bureau of Standards Washington, DC, USA; 1977.
248. Weiss A, Norman JM. Partitioning solar radiation into direct and diffuse, visible and near-infrared components. *Agric For Meteorol.* 1985;34(2):205-213. doi:10.1016/0168-1923(85)90020-6
249. Doctor KZ, Bachmann CM, Gray DJ, Montes MJ, Fusina RA. Wavelength dependence of the bidirectional reflectance distribution function (BRDF) of beach sands. *Appl Opt.* 2015;54(31):F243-F255. doi:10.1364/AO.54.00F243
250. DJI. P4 Multispectral - Specifications - DJI. DJI Official. Published 2022. Accessed August 5, 2022. <https://www.dji.com/p4-multispectral/specs>
251. Micasense. What is the center wavelength and bandwidth of each filter for MicaSense sensors? MicaSense Knowledge Base. Published 2022. Accessed August 5, 2022. <https://support.micasense.com/hc/en-us/articles/214878778-What-is-the-center-wavelength-and-bandwidth-of-each-filter-for-MicaSense-sensors->
252. MicaSense. RedEdge Camera Radiometric Calibration Model. MicaSense Knowledge Base. Published 2020. Accessed December 1, 2020. <https://support.micasense.com/hc/en-us/articles/115000351194-RedEdge-Camera-Radiometric-Calibration-Model>
253. DJI Co. P4 Multispectral - Downloads - DJI. DJI Official. Published 2020. Accessed November 19, 2021. [https://dl.djicdn.com/downloads/p4-multispectral/20200717/P4\\_Multispectral\\_Image\\_Processing\\_Guide\\_EN.pdf](https://dl.djicdn.com/downloads/p4-multispectral/20200717/P4_Multispectral_Image_Processing_Guide_EN.pdf)

254. Moghimi A, Yang C, Miller ME, Kianian SF, Marchetto PM. A Novel Approach to Assess Salt Stress Tolerance in Wheat Using Hyperspectral Imaging. *Front Plant Sci.* 2018;9:1182. doi:10.3389/fpls.2018.01182
255. Otsu N. A threshold selection method from gray-level histograms. *IEEE Trans Syst Man Cybern.* 1979;9(1):62-66.
256. Kuusk A. The Hot Spot Effect in Plant Canopy Reflectance. In: Myneni RB, Ross J, eds. *Photon-Vegetation Interactions: Applications in Optical Remote Sensing and Plant Ecology*. Springer Berlin Heidelberg; 1991:139-159. doi:10.1007/978-3-642-75389-3\_5
257. Ranson KJ, Daughtry CST, Biehl LL, Bauer ME. Sun-view angle effects on reflectance factors of corn canopies. *Remote Sens Environ.* 1985;18(2):147-161. doi:10.1016/0034-4257(85)90045-8
258. Verhoef W, Jia L, Su Z. Optical-thermal canopy radiance directionality modelling by unified 4SAIL model. Published online 2007.
259. Zhu G, Ju W, Chen JM, Gong P, Xing B, Zhu J. Foliage Clumping Index Over China's Landmass Retrieved From the MODIS BRDF Parameters Product. *IEEE Trans Geosci Remote Sens.* 2012;50(6):2122-2137. doi:10.1109/TGRS.2011.2172213
260. Weiss M, Jacob F, Duveiller G. Remote sensing for agricultural applications: A meta-review. *Remote Sens Environ.* 2020;236:111402. doi:10.1016/j.rse.2019.111402
261. Brook A, Polinova M, Ben-Dor E. Fine tuning of the SVC method for airborne hyperspectral sensors: the BRDF correction of the calibration nets targets. *Remote Sens Environ.* 2018;204:861-871. doi:10.1016/j.rse.2017.09.014
262. Moghimi A, Pourreza A, Zuniga-Ramirez G, Williams LE, Fidelibus MW. A Novel Machine Learning Approach to Estimate Grapevine Leaf Nitrogen Concentration Using Aerial Multispectral Imagery. *Remote Sens.* 2020;12(21):3515.
263. Arroyo-Mora JP, Kalacska M, Løke T, et al. Assessing the impact of illumination on UAV pushbroom hyperspectral imagery collected under various cloud cover conditions. *Remote Sens Environ.* 2021;258:112396. doi:10.1016/j.rse.2021.112396

## 5 Appendix

*Table A. 1- The full results of the experiments outlined in this study. Calculation methods and equations are presented below the table.*

	Band	Prime s' mean	Primes' STD	Mean of min views	Mean of max views	Percent of change % (total)	Average RMSD	Model coefficients [a1, a2, $\sigma_y$ , $\sigma_x$ ]	RMS of prime errors	Average fit r <sup>2</sup>
19/03/18	B	2.6	0.22	2.0	3.3	-21 to 30 (51)	0.35	[1.32e-2, -5.77e-10, -3.37e6, 54.0]	0.1	0.78
	G	8.6	0.8	6.2	11.6	-28 to 33 (62)	1.48	[1.47e-2, -1.55e-09, -4.32e6, 73.9]	0.41	0.78
	R	3.9	0.55	2.9	5.6	-27 to 42 (69)	0.77	[1.67 e-2, -3.1e-09, -1.46 e6, 47.5]	0.2	0.63
	RE	26.4	1.95	20.5	34.5	-22 to 30 (53)	3.76	[11.4 e-2, -3.56e-09, -5.92e6, 57.0]	1.08	0.85
	NIR	45.0	2.79	39.4	55.5	-12 to 23 (35)	4.43	[31.6 e-2, -7.65e-09, -3.45e6, 48.4]	1.2	0.82
19/06/12	B	2.9	0.24	2.17	3.92	-24 to 37 (61)	0.53	[0.0151, 0.646e-6, 59.2, 29.2]	0.16	0.83
	G	11.4	0.93	8.97	15.31	-22 to 33 (55)	1.93	[0.052, 1.46e-6, 80.2, 38.4]	0.57	0.84
	R	3.9	0.34	3.1	5.5	-22 to 39 (61)	0.72	[0.0263, 1.36e-6, 45.9, 22.3]	0.2	0.82
	RE	25	1.48	20.1	32.5	-20 to 29 (49)	3.71	[0.115, 2.23e-6, 97.2, 42.3]	1.09	0.87
	NIR	46.8	2.6	40.8	56.4	-12 to 21 (33)	4.58	[0.36, 4.29e-6, 79.5, 27.8]	1.27	0.85
19/09/05	B	3.7	0.23	3.0	4.4	-18 to 21 (39)	0.45	[0.0162, 1.35e-05, 199.0, 57.4]	0.16	0.88
sunny	G	8.1	0.55	6.6	10.0	-18 to 23 (42)	1.06	[0.0499, 4.01e-05, 211.0, 37.3]	0.36	0.85
	R	4.6	0.32	3.7	5.9	-19 to 26 (46)	0.64	[0.0323, 4.97e-05, 144.0, 27.7]	0.22	0.78
	RE	17.8	1.03	14.8	22	-16 to 23 (40)	2.19	[0.104, 6.48e-05, 221.0, 45.2]	0.72	0.86
	NIR	35.4	1.83	31.6	41.2	-10 to 16 (26)	2.89	[0.291, 0.000115, 263.0, 28.8]	0.98	0.77
19/09/05	B	3.8	0.27	3.4	4.0	-10 to 6 (17)	0.27	[-0.532, 1.07e-11, 1.42e7, 15100]		0.04
cloudy	G	8.2	0.57	7.3	9.1	-10 to 10 (20)	0.55	[-3.27, 1.76e-11, 4.14 e7, 18500]		0.14
	R	4.4	0.41	3.9	5.0	-11 to 12 (23)	0.33	[-3.14, 1.29e-11, 4.29 e7, 23000]		0.23
	RE	17.9	1.0	16.1	19.8	-9 to 10 (20)	1.18	[-4.82, 4.1e-11, 4.42 e7, 11100]		0.21
	NIR	46.9	2.73	43.5	51.1	-10 to 6 (16)	2.93	[-3.01, 1.16e-10, 1.76 e7, 6890]		0.04
19/12/03	B	2.3	0.24	2.1	2.6	-7 to 9 (23)	0.3	[-0.0372, 9.87e-11, 410000, 6130]	-	0.00
	G	5.9	0.61	5.3	6.7	-9 to 14 (23)	0.68	[0.0582, 2.77e-08, 112000000, 14.5]	-	0.03
	R	3	0.35	2.7	3.5	-10 to 16 (26)	0.40	[0.0304, 4.15e-07, 167000000, 8.3]	-	0.02
	RE	16.6	1.65	15	18.8	-10 to 13 (23)	2	[0.161, 1.7e-08, 59800000, 19.5]	-	0.04
	NIR	38.4	3.56	35.2	44.2	-8 to 15 (23)	5	[0.393, 6.67e-06, 3.32e10, 6.62]	-	0.01
19/12/17	B	2.4	0.18	2.2	2.7	-8 to 14 (22)	0.21	[0.0214, 1.37e-09, 7200000.0, 32.0]	-	0.20
	G	6.5	0.55	5.8	7.5	-10 to 16 (26)	0.62	[0.0522, 2.61e-09, 11400000.0, 35.5]	-	0.36
	R	3.1	0.34	2.7	3.8	-10 to 22 (33)	0.42	[0.0273, 3.85e-09, 17500000.0, 23.5]	-	0.26
	RE	18.6	1.49	16.7	21.6	-10 to 16 (26)	1.99	[0.16, 6.31e-09, 29900000.0, 27.8]	-	0.37
	NIR	43.3	3.21	39.8	50.9	-7 to 17 (25)	5.48	[0.438, 1.3e-07, 738000000.0, 10.4]	-	0.14
20/06/17 P4M	B	1.6	0.27	1.05	2.23	-33 to 43 (76)	0.31	[0.00873, 5.95e-05, 37.6, 25.9]	0.09	0.82
	G	4.1	0.82	2.78	5.76	-32 to 40 (72)	0.81	[0.0217, 0.000106, 50.7, 27.6]	0.21	0.85
	R	2.2	0.44	1.33	3.27	-38 to 51 (89)	0.50	[0.0109, 9.36e-05, 40.5, 24.9]	0.14	0.80
	RE	16.4	3	9.93	20.8	-39 to 27 (66)	3.13	[-0.136, 5.65e-05, 190.0, 129.0]	0.72	0.82
	NIR	26.5	4.2	18.26	32.15	-31 to 21 (52)	4.1	[-0.0191, 0.00011, 136.0, 92.6]	0.95	0.82
20_9_29 P4M	B	3.0	0.26	2.3	3.3	-22 to 10 (32)	0.31	[-13.4, 5.21e-09, 164000, 62700.0]	0.07	0.64
	G	5.4	0.52	4.2	6.1	-21 to 13 (35)	0.62	[-23.6, 8.35e-09, 230000, 49100.0]	0.16	0.69
	R	4.0	0.43	2.7	4.6	-31 to 15 (47)	0.59	[-31.4, 9.99e-09, 163000, 77300.0]	0.14	0.62
	RE	17.7	1.78	11.2	19.8	-36 to 11 (48)	2.82	[-240.0, 4.09e-08, 174000, 136000]	0.63	0.72
	NIR	30.6	3.52	22.0	33.8	-28 to 10 (38)	3.97	[-375.0, 3.5e-08, 311000, 138000]	0.91	0.64
20/11/20 P4M	B	1.9	0.86	1.3	2.6	-33 to 37 (70)	0.48			
	G	3.5	1.71	2.4	5.5	-33 to 54 (87)	1.07			
Part cloudy	R	2.2	1.13	1.2	3.1	-42 to 45 (88)	0.66			
	RE	13.6	7.12	7.5	19.3	-44 to 42 (86)	4.19			
	NIR	23.4	12.82	13.6	33.2	-41 to 42 (84)	7.2			
20/12/16 P4M	B	2.6	0.3	1.9	3.1	-24 to 20 (44)	0.32	[-8.36, 1.34e-09, 534000, 46900]	0.07	0.57
	G	5.8	0.76	4.5	7.7	-23 to 32 (55)	0.94	[0.0312, 1.94e-09, 9260000, 50.7]	0.21	0.76
	R	3.7	0.57	2.3	4.7	-38 to 25 (64)	0.69	[-23.6, 6.64e-09, 222000, 64200]	0.15	0.53
	RE	28.7	2.84	17.4	31.5	-39 to 9 (49)	4.69	[-344.0, 4.04e-08, 191000, 179000]	0.89	0.56
	NIR	47.4	4.52	32.1	51.2	-32 to 7 (40)	6.03	[-530.0, 3.67e-08, 309000, 187000]	1.21	0.42
19/5/29 MRE	B	3.2	0.37	2.7	3.7	-15 to 15 (30)	0.28	[-1.1, -3.31e-12, -3.52e8, 3940]	0.04	0.57
Almond	G	8.2	0.79	6.9	9.6	-16 to 16 (33)	0.78	[-8.23, -1.51e-11, -2.3e8, 9650.0]	0.13	0.65
	R	4.0	0.53	3.4	5.0	-15 to 23 (39)	0.47	[0.0322, -1.53e-09, -8.16 e6, 22.0]	0.05	0.37
	RE	21.9	1.54	18.4	25.2	-16 to 14 (30)	1.95	[-33.9, -6.65e-11, -1.26 e8, 16400]	0.32	0.63

	NIR	42.1	3.04	36.7	48.2	-13 to 14 (27)	3.64	[-16.1, -2.31e-10, -4.84 e7, 5970.0]	0.43	0.13
19_7_26 MRE	B	4.5	0.46	3.5	6.0	-22 to 34 (56)	0.64	[0.0323, -3.83e-10, -8.46 e6, 28.7]	0.11	0.54
	G	11.9	0.98	9.3	15.6	-21 to 31 (53)	1.61	[0.072, -9.26e-10, -7.34 e6, 43.5]	0.29	0.63
	R	6.0	0.82	4.8	8.4	-20 to 39 (60)	0.93	[0.0466, -5.44e-10, -1.06 e7, 21.3]	0.15	0.51
	RE	21.5	1.32	17.0	27.6	-20 to 28 (49)	2.66	[0.115, -1.16e-09, -9.01 e6, 55.1]	0.5	0.68
	NIR	39.4	1.86	33.6	49.0	-14 to 24 (39)	3.88	[0.307, 1.03e-09, 1.57 e7, 39.2]	0.66	0.64
20_6_2 P4M	B	3.9	0.26	3.0	4.5	-22 to 15 (38)	0.44	[-8.35, 5.68e-08, 24700.0, 23900.0]	0.08	0.44
Almond	G	8.2	0.5	6.7	9.6	-17 to 16 (34)	0.82	[-1.63, 9.44e-07, 3090.0, 2360.0]	0.16	0.42
Without DLS	R	5.0	0.42	3.7	6.0	-25 to 19 (45)	0.66	[-5.65, 1.93e-07, 9650.0, 12200.0]	0.12	0.45
	RE	27.3	1.64	19.4	28.7	-29 to 5 (34)	3.77	[-67.0, 2.91e-07, 21500.0, 43000.0]	0.21	0.46
	NIR	46.6	3.23	36.3	49.3	-22 to 5 (27)	4.86	[-62.2, 4.46e-07, 18800.0, 30000.0]	0.00	0.56
	B	4.0	0.3	3.1	4.7	-21 to 16 (38)	0.43	[-6.01, 9.29e-08, 15800.0, 16500.0]	0.09	0.68
With DLS	G	8.5	0.57	7.0	10.0	-17 to 17 (35)	0.84	[0.0474, 7.9e-05, 58.3, 46.2]	0.18	0.77
	R	5.2	0.5	2.9	6.2	-24 to 21 (46)	0.66	[0.0169, 5.58e-05, 53.5, 62.0]	0.14	0.68
	RE	28.0	1.3	19.8	29.2	-29 to 4 (33)	3.86	[-66.2, 4.16e-07, 18300.0, 35000.0]	0.56	0.47
	NIR	47.6	2.61	36.9	49.6	-22 to 4 (26)	4.85	[-105.0, 4.05e-07, 27500.0, 37800]	0.71	0.54
20/07/08 P4M	B	10.4	0.8	7.2	12.9	-30 to 24 (55)	1.7	[-39.5, 2.71e-07, 24000.0, 24300.0]	0.35	0.76
With dls	G	22.6	1.58	17.2	27.7	-23 to 22 (46)	3.09	[0.102, 0.000409, 47.8, 37.2]	0.68	0.77
	R	14.8	1.54	9.4	18.6	-36 to 25 (62)	2.91	[-49.2, 6.25e-07, 16500.0, 19200.0]	0.58	0.68
	RE	65.8	3.18	42.6	71.7	-35 to 9 (44)	11.71	[-257.0, 1.46e-06, 19600, 36000]	1.98	0.62
	NIR	105	5.56	76.9	114.9	-27 to 8 (35)	14.42	[-259.0, 2.2e-06, 19100.0, 24800.0]	2.44	0.48
20/07/08 P4M	B	4.0	0.28	2.8	5.1	-30 to 27 (57)	0.63	[-1.19, 9.49e-07, 1980.0, 2650.0]	0.11	0.77
	G	8.3	0.5	6.4	10.4	-22 to 25 (48)	1.09	[-0.0287, 3.62e-05, 133.0, 113.0]	0.21	0.82
No dls	R	5.6	0.56	3.6	7.2	-36 to 29 (65)	1.05	[-9.72, 3.19e-07, 9990.0, 12300.0]	0.19	0.71
	RE	26.1	1.05	16.5	28.8	-36 to 10 (47)	4.66	[-83.1, 5.2e-07, 18000.0, 35600.0]	0.7	0.66
	NIR	39.2	1.98	27.7	43.0	-29 to 9 (39)	5.32	[-125.0, 4.21e-07, 29500, 40600]	0.77	0.52
21/06/23	B	3.9	0.25	2.4	4.6	-38 to 16 (55)	0.73	[-16.3, 2.88e-07, 15000.0, 15200.0]	0.19	0.62
Grape	G	10	0.73	7.6	11.2	-24 to 12 (36)	1.26	[-15.9, 1.02e-06, 7950.0, 7950.0]	0.36	0.66
	R	5.1	0.35	2.4	6.1	-52 to 19 (72)	1.22	[-26.2, 5.19e-07, 13200.0, 15300.0]	0.3	0.57
	RE	34.3	2.02	20.5	36.2	-40 to 5 (45)	5.51	[-134.0, 1.94e-06, 11700.0, 23600]	0.99	0.40
	NIR	57.3	2.54	41.6	59.4	-27 to 3 (30)	6.54	[-174.0, 1.91e-06, 18800.0, 19600]	1.58	0.17
21/08/17	B	3.9	0.35	2.4	5.3	-38 to 33 (71)	0.83	[-17.7, 3.69e-07, 17700.0, 10800.0]	0.29	0.82
	G	8.8	0.69	6.7	11.3	-23 to 28 (51)	1.41	[-9.43, 8.68e-07, 13000.0, 3380.0]	0.44	0.84
	R	5.1	0.71	2.6	7.2	-48 to 40 (89)	1.39	[-16.8, 1.02e-06, 10400.0, 6360.0]	0.46	0.82
	RE	28.3	2.44	17.7	31.8	-37 to 12 (49)	4.81	[-122.0, 1.63e-06, 18000, 16700.0]	1.43	0.60
	NIR	46.5	3.82	33.1	50.2	-28 to 8 (36)	6.08	[-148.0, 1.71e-06, 21900, 15900]	1.7	0.49

$$A\text{-RMSD} = \frac{\sum_{i=1}^{tn} \sqrt{\frac{\sum_{\theta_r=-60}^{+60} \sum_{\phi_r=-60}^{+60} (R_{(\theta_r, \phi_r)} - R_{Prime})^2}{\text{Number of views of tree}(i)}}}{tn} \quad \text{Eq.A.1}$$

(Average RMSD of all views of all trees)

tn=total number of trees

$\hat{R}$  =predicted reflectance

$\bar{R}$  = Average reflectance of all view angles of one tree

$$\text{RMS of prime errors} = \sqrt{\frac{\sum_{i=1}^{tn} (\hat{R}_{(\theta_r=0)} - R_{Prime})^2}{tn}} \quad \text{Eq. A.2}$$

$$\text{Residual sum of squares (SSR)} = \sum_{\theta_r=-60}^{+60} \sum_{\phi_r=-60}^{+60} (R_{(\theta_r, \phi_r)} - \hat{R}_{(\theta_r, \phi_r)})^2 \quad \text{Eq. A.3}$$

$$\text{Total sum of squares (SST)} = \sum_{\theta_r=-60}^{+60} \sum_{\phi_r=-60}^{+60} (R_{(\theta_r, \phi_r)} - \bar{R})^2 \quad \text{Eq. A.4}$$

$$r^2 = 1 - \frac{SSR}{SST} \quad \text{Eq. A.5}$$

$$\text{Average } r^2 = \frac{\sum_{i=1}^{tn} r_i^2}{tn} \quad \text{Eq. A.6}$$

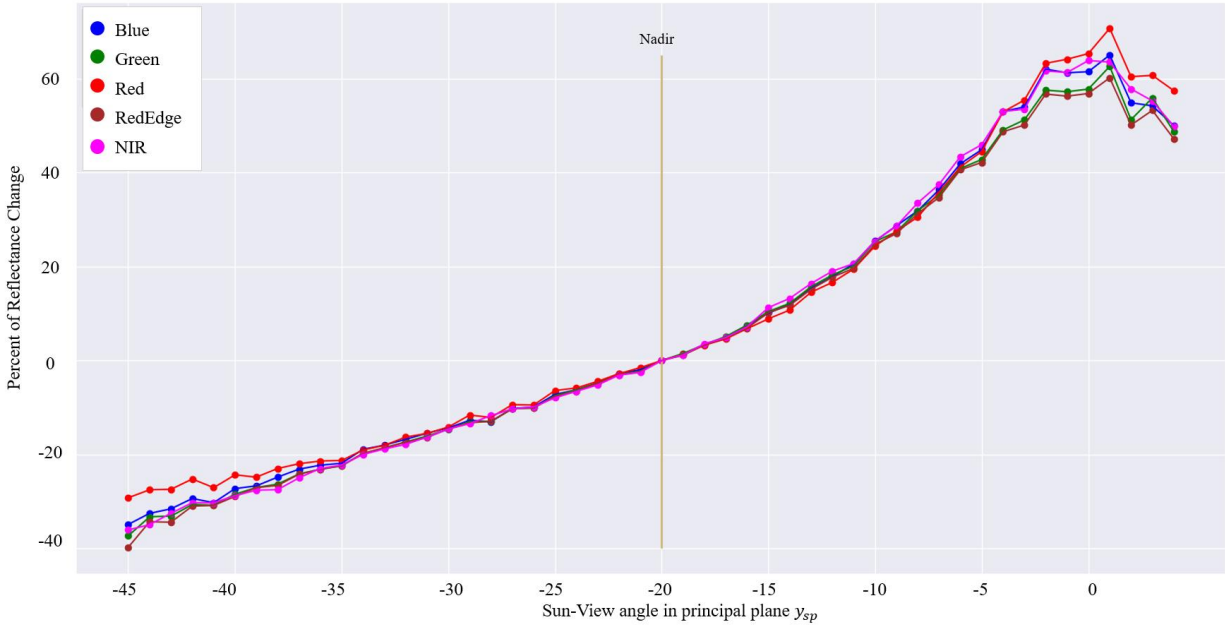


Figure A. 1- Percentage of reflectance variation from the Nadir view at each band in the 19/06/12 citrus dataset.

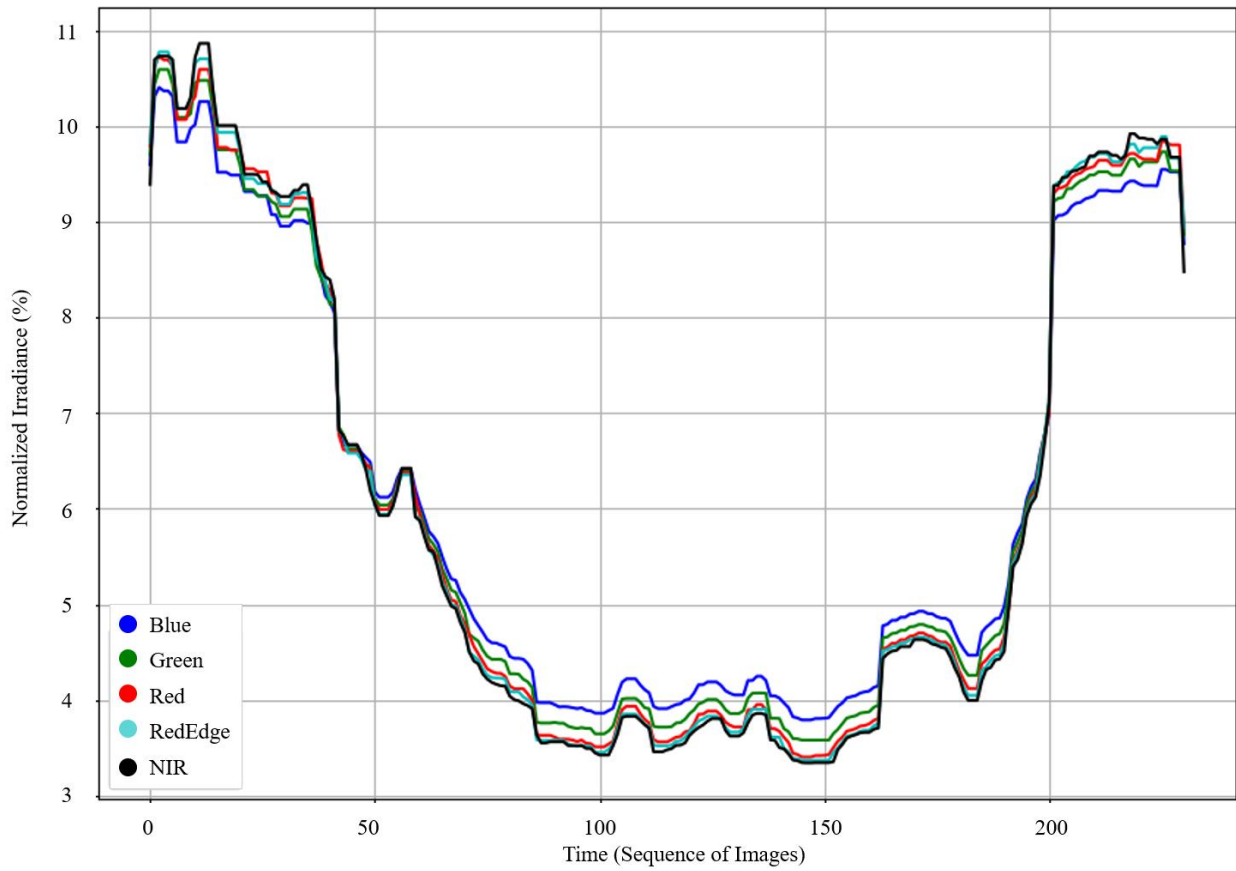


Figure A. 2- An example of the DLS sensor reading on a partly cloudy day (Normalized irradiance recording of 20/11/20 citrus dataset). The flight paths are perpendicular to the solar plane, reducing the effect of the UAS's fluctuations on the DLS readings. With this setting, variations in the DLS readings are mainly based on actual irradiance variations, e.g., clouds.

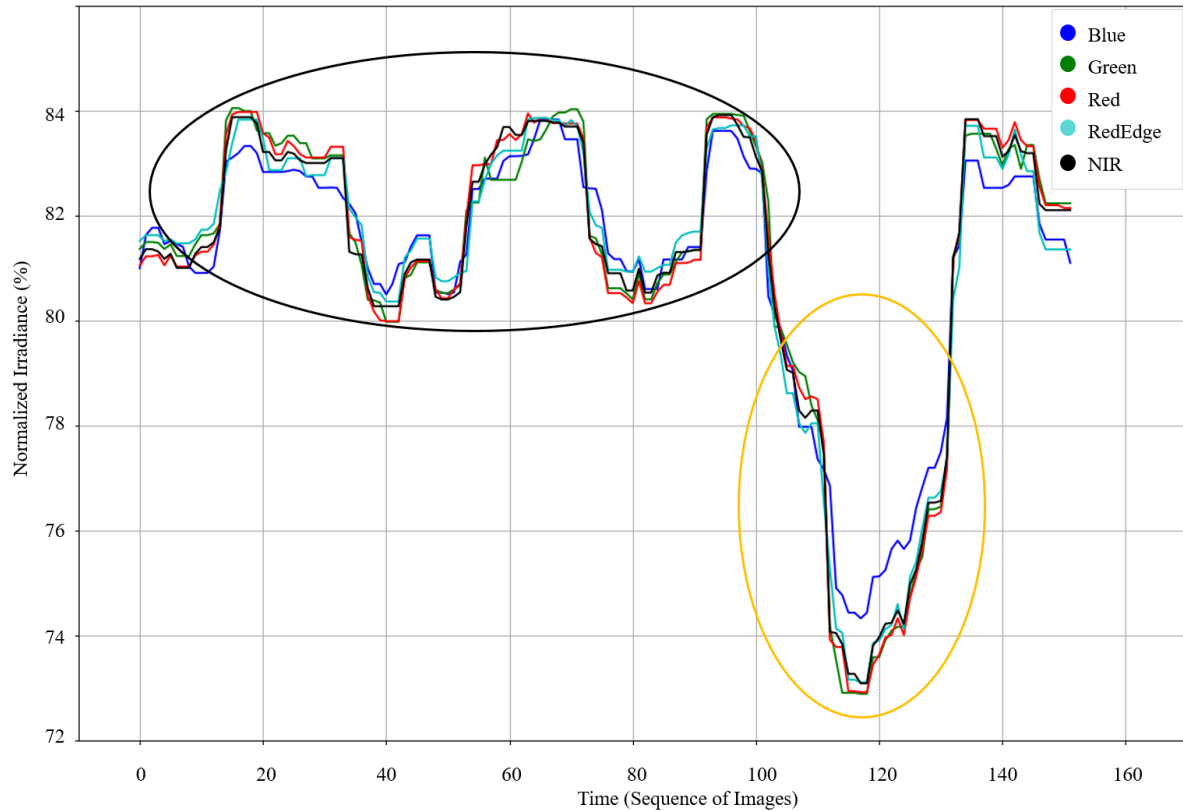


Figure A. 3- DLS readings of the MRE when the flight mission is parallel to the solar plane. Pitch fluctuations affect the DLS readings that are shown with the black oval. In this setting, determining actual irradiance changes would be challenging. An actual extreme irradiance drop due to cloud movements is marked with the yellow oval.

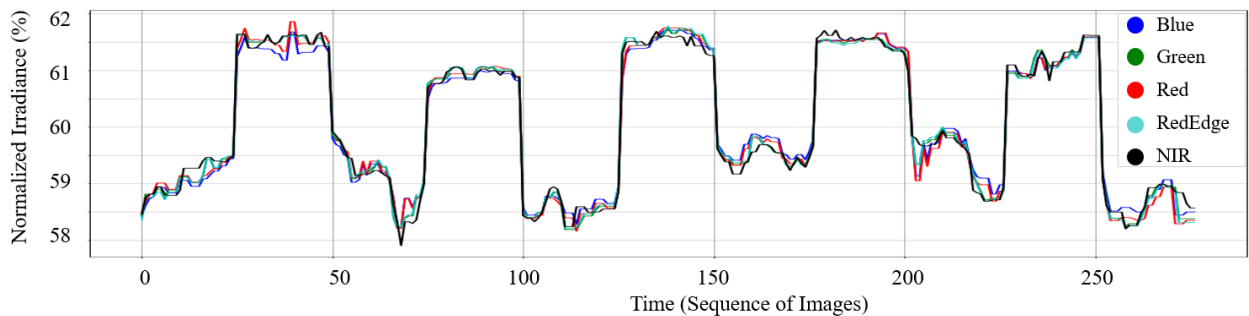


Figure A. 4- DLS readings of a P4M flight mission whose paths are parallel to the solar plane. Even though irradiance varies steadily, due to the ineffective cosine corrector of the P4M DLS, roll and pitch fluctuations of the UAS drastically affect the DLS readings.

Note that Figures Fig. A.3, Fig. A.4 both show flight missions (One for P4M and one for MRE) that are parallel to the solar plane. Thus, DLS readings are affected by pitch angles. This confirms that DLS sensors on both P4M and MRE lack a reliable cosine corrector.